UNIVERSITÀ
DEGLI STUDI
DI TRIESTE

UNIVERSITÀ DEGLI STUDI DI TRIESTE

XXXIV CICLO DEL DOTTORATO DI RICERCA IN NANOTECNOLOGIE

SMART NANOSTRUCTURED ELECTROCATALYSTS FOR SMALL MOLECULES ACTIVATION

DOTTORANDO
Marcello Ferrara
Marcello Ferrara

COORDINATORE
Chiar.mo PROF. Morgante Alberto

SUPERVISORE DI TESI
Chiar.mo PROF. Paolo Fornasiero
Paolo Fornasiero

ANNO ACCADEMICO 2020/2021

[..]

Abstract

In the modern age, electricity has risen in demand as slowly but steadily electric power becomes the most used form of energy to power our technological progress. Energy conversion and storage, in particular, is a field that has gained momentum since it became apparent that fossil fuel dependence would not be sustainable in the long term. After The United Nations Framework Convention on Climate Change (UNFCCC) and the third Conference of Parties (COP-3, culminating in the Kyoto Protocol) research on better materials to be employed in electrocatalysis has exploded, fuelled by environmental concerns. However, even if electrochemical devices, such as electrolyzers and fuel cells, offer better performances than current solutions (i.e. internal combustion engines), the need for expensive catalysts still hampers widespread adoption. In order to lessen the burden on current precious metals demand, research is focusing on carbon-based materials, non-noble metals and their composites. Moreover, nanotechnology represents a set of tools to boost (and finetune) materials' properties for electrocatalytic applications, leading to a general reduction in weight and price of commercial catalysts. In this thesis, the use of advanced synthetic techniques as well as morphological, textural and (electro)chemical characterizations (e.g. TEM, XRD, XPS, EIS, GC) allowed to optimize various electrocatalysts for different applications at the forefront of electrocatalysis research. The dissertation focuses on the reduction of small molecules that can be found in the atmosphere (O_2, N_2 and CO_2) to produce valuable chemicals (H_2O_2, NH_3, hydrocarbons) or energy. Being able to fix these elements at room temperature and pressures (unlike current methods such as the Haber-Bosh process) from the gas phase could be instrumental to the implementation of a circular economy based on them. Finally, a particular focus of this thesis is the development of methods to streamline future catalytic tests and their application in electrolyzer setups resembling industrial conditions to have a more realistic image of their efficiencies in a "real case scenario" (i.e. presence of impurities, high currents, longer working times).

Riassunto

Nell'era moderna la richiesta di elettricità è cresciuta lentamente ma inesorabilmente, mentre è divenuta la forma di energia più importante per il progresso scientifico. I sistemi di accumulo e conversione sono in particolare oggetto di molti studi, sin dalle prime ratifiche di accordi internazionali sulla crisi climatica (per primi i protocolli di Kyoto). Data la natura limitata e "sporca" dei combustibili fossili (la loro combustione non solo libera CO_2, ma anche polveri sottili e gas acidi come ossidi di zolfo e azoto), la ricerca si sta concentrando in altre tecnologie, come ad esempio le celle a combustibile e gli elettrolizzatori. Tuttavia, l'adozione di questi device elettrochimici è rallentata dal loro attuale alto costo, principalmente a causa dei catalizzatori. In particolare, le soluzioni commerciali attuali sfruttano principalmente metalli preziosi (come il platino). Il bisogno di catalizzatori più economici ha incentivato lo sviluppo di materiali a base di carbonio e metalli non preziosi. Le nanotecnologie hanno poi permesso lo sviluppo di metodologie e strumenti che permettono la sintesi di materiali nanostrutturati che presentano proprietà potenziate in elettrocatalisi. In questa tesi, l'uso di tecniche di sintesi avanzate, insieme alla caratterizzazione strutturale, superficiale, morfologica e (elettro)chimica ha permesso di ottimizzare degli elettrocatalizzatori per applicazioni all'avanguardia. In particolare, questi catalizzatori possono attivare la riduzione di piccole molecole presenti nell'atmosfera (O_2, N_2 e CO_2) al fine di produrre composti con alto valore commerciale (H_2O_2, NH_3 e idrocarburi) o energia. L'abilità di fissare tali elementi dall'atmosfera senza il bisogno di alte pressioni e temperature (come ad esempio richiede attualmente il processo Haber-Bosh) potrebbe risultare indispensabile per un futuro basato sull'economia circolare. Infine, un particolare obiettivo di questa dissertazione è stata la creazione di metodi per velocizzare la verifica di nuovi catalizzatori e la loro applicazione in elettrolizzatori/celle a combustibile in condizioni più realistiche e vicine all'applicazione industriale (presenza di inquinanti, alte correnti e lunghi tempi di utilizzo).

Index

Preface

The global energy challenge for electricity

The rise of electricity has been the defining characteristic of the modern age. The electrification process gave way to an uninterrupted era of advancement and today allows us to take many commodities for granted. Still, electricity is only a part of our global energy consumption: if we consider heating and transportation, in 2019 electricity covered 82 EJ (10^{18} Joule) out of more than 400 EJ total, or roughly 20%.[1] These numbers have many implications. First, even if our world is slowly moving toward electricity, the pace of this conversion is allowing us to invest also in better infrastructure, such as power lines and energy accumulators (i.e. batteries, molten salt heat storage, pumped hydro, etc.). Second, further research is needed to make electricity more compelling than fossil fuels in many applications that are now dominated by the latter, like heating and transportation. It could be argued that how we generate this electricity is also an important point. Using the latest IEA figures for 2019 (Fig. 0.1), in Europe “clean” sources (tidal, wind, photovoltaics, geothermal, hydro, nuclear, waste and biomass energy conversion) have seen an increase in share, overcoming the 60% figure in 2019 against more traditional fossil fuels. This trend has been slower in other parts of the world (both India and China derive electricity mainly from coal, >60%) but still, it is visible in government policies and industrial investments.[2] Moreover, only the maturity of the electricity sector can convince big industries and the population to embrace new technologies, such as electric vehicles and heat pumps, so research in this field is an imperative.

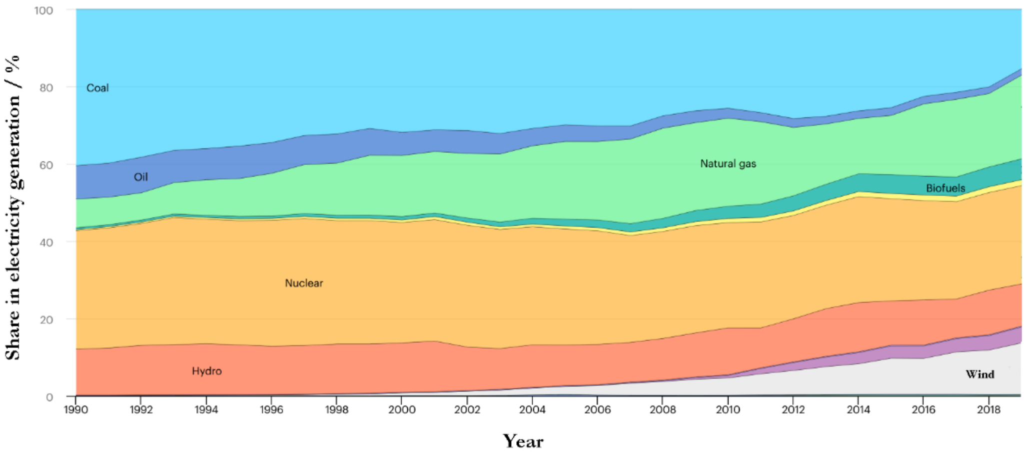

Figure 0.1 European electricity generation by source from 1990 to 2019 from IEA data.[1]

The urge for cleaner and renewable sources is not only dictated by the need to lower our carbon footprint, but also from global political instabilities that prompt our countries in achieving real alternatives to fossil fuels and the problematic ties they entail. Every energy source, of course, has pros and cons. For example, gas and oil can be easily stored and transported wherever they are needed, being energy dense, but they pollute. Many renewable sources are present all around the world, yet in intermittent and diluted form: wind, light and water are somewhat available worldwide and just need the right devices to be taken advantage of properly. Their energy can be stored both chemically (i.e. in batteries or in hydrogen, methanol and many other energy dense molecules) and physically (i.e. in water reservoirs and supercapacitors) to even out their intermittent nature. Otherwise, electricity can be used directly by transporting it through the grid to cities or factories. Herein we refer to the grid as the interconnected network for electricity delivery from producers to consumers, comprising power transmission and distribution nodes.

In general, the two problems of electricity production and its storage and use are not strictly dependent and can be decoupled and addressed separately. Thus, we can conceptually put on hold the generation problem, and focus on the latter point. This thesis explores the recent history of heterogeneous electrochemistry and my research has focused on the development of cathodic catalysts for different applications in the realm of fuel cells and electrolyzers. Both types of devices can use many different materials as catalyst to: i) favor the generation of one specific product over others (in the case of electrolyzers), ii) to minimize -or maximize- power consumption –or production (in the case of fuel cells). Therefore, this research is central to the scientific and technological progress of such devices. The limitations of fossil fuels and the ever-increasing complication in raw materials production led us to prioritize reducing, reusing, and recycling. These concepts are backed in the idea of circular economy, where everything must be done to minimize input from outside the “circle”. Electrochemistry is one of the tools at our disposal for the energy transition process. Other fields of chemistry, such as photochemistry or green organic chemistry, will be instrumental in reshaping the pillars of catalysis: processes like Haber-Bosh and Fisher-Tropsch now produce the majority of some of the most fundamental building blocks in chemistry (NH_3 and hydrocarbons) and will need to be modernized to limit their impact on the environment. Their electrochemical or photochemical related processes not only can work in aqueous systems, but can be fed with CO_2 and N_2, two molecules that are a byproduct of many reactions, and, most importantly, that can be separated from the air. To put within a context the current situation, we can take into consideration the electrolytic production of metallic aluminum. This electrochemical process (i.e. the Hall–Héroult process), with all its drawbacks (high electric consumption and CO_2 production at the anode)[3] revolutionized the aluminum industry and transformed one of the costliest metals in XIX century to a cheap commodity.

1. Introduction

1.1 Electrochemical devices

The Electrolysis Cell (EC or electrolyzer) invention can be traced back to paper by Paets van Troostwijk in 1790[4,5] where he observed that electric discharges from a generator could produce gasses on gold wires in water, concluding that they were oxygen and hydrogen. Today, electrolysis occupies an important role in many industrial processes (first and foremost, electrometallurgic reactions) and many electrocatalytic reactions are in the research stage and could one day revolutionize the energy sector. Just as important to this energy revolution, the Fuel Cell (FC) was first discovered by William Robert Grove in 1839, when he noticed that platinum plates in contact with oxygen and hydrogen generated a current detectable by a galvanometer.[6] In many ways, FCs and ECs can be thought as the same device working with inversed polarization: while one can use electric power to form high energy chemical bonds (electrolyzer, Fig. 1.1a), the other can channel the potential energy of a molecule in a direct electrical current (fuel cell, Fig. 1.1b). Whatever the chemistry behind ECs and FCs, they can be divided in the same basic components: two electrodes (in grey, Fig. 1.1), an electrolyte (in blue, Fig. 1.1) and a separator (or membrane, in pale blue in Fig. 1.1). The two electrodes are connected to a load in a fuel cell or to a source of electrical power in an electrolyzer and the electrolyte-separator maintain the chemical equilibrium and the circuit closed.

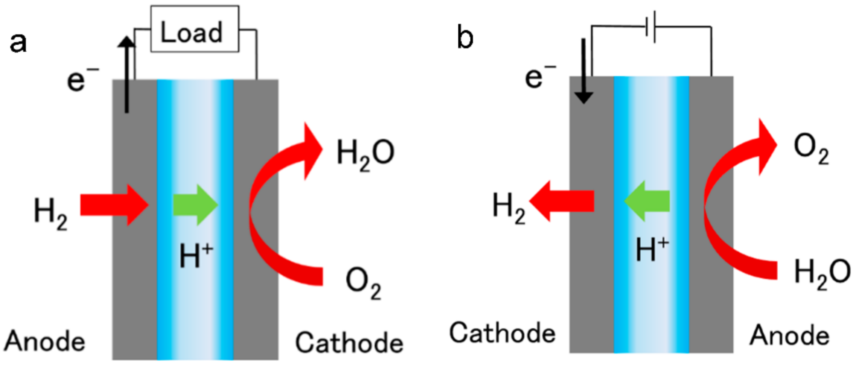

Figure 1.1 Schematic of (a) a water electrolyzer; and (b) a fuel cell (examples of a polymer electrolyte water electrolyzer and a polymer electrolyte fuel cell, respectively). Reprinted with permission from ref. [7]. Copyright © 2018 by the authors.

To this day, many technologies exist for FCs (and ECs), able to function with different components and in different pressure and temperature ranges. Proton Exchange Membrane Fuel Cells (PEMFCs) use polymer membranes that can shuttle protons from one side to the other to keep the reactions going. Anion Exchange Membrane Fuel Cell (AEMFC) use membranes that are able to transfer hydroxide ions and are thus more suitable for alkaline electrolytes. Both PEM and AEM FCs use aqueous electrolytes and behave best between 25 and 100 °C. On the other side, Solid Oxide Fuel Cells (SOFCs) are solid-state devices that can function only at high temperatures (between 450 and 1000 °C), where their solid electrolyte becomes conductive enough to sustain the device operation. Of course, each technology has its own pros and cons, both regarding the possible *fuels* (e.g. SOFCs are much more durable to chemical poisoning), the costs of the device and its operation and finally the target for energy production/consumption (i.e. small and portable or big and fixed). Many different reactions can be exploited both at the anode and the cathode in FCs and ECs: the Hydrogen Evolution Reaction (HER), Oxygen Reduction Reaction (ORR), the Nitrogen Reduction Reaction (NRR), the CO_2 Reduction Reaction (CO_2RR) are all possible reaction at the cathode side, while Oxygen Evolution Reaction (OER) and the Methanol Oxidation Reaction (MOR) are two of the most researched reactions for the anode. Once the design of the device and a pair of half reactions are chosen, the three main components (i.e. electrodes, electrolyte and membrane) can be optimized. As an example, if the reactant has low solubility in the electrolyte one possibility is the creation of an interface where the solid electrode is in contact with both a gas-phase reactant and the liquid electrolyte (Fig. 1.2, third iteration). This Triple Phase Boundary (TPB) is possible through the Gas Diffusion Electrode (GDE), composed of a conductive hydrophilic surface on one side, and a hydrophobic texture for the gas interface on the other. The GDE not only allows for more contact between the active catalyst and the gaseous reactant, but also minimizes the electric resistance created by the non-conductive gas bubbles of product that form on the electrode surface. Currently, the industry standard is a hybrid (or asymmetric) solution, where a liquid compartment (usually the anode) is separated from a gaseous compartment where the cathodic reaction takes place on the GDE. Moreover, the GDE is physically pressed on the separator to obtain a Membrane Electrode Assembly (MEA) to facilitate cell manufacture. Variation of this design exists and most recently A. Hodges et al.[8] proposed an EC design with a double gas compartment, where the membrane is dipped in the electrolyte and exploits capillary forces to keep the membrane always hydrated and conductive.

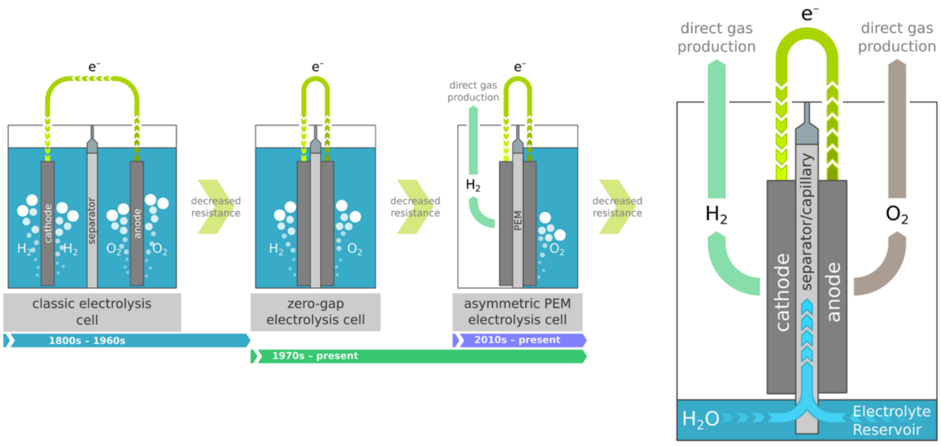

Figure 1.2 Historic evolution of water electrolysis cell architectures culminating in the direct production of one of the gases in the asymmetric EC, and a Capillary-Fed Electrolysis cell recently proposed by A. Hodges et al.[8] Reprinted with permission. Copyright © 2022 by the authors.

Being part of the MEA, the membrane composition is of course fundamental to correct functioning of the device. The membrane main purpose is the separation of the two cell compartments given the dangerous nature of reactants and products (in the simplest FCs, hydrogen and oxygen gas must be supplied to the anode and cathode respectively). The membrane is also a structural component as it anchors the GDE to the assembly and can be subject to hydrostatic pressures from one or both sides. The chemical (i.e. semipermeability) and physical (structural) characteristics of many membranes are tailormade to fit particular working conditions. For example, PolyTetraFluoroEthylene (PTFE), PolyEthylene Terephthalate (PET) and PolyKetone (PK) have all been used as backbones of different membranes for their chemical inertness and physical properties, while the permeability to charge carrier is guaranteed, as an example, by terminal sulfonate groups in Nafion® 117 and imidazolium in Sustainion® membranes. Finally, the electrolyte nature influences both the membrane and the electrode, being in contact, by design, with all parts of a FC/EC. PEMs for example, use Nafion® membranes that can transport protons and need acid-stable catalysts (usually metals from the platinum group). On the other hand, Sustainion®, as many other, are suitable for alkaline electrolytes and many catalysts are stable at higher pHs, enabling the use of earth abundant metals in cheaper AEM cells.

To this day, commercial fuel cells represent the most efficient way to turn chemical energy in electrical power, with the most performing FCs in production exceeding 90% efficiency,[9] while natural gas turbines rarely touch efficiency over 35%.[10] Moreover, FCs and ECs offer a way to store and use electrical energy with low environmental impact, limiting the production of sulfur and nitrogen oxides, sooths, particulate and CO_2 produced from combustion. Finally, a powerful aspect of all fuel cell and electrolyzer applications is their modular nature. Typically (not unlike batteries) a single device is rated for low power profiles, but they can be connected in series or in parallel to increase either operative voltage or current. This creates so called *stacks,* where many cells are connected together and controlled by a single circuit board. Another strong advantage could be represented by the possibility of a fuel cell and electrolyzer to be implemented in the same device.[11] The reversibility between the two modes of operation would unlock the possibility to store and release energy, not unlike batteries, but in a much more stable chemical bond (i.e. not subject to discharge over time).

1.2 Basics of Electrochemistry and Electrocatalysis

Electrochemistry is the study of the interaction between matter and an electrical potential. The most studied events in electrochemistry are those electrode processes where, at the *electrode - electrolyte* interface, matter can react with the imposed potential. Faradaic processes (i.e. redox reactions), for example, can be studied through chronoamperometry analysis (for a more in depth vision on electrochemical components and techniques see Chapter 2), in which the currents registered by a potentiostat are plotted against elapsed time. This is because the current flow is directly related to the moles of reagent consumed, through the relation:

$$Q = \int_{t_0}^{t_1} i(t)\, dt = n\, F\, n_R \qquad (1)$$

where Q is the charge, equal to the area under the current curve, n is the number of electrons exchanged in the redox reaction, F is the Faraday's constant (i.e. 96485 C mol^{-1}) and n_R is the moles of reagent consumed. While the reagent R is consumed and the product P forms, diffusion (following Fick laws) will equalize their local and bulk solution concentration. These are just some of the possible events at the interface. In fact, an unavoidable consequence of an applied potential is the "charging" of the electrode – electrolyte interface: free charges (holes or electrons) accumulate on the electrode while in the electrolyte there is a buildup of the opposite ions, directly resulting in the formation of a double layer (i.e. a capacitor), and thus of a *capacitive* current readable by the potentiostat.

It is important to note that experimentally, an isolated boundary cannot work without a second electrode to close the circuit. The minimal setup needed for an electrochemical study is a cell, and the simplest cell is two electrodes separated by an electrolyte (Fig. 1.3a). Of course, in laboratories around the world many types of cells with varying designs and amounts of electrodes (an example with three electrodes is shown in Fig. 1.3b, but four and five electrodes setups are not unheard of) have been used, in order to have control on selected parameters that help better describe the chemistry involved in electrochemical reactions.

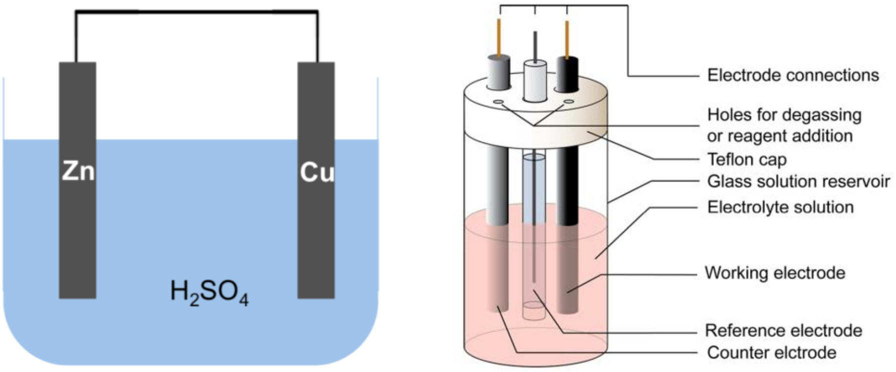

Figure 1.3 (a) An example of the simplest electrochemical cell possible and (b) schematics of a typical setup for a single cell configuration. Copyright 2021 American Chemical Society.[12]

The most used configuration, and the one that is been used throughout this thesis, is the three electrodes setup: a working electrode, at which the reaction of interest takes place, the counter electrode, that closes the circuit to keep the electron balance, and the reference electrode, whose potential is steady (i.e. non-polarizable) and can be used as a frame of reference (hence the name) to measure the other electrodes potentials. Usually, and throughout this thesis, potentials are expressed versus the Reversible Hydrogen Electrode (RHE) reference system, although practically they are measured with other types of reference electrodes (in our case either the Saturated Calomel Electrode, SCE, or the Silver/Silver Chloride electrode, Ag/AgCl). This is done for ease of comparison between scientific articles and it is one of the corrections that are applied to electrochemical data before publication. Other corrections are needed to obtain a more accurate picture of the system at the interface and are pH and ohmic corrections to potentials, as well as the background correction on currents. A more detailed discussion on what, where and why corrections were employed, can be found in section 2.1 on electrochemical techniques.

Electrocatalysis studies the kinetics of electrode processes and its dependence from electrode material, electrolyte composition and many other factors. These factors directly affect the voltages and currents that flow through fuel cells and electrolyzers and must be optimized and calibrated to obtain specific power profiles. In an oversimplified view, the working voltage of an electrochemical cell could be considered as dictated by the thermodynamic potentials (E) of the electrode reactions. Actually, this is only one of the contributions to the observed potential (V):

$$\mathrm{V} = \mathrm{E} + \eta + V_{\Omega} + V_t \qquad (2)$$

The other factors in the electrode potential are: the overpotential (η), needed to drive the reaction at reasonable currents, the ohmic loss (V_Ω), the potential drop due to internal resistance in the cell, and the stabilization potential (V_t), or the potential variation due to material degradation during operation.[13] All these contributions result in higher working potentials for electrolyzers (or lower potentials in fuel cells), but also in resistive heating that poses a threat to the stability of the device and its efficiency. Minimizing them is of outmost importance: overpotentials and stabilization can be mitigated through the optimization of the electrode material, while ohmic losses can be lowered by optimizing the cell design. As previously noted, the presence of product bubbles on the electrodic surface is one of the problems in cell optimization, increasing the overall ohmic resistance. The use of GDEs offer a way to limit bubble formation while enhancing reactant mass transport thus boosting the achievable currents. Gas-phase devices typically employ MEAs (Fig. 1.4b) to keep in contact the three phases (i.e. electrode, gas reactant and/or product and electrolyte). Yet, membranes must be permeable to charge carriers to maintain the balance in the system during operation, so polymer membranes are rated for their charge conductivity and their permeability to other chemicals.[14] While their backbone is based on inert and resistant polymers, i.e. Teflon, membranes present functionalities that adapt to specific applications (pH of media, minimal permeability to reactants and products). In particular, Nafion® membranes are one of the most used in the literature and based on a perfluorinated backbones functionalized with sulfonic groups. Such groups allow for hopping of protons and are well suited for low-pH applications, but they have high methanol permeability[15] and they can also react with ammonia forming ammonium salts.[16] Thus, they have complications when used for the Nitrogen Reduction Reaction (NRR) that produces NH_3. On the other hand, Sustainion® membranes (one of the best performing brands of Anion Exchange Membranes, AEM), are functionalized with imidazolium salts and are better suited for alkaline electrolytes but can suffer from CO_2 in solution because of carbonation effects, such as lower pH and lower charge mobility.[17,18] It must be pointed out that market enterprises and lab research have very different needs, so that the most appropriate electrochemical design hinges on the specific purpose. MEAs are really important in device construction because they bring the price down with automation, but in research MEAs can be very costly because of the non-recoverability of the membrane. Use of simpler setups reduces cost in basic electrochemistry tests, where a lot of catalytic materials will not pan out. On the other hand, there are a lot of different experimental setups that are difficult to compare between each other and the translation of interesting results on real devices is not always straightforward.

To better understand the reaction mechanisms and the properties of new catalysts, usually it is simpler to first investigate a simpler system, without membranes or electrodes including multiple interfaces. For this reason, lab scale experiments at a preliminary level are usually carried out in single chamber cells (Fig. 1.4a). This setup presents a single electrolyte for both electrodes, that can be separated with glass frits to minimize product migration. Moreover, the working electrode has low geometric surface area (in our case 0.196 cm^2) so the quantities being produced during operation are not dangerous. Once some interesting materials have been found, more in dept testing can be done on different setups with varying electrodes and with the addition of a membrane (more information on setup used in this thesis are presented in Chapter 2).

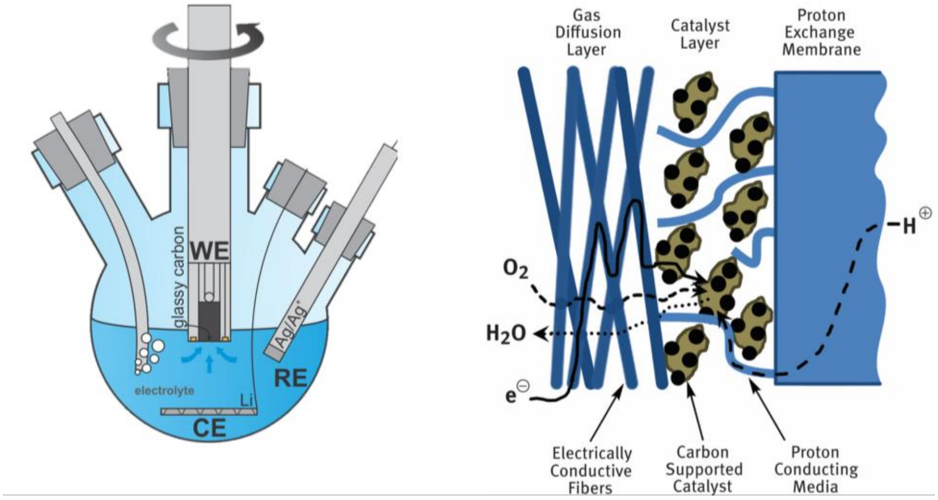

Figure 1.4 Differences between a simple single cell setup (left) and the typical Membrane Electrode Assembly configuration in a dual chamber cell (right)

The main focus of electrocatalysis research is, then, the minimization of Eq. (2) for different catalytic reactions. Given the different chemical nature and properties of reactants in the above-mentioned processes, catalysts often need to be tailored to accommodate the thermodynamic requirements. This is especially true for setups where there is competition between two possible reactions on the catalyst surface and rationalization of chemical characteristics is needed to understand why some pathways are favored instead of others. One of the ways in which chemists tackle these difficulties makes use of the so-called volcano plots. In these plots, the energetics for reagent adsorption (ΔG_{R*}) can be related to empirical data, such as the peak currents or the overpotential showed by the catalysts.[19] The name is directly related to the shape of the plot, that usually peaks at middle values of adsorption energy (Fig. 1.5). This is because if the reagent is bound too freely to the catalyst surface, detachment is the main result, while for very high adsorption energies, usually, it is difficult to remove the products, limiting the reaction turnover frequency.

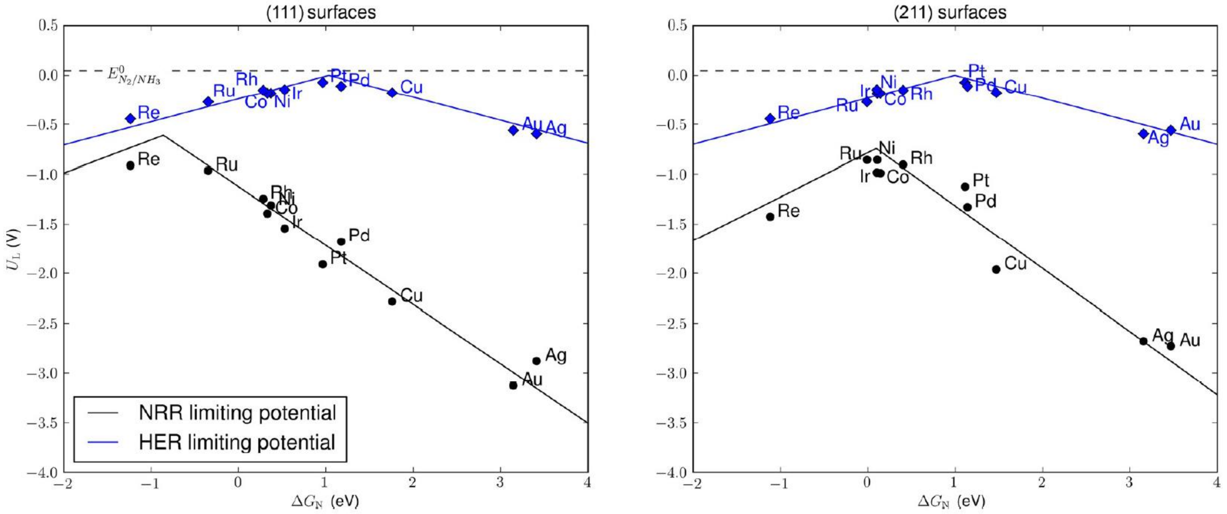

Figure 1.5 Comparison of HER and NRR volcano plots on different transition metals. In this case, the adsorption energies of N* on metals were plotted against the limiting potentials shown for NRR (black line) and HER (blue line). Moreover, Montoya *et al.* calculated the binding energy for both (111) crystallographic surfaces (left) and (211) (right). Reproduced with permission from [20].

Even with the limitation of such plots (that only consider one thermodynamic value to rationalize catalytic activity), it can be seen that different reactions will have different "sweet spots" to boost some reaction and not others.[20] The chemistry of some reactant can also suggest other types of considerations: the N-N triple bond is a very difficult bond to cleave; one of such ways is the use of d block metals that can donate electron density in the anti-bonding molecular orbitals of N_2, weakening the triple bond nature.[21,22] Moreover, a catalytic process with many steps can result in different products. Usually, research focuses on catalysts that can maximize the production of a single chemical over all the others. One example is the CO_2RR, where carbon dioxide can be reduced to a variety of products: CO, formic acid, methane, methanol, ethylene, ethane and ethanol are only the most common (and "easiest" to produce).[23] Computational studies of the reaction pathway on the catalytic surface can shed a light on a very complicated process in which most intermediates can both detach and become products or be reduced further.[24]

Finally, one must take into consideration that rarely real conditions are similar to simulations, or even laboratory tests. Again, a blatant example is the CO_2RR, where usually CO_2 is supplied as a pure gas to the electrode. This would be very expensive in a realistic context, where purification and concentration of gases takes energy and has high costs. This implies that the transition from preliminary scrutiny in the lab and real application will add complications, such as the lower CO_2 concentrations to be used *on the ground,* in comparison with laboratory tests. Moreover, catalyst tests will have to check the compatibility with common contaminants of CO_2 streams (such as O_2 when air is used, and O_2, SO_2 and NO_x when industrial flue gas is used) to understand the impacts on selectivity and stability of these materials. If these problems are not addressed, the purification cost of reagents will negatively impact the implementation of electrolysis as a viable alternative to the industry status quo.

1.3 Nanotechnology for electrocatalysis

The nature of the electrodic surface is central to the optimization of electrochemical devices. In this case, “nature” does not stand only for the material chemistry (i.e. platinum, gold or non-precious metals) but also the morphology of the material. Nanotechnology is a very powerful tool because it can not only increase greatly the surface areas of the electrodes (where all electrodic reactions occur), but also changes dramatically the properties and behavior of the material. The surface area effect is somehow intuitive, (volume increases as R^3 and surface area increases as R^2, see Fig 1.6), while the difference in reactivity behavior of the material between the bulk and nanometric scale is more nuanced and complex.

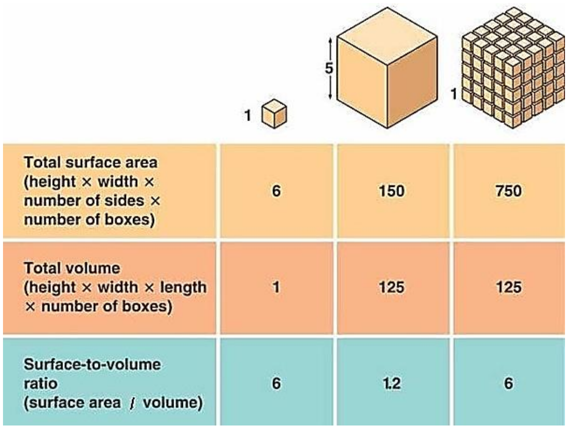

Total surface area (height × width × number of sides × number of boxes)	6	150	750
Total volume (height × width × length × number of boxes)	1	125	125
Surface-to-volume ratio (surface area / volume)	6	1.2	6

Figure 1.6 Different scalability between volume and surface area explained with cubes. The volume between the big cube and the ensemble of smaller cubes is conserved, but the surface area for the latter is 5x and can boost electrodic reactions in a theoretical catalyst.

One of the most famous examples is gold: bulk gold is famous for its inertness, extending also to catalytic reactions. When small nanoparticles of gold are supported on metal oxides, its chemistry dramatically changes.[25] The first applications to use gold’s outstanding catalytic activity in this form were pioneered by Haruta *et al.* in the late ‘80s, early ‘90s with applications from odor removal to gas sensor.[26,27] One of the factors that changes the reactivity with particle dimensions is the surface atoms coordination.[28] All surface atoms suffer from undercoordination (or different functionalization, as in SiO_2 with Si-OH terminal bonds) but smaller nanoparticles present higher undercoordination.[29] This is because the lower the diameter, the higher will be the concentration of edge and corner sites where the surface atom can be active in adsorption of molecules and catalysis

(Fig. 1.7). Another common way to exploit these reactive spots, is the synthesis of anisotropic shaped nanoparticles. Different shapes can preferentially expose some feature (or, if the nanoparticle is crystalline, some crystallographic facets) of the nanoparticle over the others (e.g. nanospikes[30]). Finally, the nanometric dimension of NPs results in quantum confinement, where the energy levels of the NPs electronic bands are conditioned by the dimensions of the nanoparticle itself. This flexibility could allow fine-tuning in electrocatalysis, where the Fermi level of the material is fundamental to enhance the redox kinetics.[31]

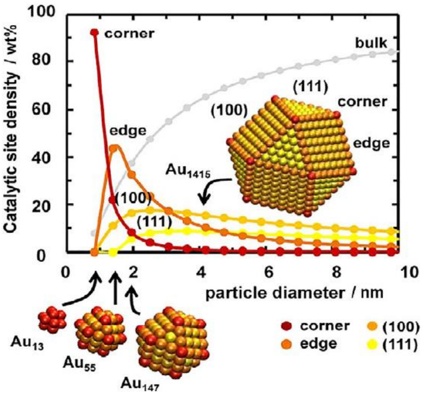

Figure 1.7 Size-dependent distribution of surface sites on Au NPs. Adapted and reprinted with permission from Ref. [29]. Copyright (2012) American Chemical Society.

In general, due to the strong correlation between shape, dimension and activity, it is preferable to assess catalytic nanoparticles with sizes as monodispersed as possible, so that meaningful correlations can be established. Many techniques have been developed to enhance nanometric catalysts (Fig. 1.8). For example, porous structures have been designed to maximize surface area where molecules can react.[32] Porosity can be either intrinsic to the chemical structure[33] or been created through post-synthetic modification, for instance by etching of alloyed NPs.[34] Moreover, NPs surfaces are less stable in the nanometric regime: to limit clustering, that can limit accessibility of their surface to reactants, nanoparticles can be deposited on substrates, called “supports”. The materials acting as supports in electrochemistry can have many characteristics: they should preferably be cheap, conductive and give some synergistic effect during catalysis. The conductivity of the support is of paramount importance to compensate for those nanoparticles that present low charge mobility (i.e. low conductivity) such as metal oxides. In these cases, the supports may function as electron wells to favor the electrodic kinetics. Finally, the close contact between NP and support implies an orbital interaction between the two, so that the electronic structure of the nanoparticle could be altered by its chemical environment (i.e. polarity of a functional group on the support lattice). Supporting materials allowed the synthesis of structures that are now at the forefront of catalysis, that were previously very difficult to obtain given the reactivity of such unstable chemical entities.

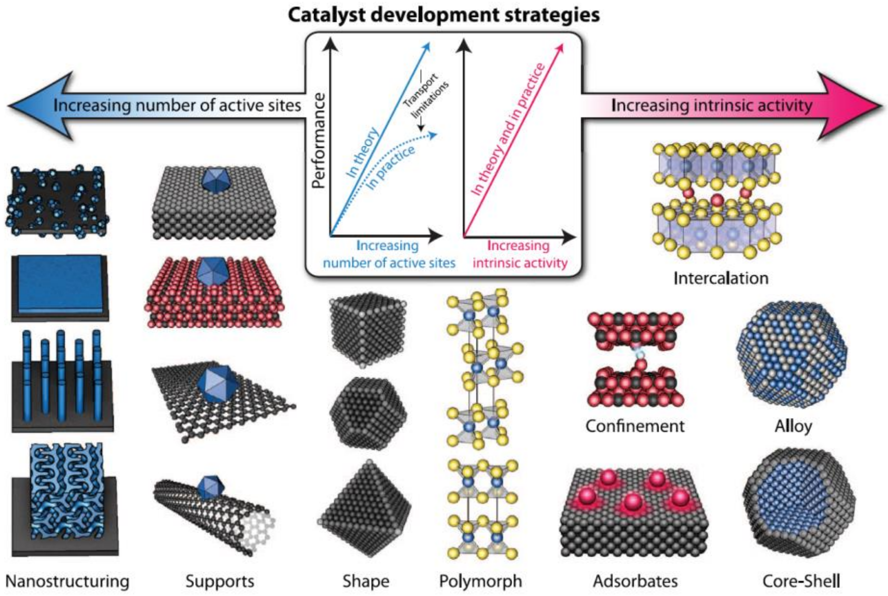

Figure 1.8 Schematic of various catalyst development strategies, which aim to increase the number of active sites and/or increase the intrinsic activity of each active site. Reproduced with permission from ref. [35]. Copyright © 2017, American Association for the Advancement of Science.

From all the proposed supports, carbon materials have emerged as one of the most utilized in the literature because of their flexibility and low cost. Carbon nanostructures (CNS) can be synthetized with an almost infinite variety and thus tailor-made to specific catalytic necessities (i.e. surface acid sites, hydrophilicity, etc.) [36] both as a standalone catalyst or as support for NPs.

1.3 Carbon nanomaterials for electrocatalysis

In the last decades a lot of work has been done focusing on the development of new methodologies and optimal reaction conditions for the synthesis of carbon-based nanomaterials. In general, two approaches can be distinguished: bottom-up and top- down techniques. Top-down strategies break down bigger structures to obtain nanoscale materials. These approaches are mostly used for carbon-based nanomaterials; pyrolysis is a common way to obtain fullerenes, nanotubes (CNT) and nanodots (CND). For carbon-based sheets (Graphene family) chemical and physical exfoliation are also important methodologies. On the contrary, the bottom-up methods take advantage of common chemical reactants (low MW carbon-containing molecules) to assemble into nanoscale structures. Popular bottom-up approaches are Chemical Vapor Deposition (CVD), Physical Vapor Deposition (PVD) but also polymerization through pyrolysis (as in the case of graphitic carbon nitride). In general, top-down approaches are subject to low purity or lengthy workups but are also quite inexpensive. On the contrary, bottom-up is still the preferred method to achieve high purity nanomaterials with very small polydispersity (PDI), given their more controlled nature, but suffer from higher costs. Doping (the introduction of impurities for the purpose of modulating its properties) is arguably the most important technique for carbon-based materials. It can be accomplished by using precursors containing the elements of interest or by first synthetizing the material and then functionalizing it through chemical reactions. Many catalysts based on CNTs and graphene often rely on this second route, subjecting the materials to oxidations (to increase oxygen content) or to heat treatments in presence of ammonia (for N functionalization). Other types of carbon (e.g. amorphous NDs, porous carbon matrixes), on the other hand, follow a bottom-up synthetic procedure, where molecules with different elements can be chosen to impart peculiar characteristics to the final product. With the use of more than one precursor at a time, it is also possible to manage inclusions in the carbon lattice, such as carefully controlling ratios between dopants or creating sites with metallic centers (in the case of SACs). In general, a wide number of studies have focused on carbon-based catalysts (Fig. 1.9) starting from the more classical approach of monodoped porous carbon materials (common to the field of CO_2RR and ORR reactions)[37–41] to the more complex co-doping heteroatom strategy,[42–45] and furthermore to tuning of edge sites and topological intrinsic defects in the carbon matrix. In this context, experimental as well as computational analysis can shed light on the critical features for the specific reactant activation. This step is necessary to further the effort to synthetize structures optimized for an electrocatalytic reaction.

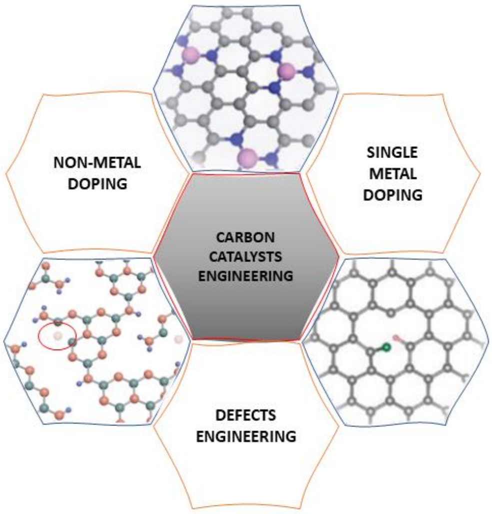

Figure 1.9 Relevant techniques for carbon catalyst activation and their main combinations. Reproduced with permission from ref. [46] Copyright © 2021 by the authors.

1.3.1 Defect engineering on carbon nanostructures

An analysis of the state of the art concerning carbon-based electrocatalysts reveals that the exploitation of vacancies represents one key concept to extensively investigate the role of carbon and its catalytic properties. Intrinsic defects in the lattice can directly function as the potential active site due to an altered surface charge state. Moreover, the presence of neighbor heteroatoms can greatly increase the possible interaction of C atoms with specific molecules or atoms, for example favoring the adsorption of small reacting molecules (e.g. O_2, CO_2) or stabilize metal species (i.e. SACs). Carbon vacancies (CV) are the simplest lattice defects. The potential activity of carbon sites is most exemplified in the case of the Defective reduced Graphene Oxide (DrGO)-based electrocatalyst with engineered defects, reported by Zhang et al.[47] Through computational and experimental analysis, the group was able to pin the high activity shown by the material toward NRR (~22.0% at −0.116 V in acidic media) to the CVs created by the hydrothermal treatment, leading to unsaturated carbon sites (oxygen-containing functional groups, structural defects in the basal plane, and on edge sites). The computational part of the study showed, in particular, that $*N_2$ was most active on sites with a double vacancy (DrGO-DV), while on single CVs (DrGO-SV) and on terminal –COOH groups, the energetics where much less favorable. (Fig. 1.10)

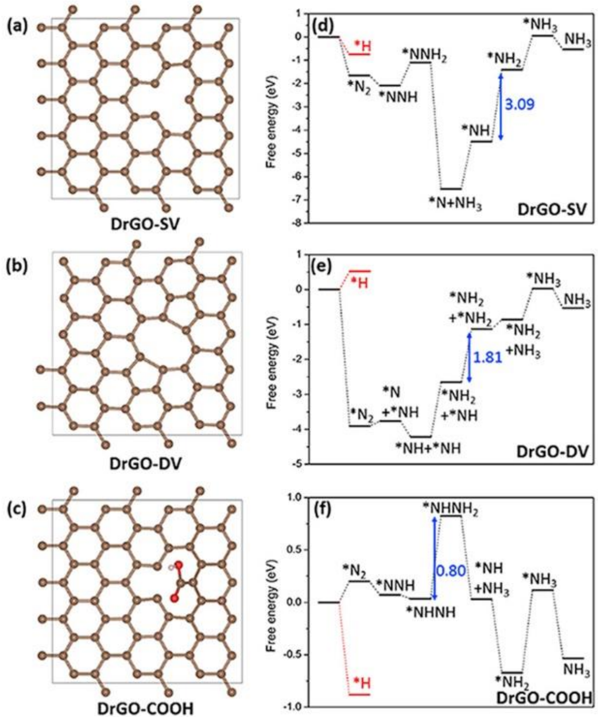

Figure 1.10 Different defects on DrGO: single Carbon Vacancy (a), double Carbon Vacancy (b), and carboxylic carbon (c). Energetics for main NRR intermediates on these defects are re-ported on the right side (d–f). Reprinted with permission from [47]. Copyright 2019 Elsevier Ltd.

Oxygen Vacancies (OVs) and Nitrogen Vacancies (NVs) have also received wide attention in metal oxides catalysts, but carbon-based materials have also shown catalytic improvements with pyrolytic treatments. The ability of intrinsic defects on carbon nanostructures to function as active site or support (for the active component in a nanocomposite) will be more apparent in the next paragraphs, where metal and non-metal doping will be discussed.

1.3.2 Non-metal doped carbon nanostructures

If oxygen and nitrogen represent the most frequent dopants in carbon-based nanostructures, boron,[48,49] fluorine,[50,51] phosphorus[52,53] and sulfur[54,55] have all been reported to augment the activity of carbon-based electrocatalysts.[56] Each element can serve in modifying the charge density on the carbon lattice, functioning as an EDG/EWG (Electron Donating/Withdrawing Group). Of course, more than one atom can be introduced in the carbon framework, to mix and match possible effects on the final nanomaterial, expanding the range of possibilities. That said, the ease of introduction in CNS of oxygen and nitrogen and their powerful effects on the material properties, make these two elements of highest relevance. In particular, oxygen content can modulate the hydrophilicity of the final material[57] and it is easily controllable through oxidation (with oxidizing acids, ozone treatment, oxygen containing precursors, etc.) and reduction (heat treatment in H_2-Ar or Ar atmosphere). The effect of varying oxygen content was studied for H_2O_2 electrosynthesis through ORR by Lu et al.[58] on several different carbon nanostructures (Fig. 1.11). The differences in oxidation were controlled simply with reaction time: a slurry was created with the insoluble carbon and an oxidizing acid (HNO_3), and the reaction was let go between 6 and 48h. Using DFT calculations, the group was able to construct a volcano plot with the limiting potentials of different C-O features on the carbon vs their binding energies for *OOH. The most active site on these oxidized carbons was the basal C-O-C functionality, displaying near zero overpotential. Similarly, other researchers have directly pointed to the importance of epoxy groups on the carbon lattice.[59,60]

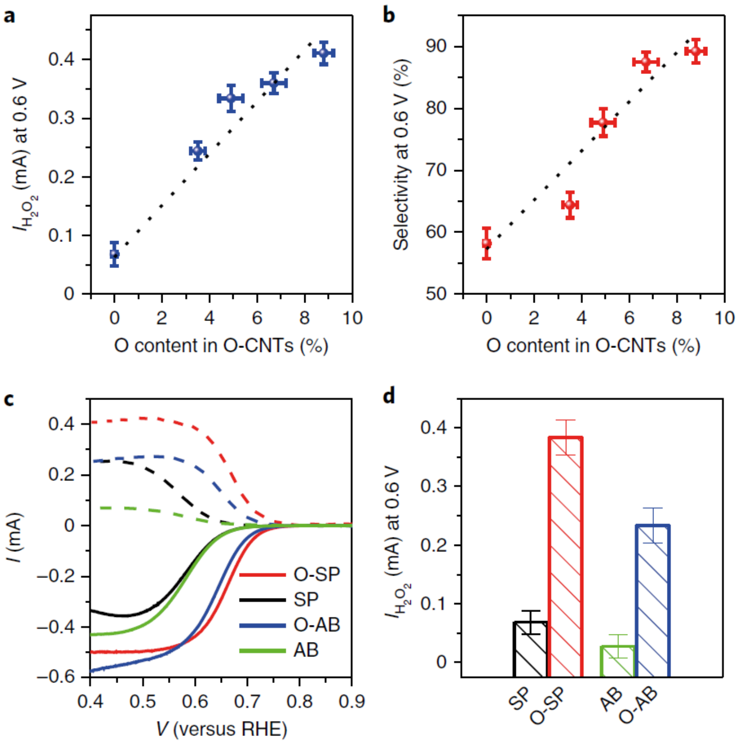

Figure 1.11 Plots of H_2O_2 current (a) and selectivity (b) at 0.6 V as a function of oxygen content for O-CNTs with various oxidation times, both the activity and selectivity correlate linearly with the oxygen content. c, Polarization curves at 1600 r.p.m. (solid lines) and ring currents (dashed lines) for Super P carbon (SP), Acetylene Black (AB) and their oxidized derivatives. d, H_2O_2 current (0.6 V) comparison of SP, O-SP, AB and O-AB, suggesting that the oxidation process is generally applicable for carbon materials. Reprinted with permission from ref. [58]. Copyright © 2018, © The Authors 2017, under exclusive licence to Macmillan Publishers Ltd, part of Springer Nature.

On the other hand, nitrogen doping is mainly controlled by using nitrogenated precursors, even if some N-doping can be created also through chemical treatment, such as thermal treatment in the presence of ammonia.[61,62] The type of nitrogen present in the precursor (pyrrolic, pyridinic) is of paramount importance to modulate the final material characteristics.[41,63,64] A powerful application of nitrogen doping is through its chelating ability toward most metals. This ability can be exploited for example in the formation of Metal Organic Frameworks (MOFs)-based materials[65]: Zinc Imidazolate Framework (ZIF) is of particular importance because zinc can be sublimated out of the material through pyrolysis leaving highly porous nitrogen doped carbon 3D matrixes that can be used in catalysis.[66] Moreover, a multitude of natural proteins contain the porphyrin structure, that can host many metallic elements. Using bio-mimetic ideas, porphyrin-like structures can be incorporated into the carbon framework to stabilize single metallic species.[67] This strategy is especially important for SACs, where the metal center must be stabilized in order to withstand the catalytic turn-over without detaching from the support.

1.3.3 Metal doped carbon nanostructures and metal-carbon nanocomposites

Metal-carbon nanocomposites are perhaps the most important class of catalysts because of the good overlap between different Transition Metals (TMs) HOMOs with reactants LUMOs. As an example, the current commercial standard for many electrochemical applications are platinum and iridium oxide nanoparticles supported on carbon.[68] Materials such as metal oxides,[69] nitrides,[70] sulfides,[71] phosphides[72] are in the most researched branch of catalysts. These materials are often not conductive enough and can be coupled with carbon to form nanohybrids that offer carbon-like conductivity and metal-derived activity. This approach is not without drawbacks: the active catalyst can suffer, during catalysis, of many deactivating processes. Coke formation on CO_2RR catalysts,[73] pore flooding,[74] demetallation[75] are all possible routes for rapid activity decay. Following recent trends in nanoparticles synthesis, many efforts have been focusing on anchoring single transition metal atoms on different supports. SACs, in a way, bridge the gap between metal complexes, i.e., homogeneous catalysis, with the bulk heterogeneous catalysts. The single-atom nature of these material allows for much larger mass activities, addressing the issues of atom economy, one of the critical aspects for the transfer to the industry. In this landscape, carbon-based material arose as a natural support structure, given their low price, ease of functionalization, and ability to stabilize TM atoms thanks to heteroatom doping (e.g., TM-N_4 structures). The SACs concept brings however its own challenges: to avoid the formation of nanoparticles, different synthetic routes were studied but, generally, it is still difficult to obtain high metal loadings without nanoparticles' formation, with notable exceptions.[76] Thus, to ensure the atomic dispersion, SACs loading is often lower than 1% [65–68] because the single atoms, as their loading increases, usually have a higher tendency to stick together and form clusters or even nanoparticles.[77–80] The low loading of many SACs translate in impressive figures for mass activity (current normalized for the metal loading), but usually need high volumes of material, due to the limited number of active sites.

Another issue to address is the possibility of these synthetic procedures to be scaled up to industrially significant methods.[81] Li et al.[82], for example, managed to synthetize a Fe-SAC anchored trough the N_4 features of graphitic carbon nitride with a simple impregnation technique. The best performing material was determined to have a Fe loading of 1.2% and showed how the confinement of an iron atom can amplify its activity toward CO_2RR in respect to be single components of this nanocomposite material (fig. 1.12c). Moreover, the SAC was also different from the parent materials for its selectivity toward CO, showing over 90% selectivity in the -0.5 ~ -0.6 V range.

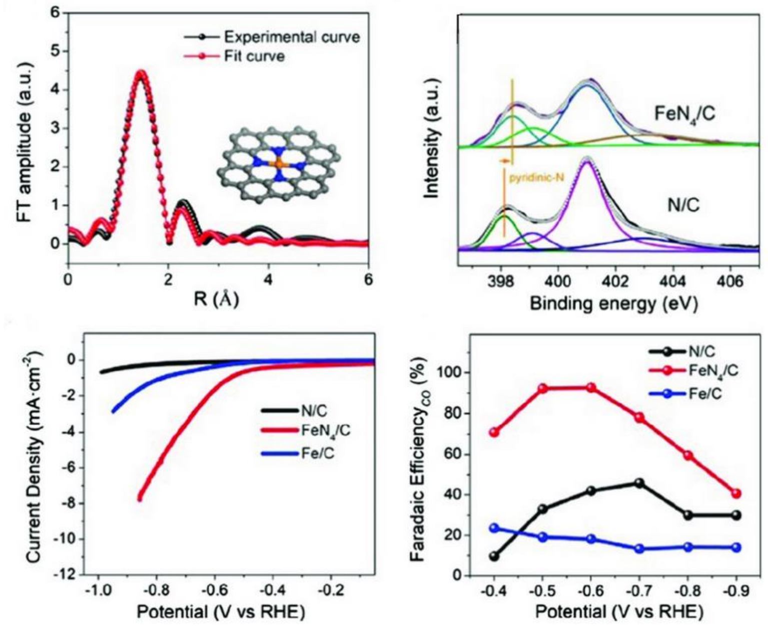

Figure 1.12 (a) EXAFS fitting curve for FeN$_4$/C. Inset is the schematic model of FeN$_4$ structure, with Fe in orange, N in blue, and C in gray. (b) N 1s XPS spectra of FeN$_4$/C and N/C. (c) LSV curves (iR-corrected) of N/C, FeN4/C, and Fe/C. (d) Faradaic efficiencies of N/C, FeN$_4$/C, and Fe/C for CO. Adapted with permission from [82]. Copyright © 2021 by the authors.

SACs, together with similar materials (DACs, clusters, etc.) represent the forefront of electrocatalytic materials. Until recently, studies of electrocatalysts with atomic features had been mostly based on theoretical insights.[83–92] In the last few years, many works have managed to synthetize these kind of structures with many different TMs, with interesting applications.[93–95] Finally, even if computational studies have suggested the stability of these materials, given the intricacies of electrocatalysis, it is critical to assess their continued activity against poisoning, breakage, and deactivation.

1.4 Motivations and scope

Electrocatalysis has been the subject of increasing academic and industrial interest in the last decades. Electrolysis is already a staple in many industrially relevant reactions, such as the chloroalkali process for the synthesis of sodium hydroxide and many electrometallurgic reductions (e.g. aluminum, sodium and potassium). The processes that will be explored in this thesis are at the forefront of the electrochemistry research because they could unlock the widespread adoption of fuel cell and electrolyzer technology in a more small-scale and decentralized manner then before.

These devices will also be instrumental in the implementation of the circular economy, taking advantage of the carbon cycle and hydrogen-oxygen recombination/water splitting. In this landscape, carbon-based hierarchical nanostructures are seen as the most promising catalysts: on one side, carbon is cheap, easy to functionalize and highly conductive; on the other side, many metal and metal oxide nanoparticles can be supported, stabilized and/or activated by carbon nanotextures. My research, then, focused on advanced synthetic methods coupled with morphological, textural but most of all, electrochemical analysis. Moreover, the setup of specific electroanalytical approaches that I developed in relation to NRR catalysis will help future research in our laboratory with preliminary screening and stability testing. Finally, a more "real life scenario" testing has begun in collaboration with prof. Baltrusaitis group in Lehigh University (Bethlehem PA, USA) to characterize copper and tin oxide nanoparticles during use with simulated flue gas (a mixture of N_2, CO_2 and SO_2) for industrial application.

1 References

(1) International Energy Agency. *World Energy Outlook 2021*; 2021.

(2) Freeman, D. China and Renewables: The Priority of Economics over Geopolitics. *Lecture Notes in Energy* **2018**, *61*, 187–201. https://doi.org/10.1007/978-3-319-67855-9_7.

(3) Das, S. Achieving Carbon Neutrality in the Global Aluminum Industry. *JOM* **2012**, *64* (2), 285–290. https://doi.org/10.1007/S11837-012-0237-0.

(4) A. Paets van Troostwijk. Null. *Algem. Mag. Wetensch. Kunst Smaak* **1790**, *4*, 909.

(5) VII. Experiments and Observations, Made with the View of Ascertaining the Nature of the Gaz Produced by Passing Electric Discharges through Water. *Philosophical Transactions of the Royal Society of London* **1797**, *87*, 142–158. https://doi.org/10.1098/RSTL.1797.0008.

(6) W.R. Grove. LXXII. On a Gaseous Voltaic Battery. *The London, Edinburgh, and Dublin Philosophical Magazine and Journal of Science* **1842**, *21* (140), 417–420. https://doi.org/10.1080/14786444208621600.

(7) Ogawa, T.; Takeuchi, M.; Kajikawa, Y. Analysis of Trends and Emerging Technologies in Water Electrolysis Research Based on a Computational Method: A Comparison with Fuel Cell Research. *Sustainability 2018, Vol. 10, Page 478* **2018**, *10* (2), 478. https://doi.org/10.3390/SU10020478.

(8) Hodges, A.; Hoang, A. L.; Tsekouras, G.; Wagner, K.; Lee, C. Y.; Swiegers, G. F.; Wallace, G. G. A High-Performance Capillary-Fed Electrolysis Cell Promises More Cost-Competitive Renewable Hydrogen. *Nature Communications 2022 13:1* **2022**, *13* (1), 1–11. https://doi.org/10.1038/s41467-022-28953-x.

(9) Blum, L.; Deja, R.; Peters, R.; Stolten, D. Comparison of Efficiencies of Low, Mean and High Temperature Fuel Cell Systems. *International Journal of Hydrogen Energy* **2011**, *36* (17), 11056–11067. https://doi.org/10.1016/J.IJHYDENE.2011.05.122.

(10) *How Gas Turbine Power Plants Work | Department of Energy*. https://www.energy.gov/fecm/how-gas-turbine-power-plants-work (accessed 2022-06-08).

(11) Graves, C.; Ebbesen, S. D.; Jensen, S. H.; Simonsen, S. B.; Mogensen, M. B. Eliminating Degradation in Solid Oxide Electrochemical Cells by Reversible Operation. *Nature Materials* **2015**, *14* (2), 239–244. https://doi.org/10.1038/NMAT4165.

(12) Elgrishi, N.; Rountree, K. J.; McCarthy, B. D.; Rountree, E. S.; Eisenhart, T. T.; Dempsey, J. L. A Practical Beginner’s Guide to Cyclic Voltammetry. *Journal of Chemical Education* **2018**, *95* (2), 197–206. https://doi.org/10.1021/ACS.JCHEMED.7B00361.

(13) Trasatti, S. Electrochemistry and Environment: The Role of Electrocatalysis. *International Journal of Hydrogen Energy* **1995**, *20* (10), 835–844. https://doi.org/10.1016/0360-3199(95)00014-5.

(14) Dekel, D. R. Review of Cell Performance in Anion Exchange Membrane Fuel Cells. *Journal of Power Sources* **2018**, *375*, 158–169. https://doi.org/10.1016/J.JPOWSOUR.2017.07.117.

(15) Mukoma, P.; Jooste, B. R.; Vosloo, H. C. M. A Comparison of Methanol Permeability in Chitosan and Nafion 117 Membranes at High to Medium Methanol Concentrations. *Journal of Membrane Science* **2004**, *243* (1–2), 293–299. https://doi.org/10.1016/J.MEMSCI.2004.06.032.

(16) Hanifpour, F.; Sveinbjörnsson, A.; Canales, C. P.; Skúlason, E.; Flosadóttir, H. D. Preparation of Nafion Membranes for Reproducible Ammonia Quantification in Nitrogen Reduction Reaction Experiments. *Angewandte Chemie* **2020**, *132* (51), 23138–23142. https://doi.org/10.1002/ANGE.202007998.

(17) Zheng, Y.; Nicole Irizarry Colón, L.; Ul Hassan, N.; Williams, E. R.; Stefik, M.; LaManna, J. M.; Hussey, D. S.; Mustain, W. E. Effect of Membrane Properties on the Carbonation of Anion Exchange Membrane Fuel Cells. *Membranes (Basel)* **2021**, No. 11, 102. https://doi.org/10.3390/membranes11020102.

(18) Piana, M.; Boccia, M.; Filpi, A.; Flammia, E.; Miller, H. A.; Orsini, M.; Salusti, F.; Santiccioli, S.; Ciardelli, F.; Pucci, A. H2/Air Alkaline Membrane Fuel Cell Performance and Durability, Using

Novel Ionomer and Non-Platinum Group Metal Cathode Catalyst. *Journal of Power Sources* **2010**, *195* (18), 5875–5881. https://doi.org/10.1016/J.JPOWSOUR.2009.12.085.

(19) Vijh, A. K. Electrocatalysis of the Electroreduction of Nitric Acid by Metals. *Journal of Catalysis* **1974**, *32* (2), 230–236. https://doi.org/10.1016/0021-9517(74)90071-2.

(20) Montoya, J. H.; Tsai, C.; Vojvodic, A.; Nørskov, J. K. The Challenge of Electrochemical Ammonia Synthesis: A New Perspective on the Role of Nitrogen Scaling Relations. *ChemSusChem* **2015**, *8* (13), 2180–2186. https://doi.org/10.1002/CSSC.201500322.

(21) Zheng, J.; Jiang, L.; Lyu, Y.; Jian, S. P.; Wang, S. Green Synthesis of Nitrogen-to-Ammonia Fixation: Past, Present, and Future. *Energy & Environmental Materials* **2021**. https://doi.org/10.1002/EEM2.12192.

(22) Cui, X.; Tang, C.; Zhang, Q. A Review of Electrocatalytic Reduction of Dinitrogen to Ammonia under Ambient Conditions. *Advanced Energy Materials* **2018**, *8* (22), 1800369. https://doi.org/10.1002/aenm.201800369.

(23) Chatterjee, T.; Boutin, E.; Robert, M. Manifesto for the Routine Use of NMR for the Liquid Product Analysis of Aqueous CO2 Reduction: From Comprehensive Chemical Shift Data to Formaldehyde Quantification in Water. *Dalton Transactions* **2020**, *49* (14), 4257–4265. https://doi.org/10.1039/C9DT04749B.

(24) Todorova, T. K.; Schreiber, M. W.; Fontecave, M. Mechanistic Understanding of CO2 Reduction Reaction (CO2RR) Toward Multicarbon Products by Heterogeneous Copper-Based Catalysts. *ACS Catalysis* **2020**, *10* (3), 1754–1768. https://doi.org/10.1021/ACSCATAL.9B04746.

(25) Haruta, M. Size- and Support-Dependency in the Catalysis of Gold. *Catalysis Today* **1997**, *36* (1), 153–166. https://doi.org/10.1016/S0920-5861(96)00208-8.

(26) Haruta, M.; Yamada, N.; Kobayashi, T.; Iijima, S. Gold Catalysts Prepared by Coprecipitation for Low-Temperature Oxidation of Hydrogen and of Carbon Monoxide. *Journal of Catalysis* **1989**, *115* (2), 301–309. https://doi.org/10.1016/0021-9517(89)90034-1.

(27) Funazaki, N.; Hemmi, A.; Ito, S.; Asano, Y.; Yamashita, S.; Kobayashi, T.; Haruta, M. Development of Carbon Monoxide Detector Using Au Fine Particles-Doped α-Fe2O3. *Sensors and Actuators B: Chemical* **1993**, *14* (1–3), 536–538. https://doi.org/10.1016/0925-4005(93)85080-T.

(28) Reske, R.; Mistry, H.; Behafarid, F.; Roldan Cuenya, B.; Strasser, P. Particle Size Effects in the Catalytic Electroreduction of CO2 on Cu Nanoparticles. *J Am Chem Soc* **2014**, *136* (19), 6978–6986. https://doi.org/10.1021/JA500328K.

(29) Zhu, W.; Michalsky, R.; Metin, Ö.; Lv, H.; Guo, S.; Wright, C. J.; Sun, X.; Peterson, A. A.; Sun, S. Monodisperse Au Nanoparticles for Selective Electrocatalytic Reduction of CO2 to CO. *J Am Chem Soc* **2013**, *135* (45), 16833–16836. https://doi.org/10.1021/JA409445P.

(30) Saberi Safaei, T.; Mepham, A.; Zheng, X.; Pang, Y.; Dinh, C. T.; Liu, M.; Sinton, D.; Kelley, S. O.; Sargent, E. H. High-Density Nanosharp Microstructures Enable Efficient CO2 Electroreduction. *Nano Letters* **2016**, *16* (11), 7224–7228. https://doi.org/10.1021/ACS.NANOLETT.6B03615.

(31) Zhu, Y.; Qian, H.; Jin, R. Catalysis Opportunities of Atomically Precise Gold Nanoclusters. *Journal of Materials Chemistry* **2011**, *21* (19), 6793–6799. https://doi.org/10.1039/C1JM10082C.

(32) Chen, Y. Z.; Zhang, R.; Jiao, L.; Jiang, H. L. Metal–Organic Framework-Derived Porous Materials for Catalysis. *Coordination Chemistry Reviews* **2018**, *362*, 1–23. https://doi.org/10.1016/J.CCR.2018.02.008.

(33) Gonzalez, M. I.; Bloch, E. D.; Mason, J. A.; Teat, S. J.; Long, J. R. Single-Crystal-to-Single-Crystal Metalation of a Metal–Organic Framework: A Route toward Structurally Well-Defined Catalysts. *Inorganic Chemistry* **2015**, *54* (6), 2995–3005. https://doi.org/10.1021/acs.inorgchem.5b00096.

(34) Erlebacher, J.; Aziz, M. J.; Karma, A.; Dimitrov, N.; Sieradzki, K. Evolution of Nanoporosity in Dealloying. *Nature 2001 410:6827* **2001**, *410* (6827), 450–453. https://doi.org/10.1038/35068529.

(35) She, Z. W.; Kibsgaard, J.; Dickens, C. F.; Chorkendorff, I.; Nørskov, J. K.; Jaramillo, T. F. Combining Theory and Experiment in Electrocatalysis: Insights into Materials Design. *Science (1979)* **2017**, *355* (6321). https://doi.org/10.1126/SCIENCE.AAD4998.

(36) Wang, L.; Sofer, Z.; Pumera, M. Will Any Crap We Put into Graphene Increase Its Electrocatalytic Effect? *ACS Nano* **2020**, *14* (1), 21–25. https://doi.org/10.1021/ACSNANO.9B00184.

(37) Iglesias, D.; Giuliani, A.; Melchionna, M.; Marchesan, S.; Criado, A.; Nasi, L.; Bevilacqua, M.; Tavagnacco, C.; Vizza, F.; Prato, M.; Fornasiero, P. N-Doped Graphitized Carbon Nanohorns as a Forefront Electrocatalyst in Highly Selective O2 Reduction to H2O2. *Chem* **2018**, *4* (1), 106–123. https://doi.org/10.1016/J.CHEMPR.2017.10.013.

(38) Melchionna, M.; Fornasiero, P.; Prato, M. The Rise of Hydrogen Peroxide as the Main Product by Metal-Free Catalysis in Oxygen Reductions. *Advanced Materials* **2019**, *31* (13), 1802920. https://doi.org/10.1002/ADMA.201802920.

(39) Duan, X.; Xu, J.; Wei, Z.; Ma, J.; Guo, S.; Wang, S.; Liu, H.; Dou, S. Metal-Free Carbon Materials for CO2 Electrochemical Reduction. *Advanced Materials* **2017**, *29* (41), 1701784. https://doi.org/10.1002/ADMA.201701784.

(40) Wu, J.; Ma, S.; Sun, J.; Gold, J. I.; Tiwary, C.; Kim, B.; Zhu, L.; Chopra, N.; Odeh, I. N.; Vajtai, R.; Yu, A. Z.; Luo, R.; Lou, J.; Ding, G.; Kenis, P. J. A.; Ajayan, P. M. A Metal-Free Electrocatalyst for Carbon Dioxide Reduction to Multi-Carbon Hydrocarbons and Oxygenates. *Nature Communications 2016 7:1* **2016**, *7* (1), 1–6. https://doi.org/10.1038/ncomms13869.

(41) Tuci, G.; Zafferoni, C.; D'Ambrosio, P.; Caporali, S.; Ceppatelli, M.; Rossin, A.; Tsoufis, T.; Innocenti, M.; Giambastiani, G. Tailoring Carbon Nanotube N-Dopants While Designing Metal-Free Electrocatalysts for the Oxygen Reduction Reaction in Alkaline Medium. *ACS Catalysis* **2013**, *3* (9), 2108–2111. https://doi.org/10.1021/CS400379H.

(42) Zhang, X.; Yao, S.; Chen, P.; Wang, Y.; Lyu, D.; Yu, F.; Qing, M.; Tian, Z. Q.; Shen, P. K. Revealing the Dependence of Active Site Configuration of N Doped and N, S-Co-Doped Carbon Nanospheres on Six-Membered Heterocyclic Precursors for Oxygen Reduction Reaction. *Journal of Catalysis* **2020**, *389*, 677–689. https://doi.org/10.1016/J.JCAT.2020.07.003.

(43) You, C.; Liao, S.; Li, H.; Hou, S.; Peng, H.; Zeng, X.; Liu, F.; Zheng, R.; Fu, Z.; Li, Y. Uniform Nitrogen and Sulfur Co-Doped Carbon Nanospheres as Catalysts for the Oxygen Reduction Reaction. *Carbon N Y* **2014**, *69*, 294–301. https://doi.org/10.1016/J.CARBON.2013.12.028.

(44) Zhang, Y.; Zhuang, X.; Su, Y.; Zhang, F.; Feng, X. Polyaniline Nanosheet Derived B/N Co-Doped Carbon Nanosheets as Efficient Metal-Free Catalysts for Oxygen Reduction Reaction. *Journal of Materials Chemistry A* **2014**, *2* (21), 7742–7746. https://doi.org/10.1039/C4TA00814F.

(45) Chen, C.; Sun, X.; Yan, X.; Wu, Y.; Liu, H.; Zhu, Q.; Bediako, B. B. A.; Han, B. Boosting CO2 Electroreduction on N,P-Co-Doped Carbon Aerogels. *Angewandte Chemie International Edition* **2020**, *59* (27), 11123–11129. https://doi.org/10.1002/ANIE.202004226.

(46) Ferrara, M.; Melchionna, M.; Fornasiero, P.; Bevilacqua, M. The Role of Structured Carbon in Downsized Transition Metal-Based Electrocatalysts toward a Green Nitrogen Fixation. *Catalysts 2021, Vol. 11, Page 1529* **2021**, *11* (12), 1529. https://doi.org/10.3390/CATAL11121529.

(47) Zhang, M.; Choi, C.; Huo, R.; Gu, G. H.; Hong, S.; Yan, C.; Xu, S.; Robertson, A. W.; Qiu, J.; Jung, Y.; Sun, Z. Reduced Graphene Oxides with Engineered Defects Enable Efficient Electrochemical Reduction of Dinitrogen to Ammonia in Wide PH Range. *Nano Energy* **2020**, *68*, 104323. https://doi.org/10.1016/J.NANOEN.2019.104323.

(48) Yu, X.; Han, P.; Wei, Z.; Huang, L.; Gu, Z.; Peng, S.; Ma, J.; Zheng, G. Boron-Doped Graphene for Electrocatalytic N2 Reduction. *Joule* **2018**, *2* (8), 1610–1622. https://doi.org/10.1016/J.JOULE.2018.06.007.

(49) Mao, X.; Zhou, S.; Yan, C.; Zhu, Z.; Du, A. A Single Boron Atom Doped Boron Nitride Edge as a Metal-Free Catalyst for N2 Fixation. *Physical Chemistry Chemical Physics* **2019**, *21* (3), 1110–1116. https://doi.org/10.1039/c8cp07064d.

(50) Wang, W.; Lu, X.; Su, P.; Li, Y.; Cai, J.; Zhang, Q.; Zhou, M.; Arotiba, O. Enhancement of Hydrogen Peroxide Production by Electrochemical Reduction of Oxygen on Carbon Nanotubes Modified with Fluorine. *Chemosphere* **2020**, *259*, 127423. https://doi.org/10.1016/j.chemosphere.2020.127423.

(51) Liu, Y.; Li, Q.; Guo, X.; Kong, X.; Ke, J.; Chi, M.; Li, Q.; Geng, Z.; Zeng, J. A Highly Efficient Metal-Free Electrocatalyst of F-Doped Porous Carbon toward N2 Electroreduction. *Advanced Materials* **2020**, *32* (24), 1907690. https://doi.org/10.1002/ADMA.201907690.

(52) Wu, J.; Yang, Z.; Sun, Q.; Li, X.; Strasser, P.; Yang, R. Synthesis and Electrocatalytic Activity of Phosphorus-Doped Carbon Xerogel for Oxygen Reduction. *Electrochimica Acta* **2014**, *127*, 53–60. https://doi.org/10.1016/J.ELECTACTA.2014.02.016.

(53) Hu, X.; Fan, M.; Zhu, Y.; Zhu, Q.; Song, Q.; Dong, Z. Biomass-Derived Phosphorus-Doped Carbon Materials as Efficient Metal-Free Catalysts for Selective Aerobic Oxidation of Alcohols. *Green Chemistry* **2019**, *21* (19), 5274–5283. https://doi.org/10.1039/C9GC01910C.

(54) Xia, L.; Yang, J.; Wang, H.; Zhao, R.; Chen, H.; Fang, W.; Asiri, A. M.; Xie, F.; Cui, G.; Sun, X. Sulfur-Doped Graphene for Efficient Electrocatalytic N2-to-NH3 Fixation. *Chemical Communications* **2019**, *55* (23), 3371–3374. https://doi.org/10.1039/C9CC00602H.

(55) Li, W.; Yang, D.; Chen, H.; Gao, Y.; Li, H. Sulfur-Doped Carbon Nanotubes as Catalysts for the Oxygen Reduction Reaction in Alkaline Medium. *Electrochimica Acta* **2015**, *165*, 191–197. https://doi.org/10.1016/J.ELECTACTA.2015.03.022.

(56) Kim, D. W.; Li, O. L.; Saito, N. Enhancement of ORR Catalytic Activity by Multiple Heteroatom-Doped Carbon Materials. *Physical Chemistry Chemical Physics* **2014**, *17* (1), 407–413. https://doi.org/10.1039/C4CP03868A.

(57) Xiang, Y.; Kong, L.; Xie, P.; Xu, T.; Wang, J.; Li, X. Carbon Nanotubes and Activated Carbons Supported Catalysts for Phenol in Situ Hydrogenation: Hydrophobic/Hydrophilic Effect. *Industrial and Engineering Chemistry Research* **2014**, *53* (6), 2197–2203. https://doi.org/10.1021/IE4035253.

(58) Lu, Z.; Chen, G.; Siahrostami, S.; Chen, Z.; Liu, K.; Xie, J.; Liao, L.; Wu, T.; Lin, D.; Liu, Y.; Jaramillo, T. F.; Nørskov, J. K.; Cui, Y. High-Efficiency Oxygen Reduction to Hydrogen Peroxide Catalysed by Oxidized Carbon Materials. *Nature Catalysis* **2018**, *1* (2), 156–162. https://doi.org/10.1038/s41929-017-0017-x.

(59) Chang, Q.; Zhang, P.; Mostaghimi, A. H. B.; Zhao, X.; Denny, S. R.; Lee, J. H.; Gao, H.; Zhang, Y.; Xin, H. L.; Siahrostami, S.; Chen, J. G.; Chen, Z. Promoting H2O2 Production via 2-Electron Oxygen Reduction by Coordinating Partially Oxidized Pd with Defect Carbon. *Nature Communications 2020 11:1* **2020**, *11* (1), 1–9. https://doi.org/10.1038/s41467-020-15843-3.

(60) Zhang, Q.; Tan, X.; Bedford, N. M.; Han, Z.; Thomsen, L.; Smith, S.; Amal, R.; Lu, X. Direct Insights into the Role of Epoxy Groups on Cobalt Sites for Acidic H2O2 Production. *Nature Communications 2020 11:1* **2020**, *11* (1), 1–11. https://doi.org/10.1038/s41467-020-17782-5.

(61) Li, X.; Zhang, B. W.; Yan, X.; Zhang, Y.; Deng, X.; Zhang, S. Fe,N-Doped Graphene Prepared by NH3 Plasma with a High Performance for Oxygen Reduction Reaction. *Catalysis Today* **2019**, *337*, 97–101. https://doi.org/10.1016/J.CATTOD.2019.04.032.

(62) Li, X.; Wang, H.; Robinson, J. T.; Sanchez, H.; Diankov, G.; Dai, H. Simultaneous Nitrogen Doping and Reduction of Graphene Oxide. *J Am Chem Soc* **2009**, *131* (43), 15939–15944.

(63) Lenarda, A.; Bevilacqua, M.; Tavagnacco, C.; Nasi, L.; Criado, A.; Vizza, F.; Melchionna, M.; Prato, M.; Fornasiero, P. Selective Electrocatalytic H 2 O 2 Generation by Cobalt@N-Doped Graphitic Carbon Core–Shell Nanohybrids. *ChemSusChem* **2019**, *12* (8), 1664–1672. https://doi.org/10.1002/cssc.201900238.

(64) Wan, K.; Long, G. F.; Liu, M. Y.; Du, L.; Liang, Z. X.; Tsiakaras, P. Nitrogen-Doped Ordered Mesoporous Carbon: Synthesis and Active Sites for Electrocatalysis of Oxygen Reduction Reaction. *Applied Catalysis B: Environmental* **2015**, *165*, 566–571. https://doi.org/10.1016/J.APCATB.2014.10.054.

(65) Rao, C. N. R.; Pramoda, K.; Kumar, R. Covalent Cross-Linking as a Strategy to Generate Novel Materials Based on Layered (2D) and Other Low D Structures. *Chemical Communications* **2017**, *53* (73), 10093–10107. https://doi.org/10.1039/C7CC05390H.

(66) Liu, Y.; Su, Y.; Quan, X.; Fan, X.; Chen, S.; Yu, H.; Zhao, H.; Zhang, Y.; Zhao, J. Facile Ammonia Synthesis from Electrocatalytic N2 Reduction under Ambient Conditions on N-Doped Porous Carbon. *ACS Catalysis* **2018**, *8* (2), 1186–1191. https://doi.org/10.1021/acscatal.7b02165.

(67) Yao, X.; Chen, Z. W.; Wang, Y. R.; Lang, X. Y.; Zhu, Y. F.; Gao, W.; Jiang, Q. High-Loading Intrinsic Active Sites for Ammonia Synthesis Using Efficient Single-Atom Catalyst: 2D Tungsten-Porphyrin Sheet. *Applied Surface Science* **2020**, *529*, 147183. https://doi.org/10.1016/J.APSUSC.2020.147183.

(68) Katsounaros, I.; Cherevko, S.; Zeradjanin, A. R.; Mayrhofer, K. J. J. Oxygen Electrochemistry as a Cornerstone for Sustainable Energy Conversion. *Angewandte Chemie International Edition* **2014**, *53* (1), 102–121. https://doi.org/10.1002/ANIE.201306588.

(69) Kim, J.; Choi, W.; Park, J. W.; Kim, C.; Kim, M.; Song, H. Branched Copper Oxide Nanoparticles Induce Highly Selective Ethylene Production by Electrochemical Carbon Dioxide Reduction. *J Am Chem Soc* **2019**, *141* (17), 6986–6994. https://doi.org/10.1021/JACS.9B00911.

(70) Chen, W. F.; Sasaki, K.; Ma, C.; Frenkel, A. I.; Marinkovic, N.; Muckerman, J. T.; Zhu, Y.; Adzic, R. R. Hydrogen-Evolution Catalysts Based on Non-Noble Metal Nickel–Molybdenum Nitride Nanosheets. *Angewandte Chemie International Edition* **2012**, *51* (25), 6131–6135. https://doi.org/10.1002/ANIE.201200699.

(71) Karunadasa, H. I.; Montalvo, E.; Sun, Y.; Majda, M.; Long, J. R.; Chang, C. J. A Molecular MoS2 Edge Site Mimic for Catalytic Hydrogen Generation. *Science (1979)* **2012**, *335* (6069), 698–702. https://doi.org/10.1126/SCIENCE.1215868.

(72) Laursen, A. B.; Patraju, K. R.; Whitaker, M. J.; Retuerto, M.; Sarkar, T.; Yao, N.; Ramanujachary, K. v.; Greenblatt, M.; Dismukes, G. C. Nanocrystalline Ni5P4: A Hydrogen Evolution Electrocatalyst of Exceptional Efficiency in Both Alkaline and Acidic Media. *Energy & Environmental Science* **2015**, *8* (3), 1027–1034. https://doi.org/10.1039/C4EE02940B.

(73) Shahrestani, S.; Beheshti, M.; Kakooei, S. Investigation of Electrochemical Parameters on Cost-Effective Zn/Ni-Based Electrocatalysts for Electrochemical CO2 Reduction Reaction to SYNGAS(H2+CO). *Journal of The Electrochemical Society* **2022**, *169* (4), 044519. https://doi.org/10.1149/1945-7111/AC645A.

(74) Choi, J. Y.; Yang, L.; Kishimoto, T.; Fu, X.; Ye, S.; Chen, Z.; Banham, D. Is the Rapid Initial Performance Loss of Fe/N/C Non Precious Metal Catalysts Due to Micropore Flooding? *Energy & Environmental Science* **2017**, *10* (1), 296–305. https://doi.org/10.1039/C6EE03005J.

(75) Ferrandon, M.; Wang, X.; Kropf, A. J.; Myers, D. J.; Wu, G.; Johnston, C. M.; Zelenay, P. Stability of Iron Species in Heat-Treated Polyaniline–Iron–Carbon Polymer Electrolyte Fuel Cell Cathode Catalysts. *Electrochimica Acta* **2013**, *110*, 282–291. https://doi.org/10.1016/J.ELECTACTA.2013.03.183.

(76) Shen, R.; Chen, W.; Peng, Q.; Lu, S.; Zheng, L.; Cao, X.; Wang, Y.; Zhu, W.; Zhang, J.; Zhuang, Z.; Chen, C.; Wang, D.; Li, Y. High-Concentration Single Atomic Pt Sites on Hollow CuSx for Selective O2 Reduction to H2O2 in Acid Solution. *Chem* **2019**, *5* (8), 2099–2110. https://doi.org/10.1016/J.CHEMPR.2019.04.024.

(77) Deng, D.; Chen, X.; Yu, L.; Wu, X.; Liu, Q.; Liu, Y.; Yang, H.; Tian, H.; Hu, Y.; Du, P.; Si, R.; Wang, J.; Cui, X.; Li, H.; Xiao, J.; Xu, T.; Deng, J.; Yang, F.; Duchesne, P. N.; Zhang, P.; Zhou, J.; Sun, L.; Li, J.; Pan, X.; Bao, X. A Single Iron Site Confined in a Graphene Matrix for the Catalytic Oxidation of Benzene at Room Temperature. *Science Advances* **2015**, *1* (11). https://doi.org/10.1126/SCIADV.1500462.

(78) Liu, P.; Zhao, Y.; Qin, R.; Mo, S.; Chen, G.; Gu, L.; Chevrier, D. M.; Zhang, P.; Guo, Q.; Zang, D.; Wu, B.; Fu, G.; Zheng, N. Photochemical Route for Synthesizing Atomically Dispersed Palladium Catalysts. *Science (1979)* **2016**, *352* (6287), 797–801. https://doi.org/10.1126/SCIENCE.AAF5251.

(79) Jones, J.; Xiong, H.; DeLaRiva, A. T.; Peterson, E. J.; Pham, H.; Challa, S. R.; Qi, G.; Oh, S.; Wiebenga, M. H.; Hernández, X. I. P.; Wang, Y.; Datye, A. K. Thermally Stable Single-Atom Platinum-on-Ceria Catalysts via Atom Trapping. *Science (1979)* **2016**, *353* (6295), 150–154. https://doi.org/10.1126/SCIENCE.AAF8800.

(80) Wang, L.; Zhang, W.; Wang, S.; Gao, Z.; Luo, Z.; Wang, X.; Zeng, R.; Li, A.; Li, H.; Wang, M.; Zheng, X.; Zhu, J.; Zhang, W.; Ma, C.; Si, R.; Zeng, J. Atomic-Level Insights in Optimizing Reaction Paths for Hydroformylation Reaction over Rh/CoO Single-Atom Catalyst. *Nature Communications 2016 7:1* **2016**, *7* (1), 1–8. https://doi.org/10.1038/ncomms14036.

(81) He, X.; Deng, Y.; Zhang, Y.; He, Q.; Xiao, D.; Peng, M.; Zhao, Y.; Zhang, H.; Luo, R.; Gan, T.; Ji, H.; Ma, D. Mechanochemical Kilogram-Scale Synthesis of Noble Metal Single-Atom Catalysts. *Cell Reports Physical Science* **2020**, *1* (1), 100004. https://doi.org/10.1016/J.XCRP.2019.100004.

(82) Li, X.; Xi, S.; Sun, L.; Dou, S.; Huang, Z.; Su, T.; Wang, X. Isolated FeN4 Sites for Efficient Electrocatalytic CO2 Reduction. *Advanced Science* **2020**, *7* (17), 2001545. https://doi.org/10.1002/ADVS.202001545.

(83) Chen, Z. W.; Chen, L. X.; Jiang, M.; Chen, D.; Wang, Z. L.; Yao, X.; Singh, C. V.; Jiang, Q. A Triple Atom Catalyst with Ultrahigh Loading Potential for Nitrogen Electrochemical Reduction. *Journal of Materials Chemistry A* **2020**, *8* (30), 15086–15093. https://doi.org/10.1039/D0TA04919K.

(84) Li, M.; Cui, Y.; Zhang, X.; Luo, Y.; Dai, Y.; Huang, Y. Screening a Suitable Mo Form Supported on Graphdiyne for Effectively Electrocatalytic N2 Reduction Reaction: From Atomic Catalyst to Cluster Catalyst. *The Journal of Physical Chemistry Letters* **2020**, *11* (19), 8128–8137. https://doi.org/10.1021/ACS.JPCLETT.0C02354.

(85) Chen, Z. W.; Yan, J.-M.; Jiang, Q. Single or Double: Which Is the Altar of Atomic Catalysts for Nitrogen Reduction Reaction? *Small Methods* **2019**, *3* (6), 1800291. https://doi.org/10.1002/SMTD.201800291.

(86) Zheng, G.; Li, L.; Hao, S.; Zhang, X.; Tian, Z.; Chen, L. Double Atom Catalysts: Heteronuclear Transition Metal Dimer Anchored on Nitrogen-Doped Graphene as Superior Electrocatalyst for Nitrogen Reduction Reaction. *Advanced Theory and Simulations* **2020**, *3* (12), 2000190. https://doi.org/10.1002/ADTS.202000190.

(87) Qian, Y.; Liu, Y.; Zhao, Y.; Zhang, X.; Yu, G. Single vs Double Atom Catalyst for N2 Activation in Nitrogen Reduction Reaction: A DFT Perspective. *EcoMat* **2020**, *2* (1), e12014. https://doi.org/10.1002/EOM2.12014.

(88) Yang, W.; Huang, H.; Ding, X.; Ding, Z.; Wu, C.; Gates, I. D.; Gao, Z. Theoretical Study on Double-Atom Catalysts Supported with Graphene for Electroreduction of Nitrogen into Ammonia. *Electrochimica Acta* **2020**, *335*, 135667. https://doi.org/10.1016/J.ELECTACTA.2020.135667.

(89) Lv, X.; Wei, W.; Huang, B.; Dai, Y.; Frauenheim, T. High-Throughput Screening of Synergistic Transition Metal Dual-Atom Catalysts for Efficient Nitrogen Fixation. *Nano Letters* **2021**, *21* (4), 1871–1878. https://doi.org/10.1021/ACS.NANOLETT.0C05080.

(90) Chen, Z.; Zhao, J.; Cabrera, C. R.; Chen, Z. Computational Screening of Efficient Single-Atom Catalysts Based on Graphitic Carbon Nitride (g-C3N4) for Nitrogen Electroreduction. *Small Methods* **2019**, *3* (6), 1800368. https://doi.org/10.1002/SMTD.201800368.

(91) Yongkang Xu; Zhewei Cai; Pan Du; Jiaxing Zhou; Yonghui Pan; Ping Wu; Chenxin Cai. Taming the Challenges of Activity and Selectivity in the Electrochemical Nitrogen Reduction Reaction Using Graphdiyne-Supported Double-Atom Catalysts. *Journal of Materials Chemistry A* **2021**, *9* (13), 8489–8500. https://doi.org/10.1039/D1TA00262G.

(92) Ma, D.; Zeng, Z.; Liu, L.; Huang, X.; Jia, Y. Computational Evaluation of Electrocatalytic Nitrogen Reduction on TM Single-, Double-, and Triple-Atom Catalysts (TM = Mn, Fe, Co, Ni) Based on Graphdiyne Monolayers. *The Journal of Physical Chemistry C* **2019**, *123* (31), 19066–19076. https://doi.org/10.1021/ACS.JPCC.9B05250.

(93) Bai, L.; Hsu, C.-S.; Alexander, D. T. L.; Chen, H. M.; Hu, X. A Cobalt–Iron Double-Atom Catalyst for the Oxygen Evolution Reaction. *J Am Chem Soc* **2019**, *141* (36), 14190–14199. https://doi.org/10.1021/JACS.9B05268.

(94) Yan, Y.; Cheng, H.; Qu, Z.; Yu, R.; Liu, F.; Ma, Q.; Zhao, S.; Hu, H.; Cheng, Y.; Yang, C.; Li, Z.; Wang, X.; Hao, S.; Chen, Y.; Liu, M. Recent Progress on the Synthesis and Oxygen Reduction Applications of Fe-Based Single-Atom and Double-Atom Catalysts. *Journal of Materials Chemistry A* **2021**, *9* (35), 19489–19507. https://doi.org/10.1039/D1TA02769G.

(95) Chen, H.; Zhang, Y.; He, Q.; Zhang, H.; Xu, S.; He, X.; Ji, H. A Facile Route to Fabricate Double Atom Catalysts with Controllable Atomic Spacing for the R-WGS Reaction. *Journal of Materials Chemistry A* **2020**, *8* (5), 2364–2368. https://doi.org/10.1039/C9TA13192B.

2. Methods and Apparatus

2.1 Electrochemical methods and Apparatus

Theoretical Base.[1] On a first level, electrochemical techniques can be divided in Direct Current (DC) techniques and Alternating Current (AC) techniques. Cyclic Voltammetries (CVs), Linear Sweep Voltammetries (LSVs), ChronoAmperometries (CAs) and ChronoPotentiometries (CPs) are the most used DC techniques nowadays, while Electrochemical Impedance Spectroscopy (EIS) represents the most used AC application in electrochemical characterizations. To explain electrodic (faradaic) processes, a parallel to chemical redox reactions can be made. During a standard redox reaction, an electron transfer (ET) takes place between the Highest Occupied Molecular Orbital (HOMO) of the reducing agent and the Lowest Unoccupied Molecular Orbital (LUMO) of the reduced molecule. The energy difference of the HOMO-LUMO levels is the driving force for the reaction. The power of electrochemistry stems from the ability to control the energy of an electron on the electrode surface by applying a bias (with a $\Delta G = nFE$). In an electrochemical reduction, once the potential energy is higher then the LUMO, the electron transfer from electrode to molecule can take place (Fig. 2.1).[2] Moreover, the applied potential is a known parameter (managed by the operator through the potentiostat), and can be exploited for calculation of thermodynamic (e.g. E^0, ΔG) and kinetic (e.g. k_0, i_0) parameters.

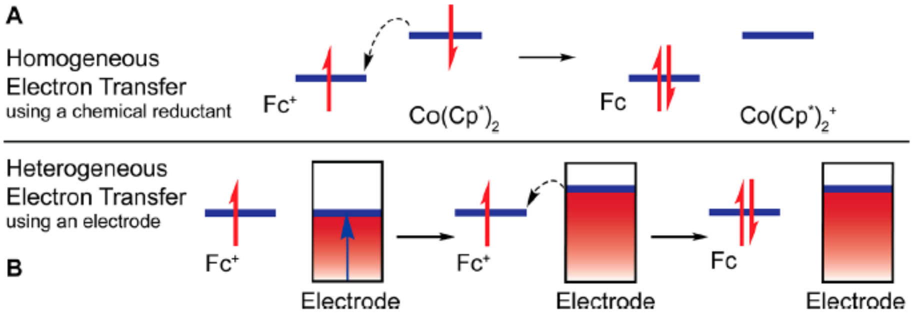

Figure 2.1 Difference between a chemical redox reaction and a heterogeneous electron transfer. Reprinted with permission from ref. [2] with permission. © Copyright 2017 ACS

Cyclic Voltammetry is a potential sweep technique, meaning that during operation the potential of the working electrode scans a predetermined window going from one potential figure to a second and then reversed (in Fig. 2.2a, $V_1 \rightarrow V_2 \rightarrow V_1$) in a triangular pulse. To understand the resulting current-potential profile, some consideration on the local electrode-electrolyte interface must be done.

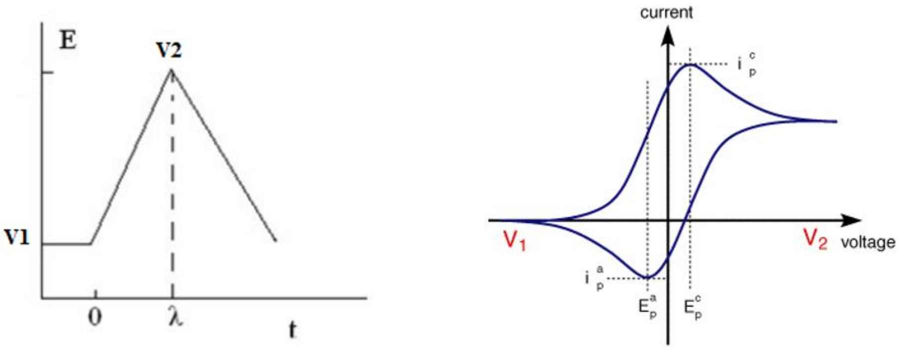

Figure 2.2 The time-potential profile of a CV (a), and a possible recorded signal in a current-potential plot (b).

During the first part of the CV (the anodic sweep), the potential changes at a fixed rate from V_1 to V_2. If a peak in the voltammogram (Fig. 2.2b) is registered, an oxidation is taking place. The height of the peak is proportional to the quantity of reactant, but also scan rate and the diffusional properties of the electroactive species. The Randles-Sevcik equation describes the relation between the peak current and the electrochemical characteristics of the setup for the reaction of a freely diffusing analyte in solution:

$$i_p = 0.4463\, n\, FAC\, (\frac{nFvD}{RT})^{\frac{1}{2}}$$

Where:

i_p is the current maximum

n is the number of electrons transferred

A the electrode surface area

F is the Faraday Constant

D is the diffusion coefficient

C is the concentration of the reactant

v is the scan rate

R is the Gas constant

T is the temperature

The “duck shape” of the CV is due to the diffusion of the reacting species to the electrode from the bulk. Indeed, the peak current potential (E_p) is the potential at which the rate of reaction at the electrode-electrolyte interface is equal to the rate of diffusion of the reactant from the bulk of the solution to the interface. At higher potentials the reaction is limited by the diffusion to the electrode and the current shrinks due to depletion of the diffusion layer. The same considerations can be done for the second part of the CV (the cathodic sweep), where a reduction can take place. The analysis of position, shape and integral of these peaks is fundamental to the correct attribution of electrochemical signals to the right process. As an example, the Randles-Sevcik equation states that the peak current and the square root of the scan rate are in a linear relationship. However, if the reactant is adsorbed on the electrode surface, then the peak current is not dependent on the analyte concentration (and the diffusion coefficient) but to the surface coverage (Γ) through the following relation:

$$i_p = \frac{n^2F^2}{4RT}\, \nu\, A\, \Gamma$$

In this equation the linear relation is between i_p and v. Therefore, a series of CVs at different scan rates can be exploited to plot v/i_p and deduce if the analyte is freely diffusing or not.

Similarly to CVs, LSVs are potential sweep techniques that use a single potential sweep (either anodic or cathodic, Fig. 2.3). They have been used throughout this dissertation to evaluate catalytic activity, where a reverse scan is not necessary.

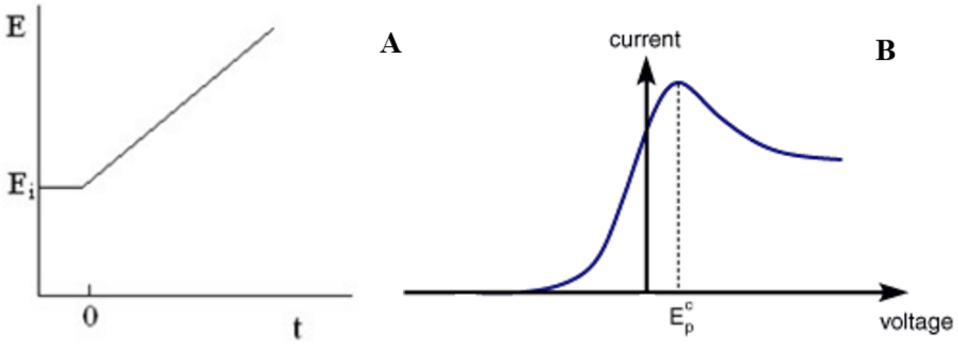

Figure 2.3 Time-potential profile for a LSV (a) and potential-current related plot (b).

Chrono-dependent methods (CA and CP) involve the measurement over time of either current (CA) or potential (CP) while the other parameter is kept at a fixed value (Fig. 2.4). The stepped potential waveform in CA (Fig. 2.4a left) results in a *i-t* curve that decays exponentially, following Cottrell equation:

$$i(t) = \frac{nFAD^{1/2}\, C^*}{(\pi\, t)^{1/2}}$$

Where C^* is the bulk concentration of the analyte. The CA shape is once again influenced by mass transport of the analyte to the electrode surface, as attested by the diffusion coefficient. Indeed, as the analyte reacts at the electrode interface, its local concentration is depleted and the current will dacay over time until either the analyte is completely consumed ($i = 0$) or an equilibrium with diffusion is reached ($i = i_{eq}$). CP functions in much the same way with a stepped current wavefunction and plotting time vs the registered potential. The *E-t* plot will tend toward higher values of E to keep the current from deviating from the setpoint. The increase in bias will counteract the slower kinetics due to depleted reactant, until consumption of the analyte itself. At this point it is important to point out that every technique until now has been discussed with examples of reversible systems (R/O couples with very fast kinetics). In the case of heterogeneous electrocatalysis, the subject of this dissertation, the behaviour will deviate for obvious reasons. For example, in the case of copper oxide nanoparticles (Chapter 5), electrode kinetics (and thus *E-t* plots) can change during analysis, due to chemical modification of the electrodic surface, leading to a trend inversion (a lowering of the registered bias in time as opposed to the standard behaviour).

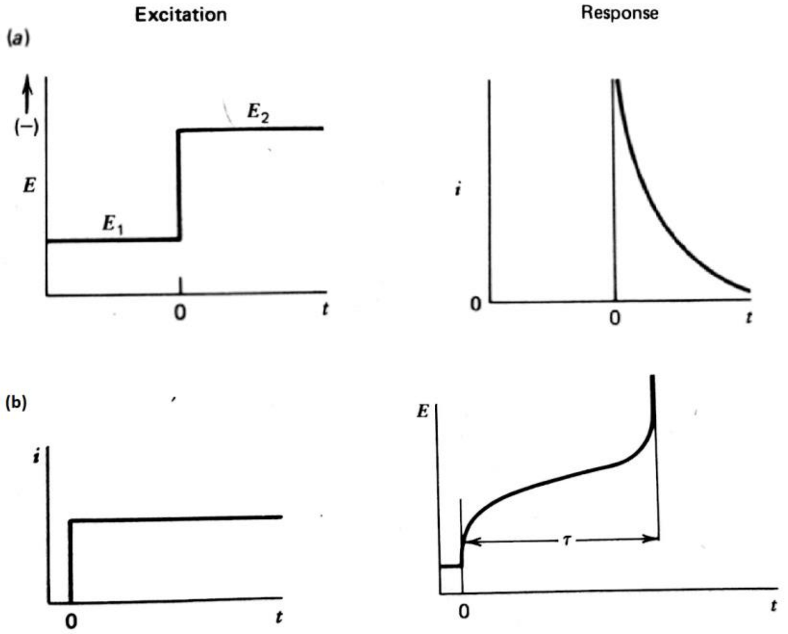

Figure 2.4 Excitation and Response waves for CAs (a) and CPs (b).

Finally, Electrochemical Impedance Spectroscopy (EIS) provides information about the resistive, capacitive and inductive properties of a system. As previously noted, EIS uses an AC sinusoidal excitation signal as a probe collecting the impedance value at varying AC frequencies. Impedance in itself, is defined as the combined effects of the resistance and reactance in a system. At its most fundamental level, an electrochemical cell can be studied with an equivalent circuit, in which every component (i.e. resistors, capacitors and inductors) corresponds to phenomena in the cell. In order to understand the application of EIS to electrochemical system, it is instrumental to first explore equivalent circuits and their response to EIS stimuli.

Considering first a pure resistance R across which a sinusoidal voltage is applied. The current can be calculated trough Omh’s law ($i = V/R$) and its onset is instantaneous, leading to a sinusoidal current wavefunction in phase with the bias. However, if we consider a capacitor in the same situation, the potential and current wavefunctions will be out of phase. Indeed, when the capacitor starts charging the current is maximized, while when the potential is at its peak, the capacitor is fully charged and no current passes (the capacitor acts as a brake). This difference in phases can be expressed more easily with complex notation, as the real and imaginary parts can facilitate calculations. In electrochemistry inductor-like behaviours are less frequent and will not be discussed in this thesis.

The simplest model for a cell, the Randles circuit, presents a resistor coupled with a capacitor and a resistor in parallel and the corresponding EIS gives a semicircle in a Nyquist plot (real impedance values vs imaginary impedance values).

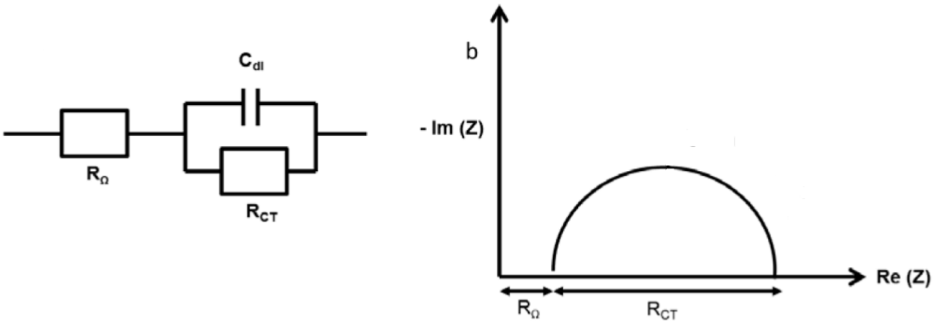

Figure 2.5 Randles equivalent circuit for a chemical cell and relative Nyquist plot

To understand the connection between Randles circuit and an electrochemical cell, we can evaluate each component at a time. The first resistance (R_{Ω}) and the capacitance (C_{dl}) depend on the nature of the electrode-electrolyte interface. R_{Ω}, also called uncompensated resistance (R_u), is the resistance of the electrolyte between the working electrode and the reference electrode (Fig. 2.6). The C_{dl} capacitance is instead caused by the accumulation of ions in solution on the electrode surface when a bias is imposed. C_{dl} is mainly dependent on the electrode and can be used to calculate the electrochemical surface area (ECSA) of different catalytic materials.

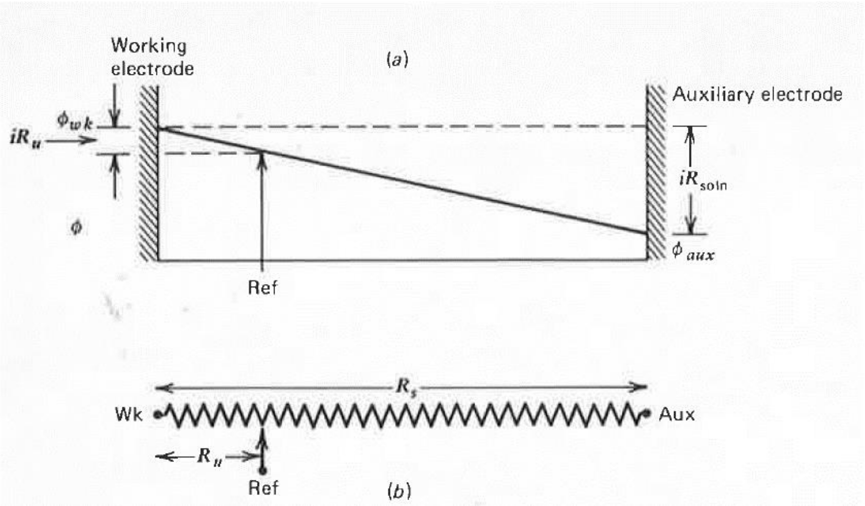

Figure 2.6 Potential difference between working and counter electrode in solution with calculated ohmic drop from uncompensated resistance (R_u or R_Ω) between working and reference electrode (a). The system can be also studied through the equivalent resistors (b).

R_{ct} has a more nuanced meaning. This resistance (the charge transfer resistance) can be derived from the Butler-Volmer equation:

$$R_{ct} = \frac{RT}{nFi_0}$$

From this relation, it can be seen that R_{ct} and i_0 (exchange current, and thus the heterogeneous electron transfer rate constant, k_0) are inversely proportional: this means that faster ET kinetics, have lower charge transfer resistance values. As previously noted, a normal Randles circuit will give a semicircle-shaped response in the R(Z) vs -Im(Z) space (i.e. Nyquist plot). In reality, the nature of heterogeneous electrodic reactions changes this shape in varying degrees. Two differences are particularly important to properly fit an EIS Nyquist plot. First, the semicircle can appear depressed (not perfectly spherical). This deviation from the model is due to the roughness of the electrode surface.[3] To fit properly this shape, a Constant Phase Element (CPE) can be used. The admittance (Y, the inverse of the impendace) of a CPE is:

$$Y_{CPE} = Q_0(wi)^n$$

With $0 < n < 1$. When $n = 1$ the CPE behaves as a pure capacitor, while for $n = 0$ the CPE behaves as a pure resistor. Usually, values of n near 0.8 are assumed for electrode surfaces, resulting in a slightly depressed semicircle. A second correction is at the end of the semicircle (low frequencies), where diffusion limitations can give rise to a linear response in the Nyquist plot. To fit this data, a Warburg element can be used to model semi-infinite linear diffusion, in other words unrestricted diffusion to a large planar electrode. The presence of the Warburg element can be recognised from a straight line with a 45° slope. However, in this dissertation, EIS data has been collected mostly to assess R_Ω values and to check that the electrochemical setup was working properly before every measurement.

Electrochemical setup. All electrochemical characterizations were carried out at room temperature on an Autolab 302N electrochemical workstation (Metrohm, Autolab) by using a standard three-electrode setup. Saturated Calomel Electrode (SCE) was used as reference electrode, while Pt wire was used as counter electrode. As working electrode, several supports were used throughout this thesis: Rotating Disk Electrode (RDE, Metrohm) and Rotating Ring Disk Electrode (RRDE, Metrohm) present both a circular Glassy Carbon (GC) surface, with the addition in RRDE of a platinum ring; moreover, Carbon Paper from Toray® and Sigracet® (39BB) were also used.

All measured potentials for CVs and LSVs were manually corrected for ohmic losses estimated through EIS and converted to reversible hydrogen electrode (RHE), while linear sweep voltammetries (LSVs) registered under Ar atmosphere were used to correct for background current under operation conditions. Electrochemical active surface area (ECSA) and Roughness factor (RF) values were calculated via the capacitive current near OCP at different scan speeds and using a reference specific capacitance (C_S) from papers on similar materials.

$$i_c = C_{DL}\, v_{scan}$$

$$ECSA = \frac{C_{DL}}{C_S}$$

$$RF = \frac{ECSA}{SA_{geom}}$$

Electrochemical impedance spectroscopy (EIS) measurements were performed using a frequency response analyzer (FRA, AutoLab 302 N, Metrohm) at room temperature. EIS spectra were recorded at OCP under pure Ar atmosphere with a 10 mV amplitude voltage perturbation in the maximum frequency range from 100 kHz to 1 Hz. The uncompensated resistance was estimated through fitting of the obtain spectra with a Randles circuit.[4]

To analyze H_2O_2 production, LSV measurements on the RRDE setup were performed. The widely used Koutechy–Levich (KL) method was not deemed suitable to determine the electron transfer number as showed in literature.[5] The collection efficiency (N_c) of the RRDE tip was evaluated for every material and rotation speed tested, showing fluctuation between the manufacturer value (25%) and 19% due to the roughness of carbon nanocomposite thin films.The disk electrode was scanned at a rate of 5 mV s^{-1} and the ring electrode potential in the RRDE system was set to 1.4 V vs RHE. The hydrogen peroxide selectivity (%H_2O_2) and the electron transfer number (n) were calculated by the followed equations:

$$n = \frac{4\, i_d}{i_r N + i_d}$$

$$\%_{H_2O_2} = \frac{4-n}{2} * 100$$

where i_d and i_r are the disk and ring currents, respectively. N is the collection efficiency, which was evaluated by the reduction of 10 mM $K_3[Fe(CN)_6]$ in 0.1 M KOH for every material and rotation speed tested, as reported by Zhou R. *et al*.[5]

For simple electrochemical characterizations (LSVs, CVs and R(R)DE measurements) a single compartment cell was used (Fig. 2.7), equipped with a bridge with a Vycor® frit to separate the catholyte (electrolyte in contact with the cathode) from the anolyte (electrolyte in contact with the anode). The reference electrode was connected through the electrolyte of the working electrode with a Luggin capillary.

Figure 2.7 Single cell setup housing RRDE GC/Pt tip (center), SCE electrode in a Luggin capillary (left) and a Pt counter electrode in a bridge equipped with a Vycor frit.

ChronoAmperometry (CA) or ChronoPotentiometry (CP) were used to assess faradaic efficiency both for ORR (coupled with RRDE measurements) and CO_2RR. ORR CA measurements were done in a two compartments cell in a vertical configuration (Fig. 2.8). In the top compartment, the working electrode (on carbon paper support) and the reference electrode in a vycor fritted bridge were placed. In the bottom compartment a Pt wire worked as a the counter electrode. At the center, as a separator, a Nafion 117 membrane was used. At the end of the measurements, the catholyte was collected with a syringe from one of the necks at the top of the cell.

Figure 2.8 Two compartments cell with working and reference electrode on the top and counter electrode at the bottom compartment. The two were separated by a Nafion 117 membrane.

Finally, CO_2RR tests were done in a two compartments cell in a H-cell configuration (Fig. 2.9). The working electrode consisted on a CP electrode pinched in place with a graphite rod, the reference was an Ag/AgCl electrode in a luggin capillary and a graphite counter electrode was separated from the main chamber with a Sustainion® X37-50 Grade RT membrane. Reagent mixing was controlled with Mass Flow Controllers (MFC, Brooks Instruments) capable of ranging the gas flow between 2 and 90 mL min^{-1}. A system of valves allowed for the selection of different gasses (N_2, CO_2, SO_2) to mix before the cell inlet. When the gas was fed to the cell, it passed through the catholyte, sparging it from previously solubilized gasses. The cathode compartment was connected with an online gas chromatographer (SRI 8610C configuration #5, Fig. 2.10) equipped with three detectors (TCD, FID-methanizer, FID-FPD for sulfur compounds) and two columns (Molesieve 5A) and Hayesep-D). Finally, the gas was vented in a KOH solution to neutralize any acidic gasses. A schematic representation of the entire setup is reported in Fig. 2.11.

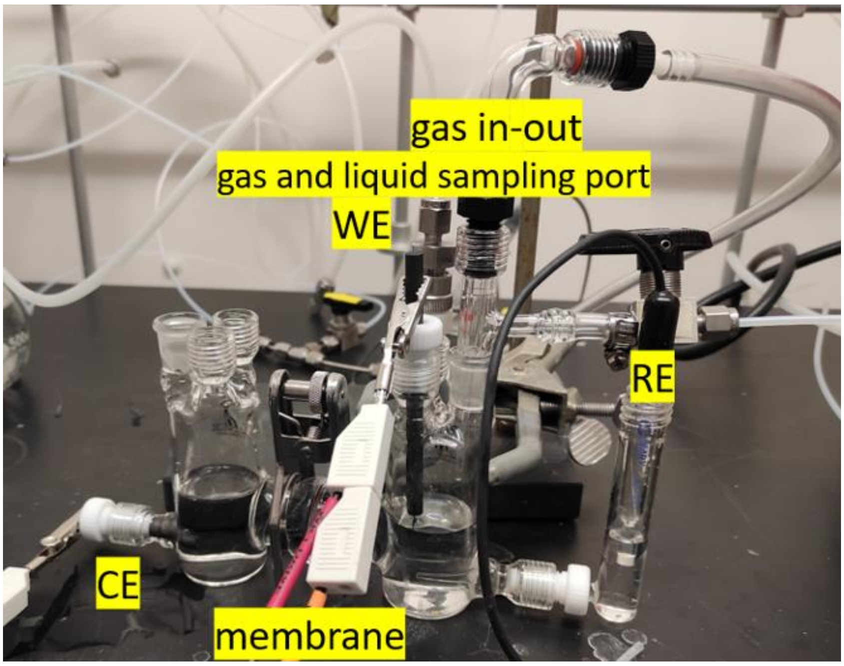

Figure 2.9 H-Cell with graphite counter electrode on the left side, Sustainion membrane separator, graphite rod current collector (and CP electrode dipped in the electrolyte) and Ag/AgCl in the Luggin capillary on the right.

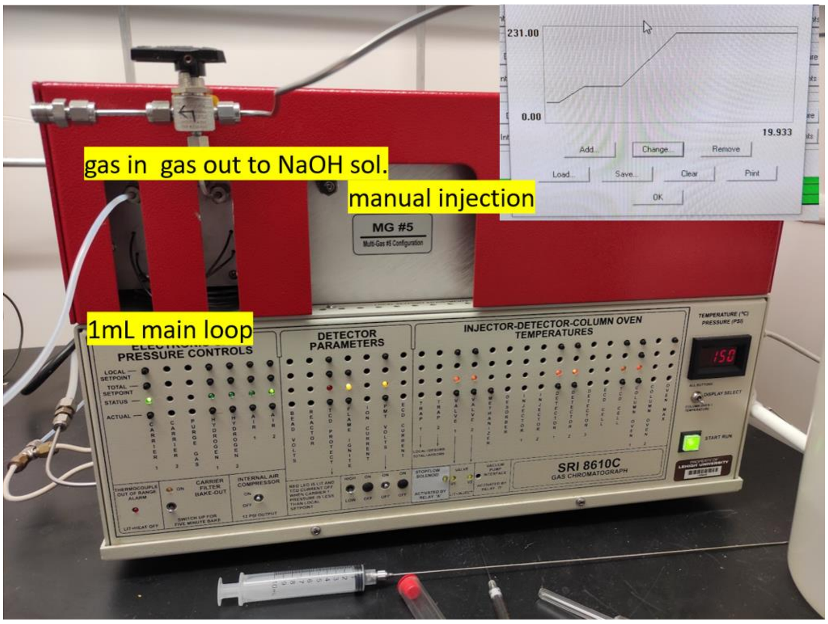

Figure 2.10 SRI GC 8610C configuration #5 with temperature gradient for the columns (inset)

GC sampling was done every 30 minutes to assess the composition of the gas mixture, while liquid sampling was done with a gas-tight syringe and analyzed with an Ionic Chromatographer (ECO IC, Metrohm).

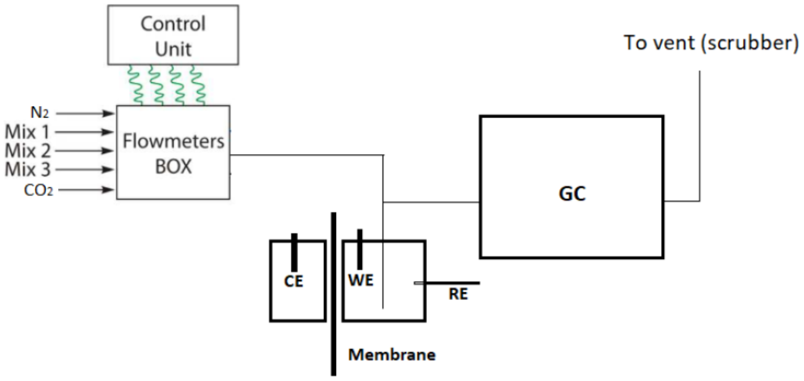

Figure 2.11 Schematics for the CO_2RR quantitative measurements with the H-cell setup

Faradaic Efficiencies Determination. Faradaic Efficiency (FE) was calculated from the concentration of the products. The following formula is valid for any product either in solution or in the gas phase:

$$FE\ (\%) = \frac{n_e\ *\ n_P\ (mol) * F}{|Q(C)|} * 100$$

Where:

- n_e is the number of electrons exchanged for the particular reaction
- n_P is the moles of product
- F is the Faraday constant (96 485 C mol^{-1})
- Q is the charge obtained from integration of the CA (as an absolute value)

Ink formulation. All the inks, unless otherwise stated, were prepared in a 3:1 H_2O-iPrOH mixture at 5 mg mL^{-1} concentration with the addition of 5% (v/v) binder solution. The preferred binder was Nafion® 117 for all experiments in single compartment cell and double compartment utilizing Nafion® 117 membrane and Sustainion® XC-2 for Sustainion® membranes. The ink is sonicated for 30 minutes in iced water and then drop casted on the chosen electrode, either GC disks with

0.198 cm^2 surface area or CP until a specified loading is reached. The electrode was dried under reduced pressure for 1h before use.

2.2 Analitical Methods

Permanganometric Titrations (for H_2O_2). Permanganometric titrations were carried out with a 0.01N solution of $KMnO_4$.[6] The concentration of the permanganate solution was standardized through the primary standard sodium oxalate. Bulk electrolysis tests were conducted in 0.1M H_2SO_4 for a set amount of time in a two compartments cell, then the catholyte was collected and acidified with 5mL of 4M H_2SO_4, and the titration started. Each test was repeated three times for comparison

Spectroscopic Measurements (for NH_3). Ammonia concentration in solution was evaluated through a modification of the standard method for wastewater analysis with sodium salicylate.[7] Briefly, three solutions were prepared (A, B, C): a 5% solution of salicylic acid and in 1M NaOH (A), a 1% solution of the sodium nitroprusside catalyst (B) and a 7% solution of sodium dichloroisocyanurate dihydrate (C). To 1mL of reaction solution, 125 µL of Sol. A, 40 µL of Sol. B, and 15 µL of Sol. C were added one at a time with stirring and the resulting mixture was kept away from light for 1 h. The absorbance value at 660 nm was registered and compared to a calibration curve. The calibration curve (Fig. 2.12) was obtained averaging four different curves with NH_4Cl standards in KOH 0.1M solution after background correction with a blank developed solution (with no ammonium added).

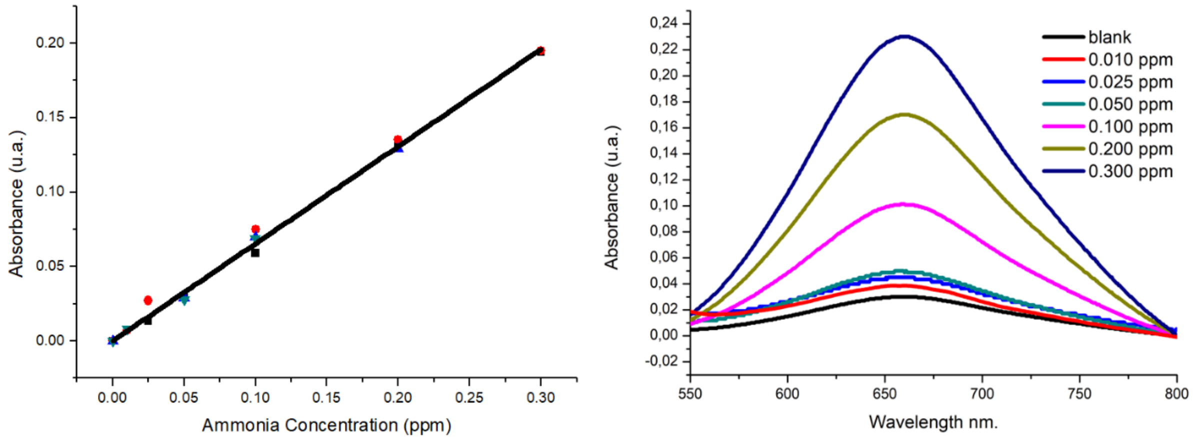

Figure 2.12 Calibration curve (left) correlating NH_3 concentration with the absorbance peak at 660 nm (right). Indophenol method.

A second colorimetric test based on Nessler reaction was adopted to further confirm NH_3 production data (FEs and formation rates). To 1 mL of electrolyte, 50 µL of Nessler solution was added and the color was left to develop for 15 minutes. The absorbance value at 420 nm was registered and compared to a calibration curve. The calibration curve was obtained averaging four different curves with NH_4Cl standard solutions in KOH 0.1M.

Cleaning protocol. The cleaning of the entire NRR setup is of outmost importance to get relevant data from this technique. If the material has nitrogen containing precursors (e.g. nitrates or ammonium salts), the first step must be a thorough washing of the material itself. In our case, the ZIF-derived porous carbon was washed in a 0.1M HCl solution several times with sonication followed by separation through centrifugation. After ink preparation, the deposition (for all materials) on the GC-RRDE should be limited to low/midrange loadings (<400 µg cm^{-2}). This is extremely important for hydrophobic materials, as thick films in water-based electrolytes tend to form bubbles that negate the cleaning action of the electrolyte. After assembling of the entire setup (cell, bridges, electrodes and gas inlet), the glass cell was filled with milliQ water, and everything was kept soaking. After 20 minutes, the water is drained with a syringe and the process repeated for at least 6 times. Finally, the cell was filled with the desired amount of electrolyte. The solution was purged with Ar pure gas for 30 minutes and a CV on the Pt ring electrode was used to evaluate the cleanliness of the setup. Only when no NH_3 peak is detected, then the electrochemical characterizations can proceed.

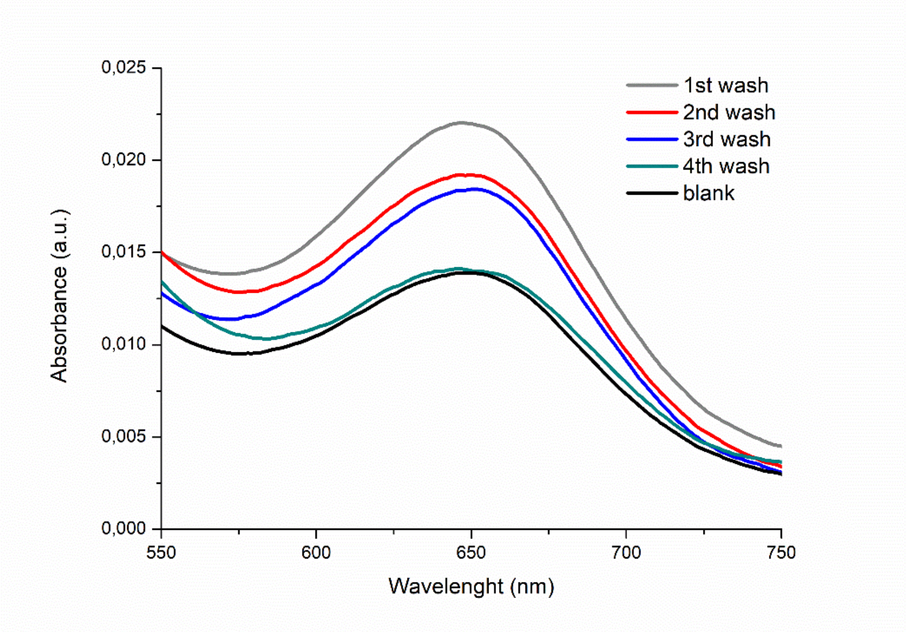

Figure 2.13 Trend observed for NH_3 traces throughout consecutive washings of the entire cell setup, including the RRDE-supported electrocatalyst. Case of study: ZIF-1100-1h. The 1st step was referred to the cell setup including the ZIF-1100-1h deposited on RRDE, after the preliminary powder washing treatment before ink preparation.

Other characterizations. Raman spectra were recorded on a inVia Renishaw spectrometer equipped with a Nd:YAG laser using an excitation wavelength of 532 nm. IR spectra were recorded in attenuated total reflectance (ATR) mode on a Shimadzu IRAffinity-1S spectrophotometer equipped with a QATR 10 accessory. Thermogravimetric analysis (TGA) was carried out on a TA Q50 instrument with a heating rate of 20 °C min^{-1} under flowing dry air. TEM analyses were performed using a Philips EM 208 microscope operating at 100 kV and equipped with an 11 MP bottom-mounted CCD Olympus Quemesa camera. Textural properties were analyzed by N_2 physisorption at the liquid nitrogen temperature using a Micrometrics ASAP 2020 automatic analyzer. All the NPs were degassed at 50 °C for 12 h at 10 μmHg. The specific surface area was obtained by applying the Brunauer–Emmett–Teller (BET) method equation. Pore size distribution was determined applying the Barrett, Joyner, and Halenda (BJH) method equation to the desorption branch of the isotherms. H_2 chemisorption was performed using a Micrometrics ASAP 2020C apparatus. A chemisorption stoichiometry H:M = 1:1 was assumed for the calculation of the exposed metal surface area. The materials have been degassed at 100 °C for 6 h. H_2 chemisorption isotherms have been recorded in a 1–400 Torr pressure range at room temperature. The elemental concentrations in the catalysts were quantified by means of inductively coupled plasma-optical emission spectrometry (ICP-OES) using an Optima 8000 instrument (Perkin Elmer; Waltham, MA, USA) with an integrated S10 autosampler. A five-point standard curve was used for ICP-OES measurements (range: 0–10 mg L–1). The limit of detection at an operative wavelength of 228.616 nm was 0.01 mg L^{-1}. Powder X-ray diffraction (XRD) analysis was performed on an X’Pert Philips MPD with monochromatic Cu Kα radiation ($\lambda = 1.5406$ Å), and the range used was $2\theta = 10$–120° in Bragg–Brentano geometry with a step size of 0.0263°. The average crystallite size was determined applying the Scherrer equation $D = (k \times \lambda)/(\beta\cos\theta)$ where D is the mean size of the crystallite, the Scherrer constant $k = 0.9354$ was obtained by tabulated values for the octahedral crystallites determined for hkl = 111, λ is the X-ray wavelength expressed in Å, β is the full width at half maximum of the first XRD peak expressed in radians, and θ is the Bragg angle. The X-ray photoelectron spectroscopy (XPS) was performed on a SPECS Sage HR 100 spectrometer with a nonmonochromatic X ray source of Magnesium with a Kα line of 1253.6 eV energy and 250 W.

2.3 N_2 Physisorption

The catalytic activity of a solid material is strictly related to the morphology and the extension of its surface. The dimension and the texture of pores also play a crucial role since they can have a strong influence on the reaction selectivity. The common method used to determine the textural characteristics of a solid material is based on the physisorption of a gas (usually N_2) because of the following advantages: i) low adsorption heat, related to the weak interactions for adsorption processes (ion dipole, dipole dipole, quadruple interactions); ii) possibility to have long range (i.e. multilayered) adsorption, leading to pore volume estimation; iii) physisorption is a fast process, except when in small pores, due to diffusion limitations; iv) total surface area can be estimated because adsorption is possible on any site and it is not dependent on specific sites energetics.

Brunauer, Emmet and Teller have developed a method (commonly regarded as BET) which allows the experimental determination of the number of adsorbate molecules needed for the formation of the theoretical monolayer. If the area effectively occupied by a single adsorbed molecule is known, it is possible to determine the total surface area. BET model starts from the assumption that adsorption process is an equilibrium with the formation of a series of layers, where the most external one is formed by adsorbate molecule directly in contact with the vapor phase. The surface area can be determined by directly applying the BET equation:

$$\frac{p}{n(p^0 - p)} = \frac{1}{n_m C} + \frac{C - 1}{n_m C} \cdot \frac{p}{p^0}$$

Where:

p is the has pressure

p^0 is the gas saturation pressure

n is the adsorbed gas at pressure p in grams

n_m is the adsorbed gas corresponding to the monolayer formation in grams

C is the BET constant (dependent on the interaction type between adsorbent and adsorbate).

This relation is usually linear in the range p/p^0 between 0.05 and 0.30. From the slope and the intercept n_m and C can be estimated. Then, the surface area can be calculated as:

$$SA_{BET} = \frac{n_m a_m N_A}{M_W}$$

Where:

a_m is the area occupied by an adsorbate molecule (for N_2 at -196 °C, $a_m = 0.162\ nm^2$)

N_A is the Avogadro’s constant

M_W is the adsorbate molecular weight

Most materials with high surface areas show porous structure. Is it useful to distinguish the internal surface area, due to porosity, from the external. It is also important to note that different adsorbate molecules will have different accessibility to pores, depending on shape and dimensions of the molecule itself. In general, pores can be divided in micropores (diameters less than 2nm), mesopores (range 2 – 50 nm) and macropores (more than 50 nm). The porosity of a material will affect greatly the shape of a physisorption isotherm. The most common isotherms (Fig. 2.14) have been classified into six shapes:

Type I isotherms are given by microporous solids having small external surfaces, where most of the contribution is due to the internal pore structure

Type II isotherms are typical of macroporous systems with continuous adsorption of species. The inflection point (denoted as 'B') denotes the pressure at which a monolayer is reached on the surface of the material.

Type III isotherms show no B inversion point and are uncommon; they point to a weak adsorbent-adsorbate interaction and, thus, indicate the necessity to use a different molecule in the analysis to get better characterize the material surface.

Type IV isotherms present a hysteresis loop (there is no perfect reversibility between adsorption and desorption), while behaving similarly to type II, and the limited adsorption at high p/p^0. The hysteresis is due to capillary condensation and denotes the presence of mesopores in the material.

Type V isotherms too show a hysteresis loop, while behaving similarly to type III, due to limited adsorbent-adsorbate interaction.

Type VI isotherms are given by stepwise multilayer adsorption on a non-porous surface. Each step in the isotherm represents the monolayer capacity for each adsorbed layer.

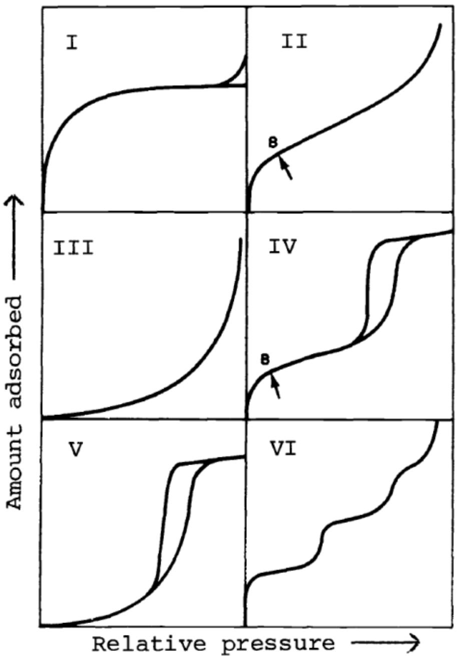

Figure 2.14 Type of adsorption/desorption isotherms. Reprinted with permission from ref. [8]

To analyze the mesopore structure of Type III and IV materials, the method commonly used was developed by Barret, Joyner and Halenda (BJH method). It describes the adsorption and capillary condensation inside mesopores. In particular, the capillary condensation in cylindrical pores is described by the Kelvin equation:

$$ln\frac{p}{p^0} = -\frac{2\gamma V_m}{RTr_c}$$

Where:

p is the pressure of the gas

p^0 is the gas saturation pressure

γ is the surface tension of the liquid

V_m is the liquid molar volume

R is the gas constant

T is the absolute temperature

r_c is the pore radius where capillary condensation occurs.

2.4 Transmission Electron Microscopy (TEM)

Of the many characterization techniques used in catalysis, TEM represents one of the most versatile: advanced electron microscopy not only gives morphological information on nanometer-scale objects, but by itself and coupled with different techniques, it can also give information on crystallography (from electron scattering),[9] chemical composition (i.e. through energy dispersive spectroscopy)[10] and analysis of dynamic systems (i.e. *in operando* TEM).[11] The versatility of TEM is complemented by the ease of sample preparation for inorganic, atmosphere-stable, materials. The need for electron microscopy arose from the limitation of visible light optics. The Rayleigh criterion is used to calculate the maximum theoretical resolution (R) of a microscope:

$$R = 0.61\frac{\lambda}{NA}$$

Where:

λ is the wavelength of the observed radiation

NA is the numerical aperture of the lens system (usually ~1)

From the Rayleigh criterion it can be calculated that using blue light (~ 400 nm) the resolution of a microscope would be near 200 nm, not allowing for detection of nanometric (< 100 nm) features. Using the De Broglie relation ($\lambda = h/p$), the wavelength of an electron can be calculated if its momentum (p) is known. Typically, in an electron microscope, electrons are accelerated to hundreds of KeV, corresponding to theoretical resolutions lower than 0.004 nm. In reality, TEMs have much lower resolution due to relativistic effects and defects in the electromagnetic lensing. That said, High Resolution TEMs (HR-TEMs) can resolve details in the sub-nanometric domain (Å) through brighter electron sources and more stable electronics and goniometers.

In general, TEMs consist of an electron source, a vertical column in which the electron beam is accelerated, the sample area with a sample holder and the camera (Fig. 2.15). Electromagnetic coils (i.e. lenses) are positioned before and after the sample bending the electron beam to change its focal point on the sample and on the camera lens. The entire TEM is held at ultra high vacuum conditions to reduce scattering and absorption by gas atoms.

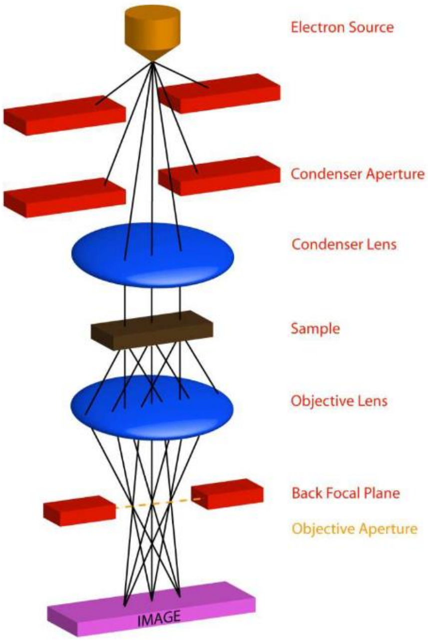

Figure 2.15 Schematic representation of the TEM column

The most common electron source is a tungsten filament heated to 2500 °C. At these temperatures, electrons can obtain energy greater than the work function of the material and are able to escape it, a phenomenon called thermoionic emission. The electrons emitted in all directions are selected, focused and accelerated by the condenser aperture and the electric field present in the TEM column. The applied potential in the column can vary between 100 and 400 KeV, depending on the sample properties and the resolution needs. Another important electron source for HR-TEM is the Field Emission Gun (FEG). This source works at lower temperatures (300 °C) and is composed of a tungsten filament sharpened to an extremely fine tip (~ 1 μm). Given the lower operating temperatures FEGs tend to have longer life spans, but also very high light coherence and brightness due to the small emission tip. Once the condenser lens system forms a parallel beam, the sample can interact with the electrons leaving some transmitted and others diffracted (Fig. 2.16). Another set of objective lenses can focus again the beam on the plane of the image sensor (the Back Focal Plane, BFP). The diffracted electrons can be studied through a Fourier Transform, revealing information on the crystallographic nature of the sample, similarly to X-ray diffraction. Through modification of the objective aperture, it is also possible to focus on diffraction patterns coming from selected structures in the sample (Select Area Diffraction, SAD). At this point, it is possible to form an image from the transmitted electrons (the central bright spot in a SAD pattern), creating what is called as Bright Field (BF) image.

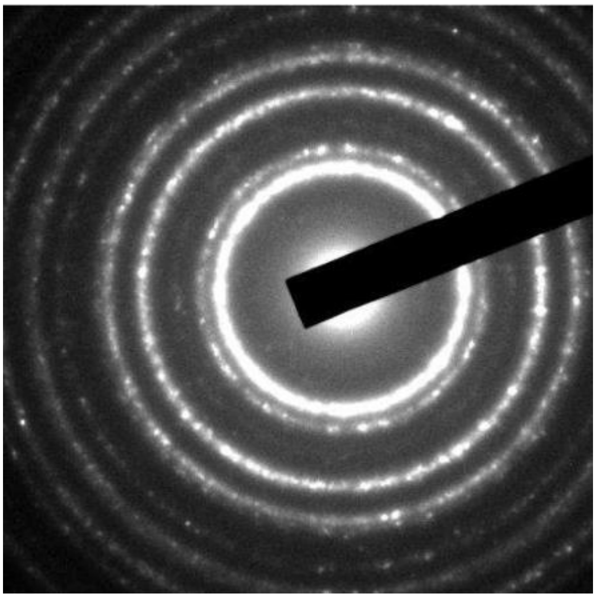

Figure 2.16 A SAD diffraction pattern with transmitted electrons in the center, and scattered electrons in concentric rings.

The scattered electrons can be collected through an Annular Dark Field (ADF) detector and used to create an image (DF image). The ADF can collect electron scattered with an angle between 10 and 50 mrad from the beam axis. Finally, High Angle Annular Dark Field (HAADF) detectors can collect electrons scattered at angles higher than 50 mrad and are particularly sensitive for high Z (atomic number) elements. As the names suggest, BF and DF images have opposing contrast features: if in bright field, species with high Z are darker than the background (because they scatter more electrons), in dark field images the bright spots are given by the highest scattering species.

Other than transmission and diffraction (i.e. elastic processes), the electrons can also transfer energy to the material. This energy can have unwanted effects on the sample itself, heating it (especially problematic with biological samples) or even kickstarting a reaction (i.e. reduction processes). If the transferred energy is absorbed by core electrons, it can result in X-ray emission from the relaxation of a valence electron to the core hole. The frequency of these photons is determined by the difference between core and valence level energies and is characteristic of the element from which it was emitted. If the number of counts is plotted against the photon energy, the spectra are called Energy Dispersive X-ray spectroscopy (EDX).[12] Another way to get chemical information about the sample is through Electron Energy Loss Spectroscopy (EELS) in which an electron spectrometer is used to measure the energy loss of the electron beam after any inelastic process has occurred.[13] EELS can also be used to extract information on oxidation states [14] and surface and depth discrimination in elemental mapping.[15] However, EELS and EDX should be seen more as complementary techniques: while EELS is most sensible to light elements, EDX is preferred for heavier ones, because light elements tend to relax emitting an Auger electron rather than a photon.[16]

Finally, the use of these techniques in conjunction with transmission electron microscopy, sheds light on not only the chemical and morphological composition of single nanostructures, but can also be used to track modifications during catalytic operation trough *in operando* measurements: the development of new sample holders that grant for contact of the sample to liquid or gas phases, has allowed to track modifications in real time on a specific structure while the material itself is subjected to working conditions.[17,18]

References

(1) Bard, A. J. ; F. R. *Electrochemical Methods: Fundamentals and Applications, 2nd Edition | Wiley*; 2000.

(2) Elgrishi, N.; Rountree, K. J.; McCarthy, B. D.; Rountree, E. S.; Eisenhart, T. T.; Dempsey, J. L. A Practical Beginner's Guide to Cyclic Voltammetry. *Journal of Chemical Education* **2018**, *95* (2), 197–206. https://doi.org/10.1021/ACS.JCHEMED.7B00361/SUPPL_FILE/ED7B00361_SI_002.DOCX.

(3) Mulder, W. H.; Sluyters, J. H.; Pajkossy, T.; Nyikos, L. Tafel Current at Fractal Electrodes: Connection with Admittance Spectra. *Journal of Electroanalytical Chemistry and Interfacial Electrochemistry* **1990**, *285* (1–2), 103–115. https://doi.org/10.1016/0022-0728(90)87113-X.

(4) Yuan, X.-Z.; Song, C.; Wang, H.; Zhang, J. EIS Equivalent Circuits. *Electrochemical Impedance Spectroscopy in PEM Fuel Cells* **2010**, 139–192. https://doi.org/10.1007/978-1-84882-846-9_4.

(5) Zhou, R.; Zheng, Y.; Jaroniec, M.; Qiao, S.-Z. Determination of the Electron Transfer Number for the Oxygen Reduction Reaction: From Theory to Experiment. *ACS Catalysis* **2016**, *6* (7), 4720–4728. https://doi.org/10.1021/acscatal.6b01581.

(6) F., J. J. Textbook of Quantitative Inorganic Analysis. *Nature 1937 139:3524* **1937**, *139* (3524), 821–821. https://doi.org/10.1038/139821a0.

(7) Bower, C. E.; Holm-Hansen, T. A Salicylate–Hypochlorite Method for Determining Ammonia in Seawater. *Canadian Journal of Fisheries and Aquatic Sciences* **1980**, *37* (5), 794–798. https://doi.org/10.1139/f80-106.

(8) Sing, K. S. W. Reporting Physisorption Data for Gas/Solid Systems. *Pure and Applied Chemistry* **1982**, *54* (11), 2201–2218. https://doi.org/10.1351/PAC198254112201.

(9) Lábár, J. L. Consistent Indexing of a (Set of) Single Crystal SAED Pattern(s) with the ProcessDiffraction Program. *Ultramicroscopy* **2005**, *103* (3), 237–249. https://doi.org/10.1016/J.ULTRAMIC.2004.12.004.

(10) Moreno, M. S.; Jorissen, K.; Rehr, J. J. Practical Aspects of Electron Energy-Loss Spectroscopy (EELS) Calculations Using FEFF8. *Micron* **2007**, *38* (1), 1–11. https://doi.org/10.1016/J.MICRON.2006.03.011.

(11) Plodinec, M.; Nerl, H. C.; Farra, R.; Willinger, M. G.; Stotz, E.; Schlögl, R.; Lunkenbein, T. Versatile Homebuilt Gas Feed and Analysis System for Operando TEM of Catalysts at Work. *Microscopy and Microanalysis* **2020**, *26* (2), 220–228. https://doi.org/10.1017/S143192762000015X.

(12) Bazin, D. C.; Sayers, D. A.; Rehr, J. J. Comparison between X-Ray Absorption Spectroscopy, Anomalous Wide Angle X-Ray Scattering, Anomalous Small Angle X-Ray Scattering, and Diffraction Anomalous Fine Structure Techniques Applied to Nanometer-Scale Metallic Clusters. *Journal of Physical Chemistry B* **1997**, *101* (51), 11040–11050. https://doi.org/10.1021/JP9721311.

(13) Egerton, R. F. Electron Energy-Loss Spectroscopy in the TEM. *Reports on Progress in Physics* **2008**, *72* (1), 016502. https://doi.org/10.1088/0034-4885/72/1/016502.

(14) Riedl, T.; Gemming, T.; Gruner, W.; Acker, J.; Wetzig, K. Determination of Manganese Valency in La1−xSrxMnO3 Using ELNES in the (S)TEM. *Micron* **2007**, *38* (3), 224–230. https://doi.org/10.1016/J.MICRON.2006.06.017.

(15) Xin, H. L.; Dwyer, C.; Muller, D. A.; Zheng, H.; Ercius, P. Scanning Confocal Electron Energy-Loss Microscopy Using Valence-Loss Signals. *Microscopy and Microanalysis* **2013**, *19* (4), 1036–1049. https://doi.org/10.1017/S1431927613001438.

(16) Goldstein, J. I.; Newbury, D. E.; Michael, J. R.; Ritchie, N. W. M.; Scott, J. H. J.; Joy, D. C. Scanning Electron Microscopy and X-Ray Microanalysis. *Scanning Electron Microscopy and X-ray Microanalysis* **2017**, 1–550. https://doi.org/10.1007/978-1-4939-6676-9.

(17) Gong, C.; Pu, S. D.; Gao, X.; Yang, S.; Liu, J.; Ning, Z.; Rees, G. J.; Capone, I.; Pi, L.; Liu, B.; Hartley, G. O.; Fawdon, J.; Luo, J.; Pasta, M.; Grovenor, C. R. M.; Bruce, P. G.; Robertson, A. W. Revealing the Role of Fluoride-Rich Battery Electrode Interphases by Operando Transmission

Electron Microscopy. *Advanced Energy Materials* **2021**, *11* (10), 2003118. https://doi.org/10.1002/AENM.202003118.

(18) Wang, X.; Klingan, K.; Klingenhof, M.; Möller, T.; Ferreira de Araújo, J.; Martens, I.; Bagger, A.; Jiang, S.; Rossmeisl, J.; Dau, H.; Strasser, P. Morphology and Mechanism of Highly Selective Cu(II) Oxide Nanosheet Catalysts for Carbon Dioxide Electroreduction. *Nature Communications 2021 12:1* **2021**, *12* (1), 1–12. https://doi.org/10.1038/s41467-021-20961-7.

The Oxygen Reduction Reaction

3.1 Introduction

Oxygen, as one of the most readily available elements on Earth, is a very interesting reagent that can be consumed at the cathode in a Fuel Cell. Usually, in the context of PEMFCs (i.e. in acidic environments), the reaction of interest is the one proceeding via a 4 e^- process, that leads to the formation of water ($O_2 + 4H^+ + 4e^- \rightarrow 2\ H_2O$). This reaction is considerably more complex than the $2e^-$ process for the Hydrogen Oxidation Reaction (HOR) at the anode, because involves four consecutive coupled electron-proton transfers. In particular, the 4 e^- pathway can either proceed with dissociative or associative steps depending on the energetics on the catalytic surface:[1]

Dissociative:
$O_2 + 2^* \rightarrow 2O^*$ (1)
$2O^* + 2H^+ + 2e^- \rightarrow 2OH^*$ (2)
$2OH^* + 2H^+ + 2e^- \rightarrow 2H_2O + 2^*$ (3)
Associative:
$O_2 + ^* \rightarrow O_2^*$ (4)
$O_2^* + H^+ + e^- \rightarrow OOH^*$ (5)
$OOH^* + H^+ + e^- \rightarrow O^* + H_2O$ (6)
$O^* + H^+ + e^- \rightarrow OH^*$ (7)
$OH^* + H^+ + e^- \rightarrow H_2O + ^*$ (8)

If the reduction takes place through the associative pathway, there is an interesting possibility arising, where before the O-O bond breakage (6) the adsorbed peroxyl radical can lead to the formation of hydrogen peroxide through an electron-proton transfer:[2]

$OOH^* + H^+ + e^- \rightarrow H_2O_2 + ^*$ (9)

The first instances of H_2O_2 being produced at a platinum electrode during electrolysis were proposed in the 1930s by Glasstone and Hickling.[3] Of course, hydrogen peroxide is a relatively unstable molecule, especially at low concentrations,[4] and can either decompose spontaneously (particularly at alkaline pH) or be further reduced to H_2O if it is kept near the electrodic surface. This can happen because the binding energy of the peroxyl radical to the catalytic surface is too high, leading to an energy barrier for the detachment of the radical, favouring the reduction to water.[5] In many carbon-based materials, porosity is very important, because it can favour reactant mass transport to the electroactive site, but it could also slow down H_2O_2 diffusion, leading to its reduction.[6–8]

If produced in low concentrations, hydrogen peroxide can be seen as an undesirable by-product in a fuel cell, because it has been shown to be detrimental to Nafion membranes. H_2O_2 attacks both main and side chain though radical depolymerization.[9] This was particularly evident if iron or copper ions are present in solution, not unlikely with Cu- and Fe-based catalysts that could leach out in time or with iron being a major contaminant in many electrolytes (i.e. alkali hydroxides).[10,11] On the other hand, if hydrogen peroxide is produced in significant quantities, this reaction could be a very interesting alternative in lieu of the chemical route in use now[12] Its production currently relies on a strategy involving high energy intensive steps and therefore poorly sustainable: the main source of industrial hydrogen peroxide for a 3.5Mt per year production is based on the anthraquinone process (Fig. 3.1), developed in 1939 by BASF. The reaction involves a catalytic cycle in which the anthraquinone molecule is first hydrogenated on a palladium catalyst, followed by oxidation with atmospheric oxygen (usually supplied in the form of compressed air). The produced H_2O_2 has found applications spanning the rocket industry,[13] organic oxidations (and the synthesis of organic peroxides), wastewater management[14] and the production of paper in the pulp industry.[15] Hydrogen peroxide is considered to be one of the "greenest" oxidants because only water is produced as a by-product of its oxidation.

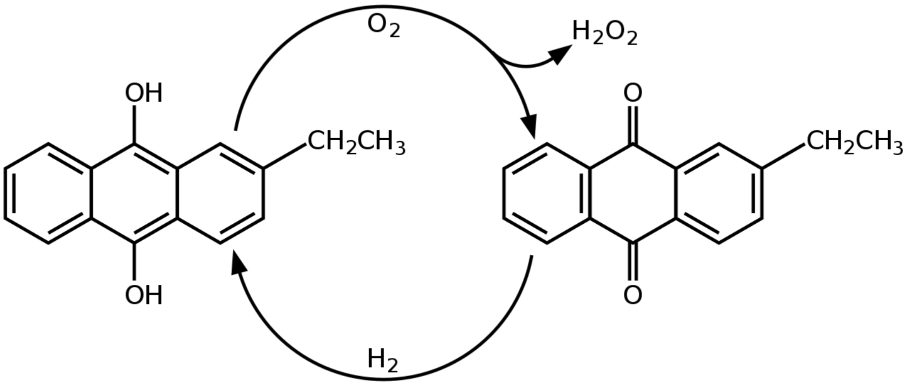

Figure 3.1 The catalytic cycle involved in the synthesis of H_2O_2 through the anthraquinone process.

From a green chemistry perspective, the main drawbacks of the anthraquinone process are the use of a PGM (Platinum Group Metal) catalyst and its loss through cycling, the use of organic solvent and the cost of the anthraquinone medium. Although all these factors impact the cost-effectiveness of the production, the anthraquinone process still represent the dominant strategy for the bulk of hydrogen peroxide production. In this landscape, H_2O_2 electrosynthesis, together with photosynthetic[16] and other greener chemical routes,[17] has been undergoing an increasing scientific interest, addressing either the development of new active and selective electrocatalysts than the multi-component structure of the fuel cell. However, in view of the high availability of the starting material (molecular oxygen, O_2) and the net positive current produced by the fuel cells, the ORR process can be an effective alternative to the energy-intensive anthraquinone process, while decentralizing production through the use of medium to big scale fuel cell stacks.

In this landscape, both possible products of ORR are attractive for different reasons. For applications where the highest power density is needed (i.e. portable FCs), the $4e^-$ process is most desirable and the attention has typically focused on small scale devices that are compact and light (i.e. in cars). This can be possible only with catalytic materials that minimize the reaction overpotentials (delivering the highest peak current at a fixed voltage), while limiting the production of the H_2O_2 intermediate to avoid potential harm to the membrane. As of today, carbon supported platinum is the accepted standard for the cathodic reaction in FCs, because it can sustain high current densities and low H_2O_2 production.[18] However, platinum is an extensively used metal in catalysis and this reflects in very high material demand, and thus cost. Moreover, platinum catalysts are sensitive to deterioration in time and CO poisoning.[19] Alternatives include earth-abundant metals supported on carbon[20,21] or even non-metallic catalysts.[22,23] Current trends, then, focus on minimization of mass loading in Pt-based catalysts[24] or exceeding its activity with other, more sustainable, materials.[25]

On the other hand, the $2e^-$ pathway has recently been object of intensified investigation, because its use could lead to combined H_2O_2 and power production. The use of different nanocomposite materials has been studied mostly based on doped carbons[26–29] and earth-abundant metals,[30–33] such as nickel, iron and cobalt.[34] The electrolyte is also a fundamental variable in the system. Neutral pH electrolytes could unlock cheap ways to synthetize medical-grade H_2O_2 to use as a disinfectant, even if the low concentration of either H^+ or OH^- hinders kinetics.[35] Alkaline and acidic electrolytes usually enable higher catalytic activities and are thus more interesting from an industrial perspective, but H_2O_2 is unstable at high pHs,[4,36] while acidic environments can be problematic for many metal-based catalysts. In this chapter, two materials for the Oxygen Reduction Reaction will be explored, one based on platinum porous nanocrystals for the 4e- process and one on a cobalt carbon nanocomposite for the 2e- process.

3.2 Porous Multifaceted Platinum Nanoparticles for electrocatalysis

As mentioned in the introduction, commercial PEMFCs currently operate thanks to platinum-based electrodes to ensure the best performances for these devices. Still, the high cost of the catalyst component is a hurdle toward further commercialization. Two trends have emerged on ORR catalyst research. The first is focused on the optimization of platinum catalysts to obtain the best possible mass activity (i.e. current normalized over platinum mass), through alloying, nanostructuring or other techniques.[37–39] The second trend is the research over different materials that can perform as good as platinum, either of the PMG family or of other earth-abundant materials.

3.2.1 Experimental Section

Materials. Oleylamine technical grade 70% (OLAM), oleic acid technical grade 90% (OLAC), benzyl ether 98%, ethanol 99.8%, methanol 99.8%, isopropanol 99.9%, toluene 99.7%, acetone 99.5%, conc. $HClO_4$ 70%, H_2SO_4 99.999%, and Nafion® 117 5% solution were purchased from Sigma-Aldrich. Platinum(II) 2,4-pentanedionate (49.6% Pt) was purchased from Chempur, and Vulcan XC72R was supplied from Cabot. The 20% Pt on the carbon used as the standard was bought from Alfa Aesar. All electrochemical experiments were performed with Milli-Q water obtained by using a Direct-Q (Millipore) water purification system. All the glassware used for the synthesis and deposition process of porous platinum NPs were previously cleaned with aqua regia (HCl/HNO_3 = 3/1) and then rinsed with Milli-Q water.

Synthesis of Porous multifaceted platinum nanoparticles (p-Pt). The p-Pt NPs were prepared by a surfactant-assisted process inspired by a previous protocol used in our group.[40] In a typical synthetic procedure, a three-necked 25 mL round-bottom flask, equipped with a stirring bar and internal thermometer, was flame-dried under vacuum and then purged with argon. Subsequently, 20 mg of $Pt(acac)_2$ (0.05 mmol), 2 mL of OLAM 70% (6.43 mmol), 2 mL of OLAC (7.11 mmol), and 10 mL of benzyl ether were added under argon flow to the flask and stirred at 100 °C using an oil bath for 10 min to completely dissolve the platinum complex and remove water traces. The temperature was then increased at 200 °C (5 °C min^{-1}), the flask was sealed, and the argon flow was stopped to better control the temperature. The reaction mixture was left to stir at 400 rpm for 1 h. At reaction completion, the flask was cooled to room temperature, ethanol was added (15 mL), and NPs were precipitated by centrifugation at 5000 rpm for 6 min and washed with ethanol/n-hexane 3 times and centrifuged again. Finally, the product was redispersed in n-hexane.

Preparation of Sintered Pt NP (s-Pt). Sintered platinum nanoparticles on Vulcan were prepared starting from NaOH-treated NPs. Twenty milligrams of NaOH-treated porous Pt NPs on Vulcan was transferred to a 30 mL quartz tube reactor connected to a H_2/Ar line. The catalyst was first purged with Ar at room temperature for 30 min and then heated at 400 °C (ramp: 5 °C min–1) under 100 mL min^{-1} H_2/Ar (3% H_2) flow for 4 h.

Deposition of Pt NPs on Vulcan carbon. p-Pt and s-Pt on carbon were prepared by impregnation in an organic solvent. Typically, 50 mg of Vulcan XC72R was dispersed in 50 mL of toluene and sonicated for 30 min, and then the dispersion was stirred vigorously. Afterward, 10 mg of Pt NPs in 10 mL of n-hexane was added dropwise under constant stirring, and the suspension was left to stir for an additional 3 h. The as-prepared Pt/C was centrifuged at 5000 rpm for 12 min and washed 3 times with methanol before drying in vacuum at 60 °C for 12 h. For methanol/NaOH treatment,[41] the dried catalyst was suspended in methanol followed by 150 mg of NaOH addition. The suspension was sonicated for 20 min until complete NaOH dissolution, and then the catalyst was collected by centrifugation at 5000 rpm for 12 min and washed with acetone (this procedure was repeated 3 times). The last washing step was performed with bi-distilled water, and the catalyst was filtered before drying at 60 °C under vacuum for 12 h.

Electrochemical Measurements. All the inks were prepared in a 3:1 H_2O:iPrOH mixture with the addition of a lowered volume of Nafion solution of 0.05% (v/v) and a catalyst concentration of 5 mg mL^{-1}. The ink was drop-casted on a polished GC-RDE in 8 μL drops till a loading of 30 μg_{Pt} cm^{-2} was reached for every experiment and dried in air flow with an RDE rotation rate of 700 rpm. All the characterizations were done following the procedures reported by Shinozaki et al.[42,43] To completely clean the surface of the nanoparticles from any possible residue, 200 cycles of CV were used at 0.5 V s^{-1} between 0 and 1.2 V vs RHE. During this conditioning, the hydrogen adsorption and desorption peaks became more accentuated and symmetric until a stable response from the material was obtained. Although this method results in some reconstruction of the platinum surface in respect to other cleaning procedures (e.g. flame annealing),[44] it is still the most widely accepted for nanoparticles on carbon support.

Two parameters were chosen to compare different catalytic results, specific activity (SA, mA cm_{Pt}^{-2}) and mass activity (MA, mA mg_{Pt}^{-1}), both measured at potentials of interest for the specific catalytic reaction. In order to evaluate the ElectroChemical Surface Area (ECSA) of the platinum NPs, many different procedures can be found in the literature, resulting in high variability in ECSA values (even in orders of magnitude).[45] Here, we followed the most straightforward procedure based on the integration of the hydrogen under potential deposition (H_{upd}) related peaks in the CV performed at 0.1 V s^{-1}. The ECSA was obtained by dividing the as obtained charge with the standard value of 210 μC cm^{-2}, normalized for the Pt NPs mass. Roughness factors (RF) were calculated as ECSA values times the material loading:

$$ECSA = \frac{Q_{UPD}\ (\mu C)}{210\ \mu C\ cm^{-2}} \frac{1}{m_{Pt}} \qquad\qquad RF = ECSA \cdot \frac{m_{Pt}}{SA_{geo}}$$

Characterization. High-resolution TEM (HR-TEM) images, selected-area electron diffraction (SAED) patterns, and high-angle annular dark field (HAADF) scanning TEM (STEM) were acquired by using a JEOL 2010 UHR field emission gun microscope operated at 200 kV with a measured spherical aberration coefficient Cs of 0.47 ± 0.01 mm. The electron dose rate was 1.5 × 10–8 e/sÅ^2 for regular and HR-TEM imaging. HAADF-STEM images were acquired using an illumination angle of 12 mrad and a collection angle of $88 \leq 2\theta \leq 234$ mrad.

3.2.2 Results and Discussion

Synthesis and characterization. The synthesis of porous platinum NPs enriched in (111) planes was performed in prof. Lucia Pasquato’s group, in dibenzyl ether, a high boiling point solvent, to easily reach the metal thermal reduction temperature (for platinum ca. 200 °C). A synoptic overview of the electron microscopy characterization for the obtained NPs is presented in Fig. 3.2. HAADF-STEM and TEM images (Fig. 3.2a,b, respectively) show that the obtained dendritic NPs have remarkably uniform shape and a narrow particle size distribution, with a mean diameter of around 52 ± 2 nm for a set of ∼400 particles is measured as shown in the histogram of Fig. 3.2c.

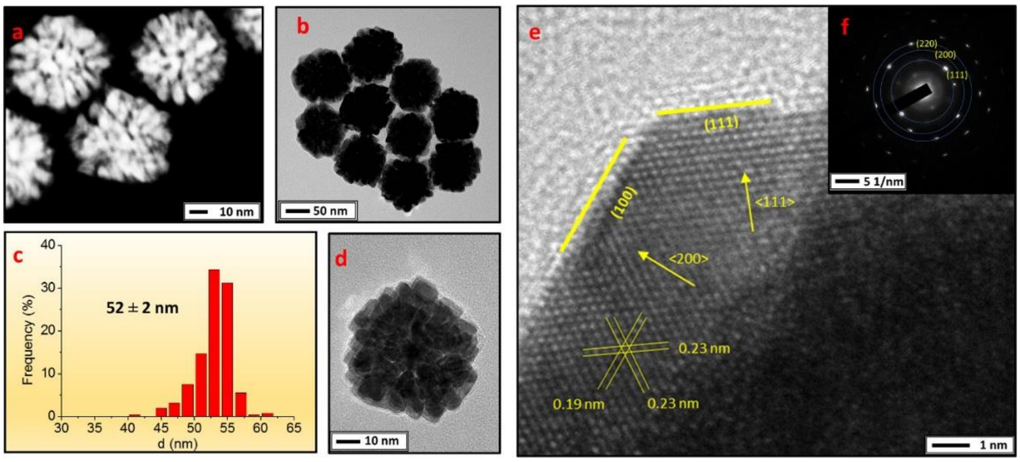

Figure 3.2 Representative HAADF-STEM image of the Pt NPs (a); low magnification (b), dimensional analysis (c), and high magnification (d) TEM images of the NPs; HR-TEM image of the Pt crystallite (e) and selected-area ED patterns (f).

A notable feature of these NPs is the regular edges that decorate their surface as observed in Fig. 3.2b,d. The high-magnification micrograph of a single particle (Fig. 3.2d) highlights the porous structure and abundant presence of shaped crystallites with an average dimension of 10 ± 1 nm. The crystallites are well oriented and hierarchically assembled to constitute the porous NPs themselves. The HR-TEM image of the crystallites unveils well-defined terraces composed of uniform low-indexed planes as evinced in Fig. 3.2e. In addition, from the SAED pattern (Fig. 3.2f), the main diffraction rings of the first reflections of the Pt face-centered cubic (fcc) lattice (111), (200), and (220) planes can be identified. The well-defined bright spots on the diffraction ring patterns indicate the high crystallinity of the synthesized NPs. Surface area measurements were performed on the Pt NPs to support their potential application in catalysis. BET surface area of 15.4 $m^2\ g^{-1}$ was measured through nitrogen adsorption/desorption isotherms (Fig. 3.3), and it is consistent with previously reported wet syntheses of porous Pt nanostructures from organic phase.[46] The adsorption/desorption isotherm shape seems to indicate low porosity, while the slight hysteresis between the two isotherms with no limiting adsorption at high p/p^0 is associated with capillary condensation taking place in slit-shaped mesopores, due to the faceted nature of the nanoparticles. A pore size distribution could be calculated for unsupported NPs from the BJH analysis of the adsorption branch of the isotherm (Fig. 3.3 inset). Due to this material’s tendency to aggregate when not supported, the average pore diameter was calculated as 35 nm, much larger than the voids observed in the porous Pt NPs by TEM analyses. This result indicates that the major contribution to the pore volume in the dried sample is related to the voids formed in the porous Pt NPs aggregates, with the inner space between the aggregated crystallites being overshadowed.

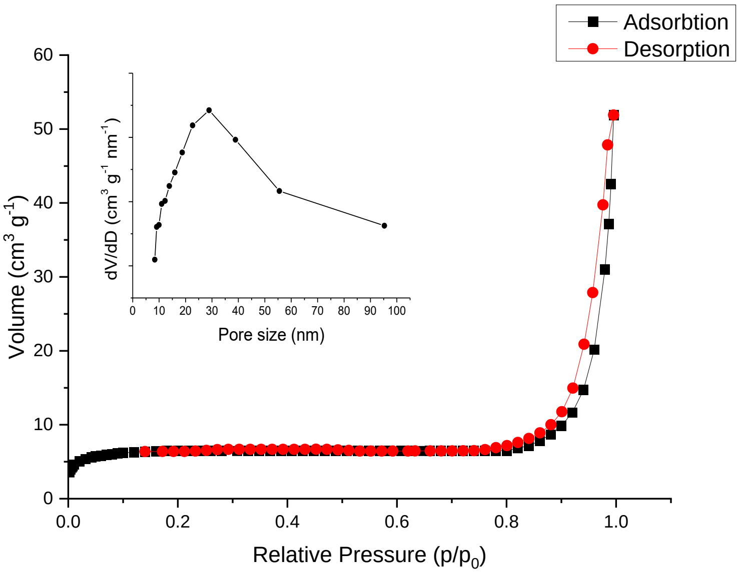

Figure 3.3 Nitrogen adsorption-desorption isotherm of the porous multifaceted Pt NPs. Inset: pore size distribution curve obtained with the BHJ method from the desorption branch.

TEM analysis was used to follow the crystallite growth in time.[47] The start of the temperature ramp from 100 to 200 °C was arbitrarily chosen as time zero, and small aliquots (0.2 mL) of the reaction mixture were withdrawn every 5 or 10 min and analyzed after a quick purification step (hexane/ethanol washing and centrifugation at 15,000 rpm). The electron dose rate and the image acquisition conditions were properly set to avoid unwanted beam effects. The growth process and morphology evolution of the Pt NPs are summarized in Fig. 3.4. It was observed that after 5 min of reaction time (Fig. 3.4a), small cubic NPs with an average size of 8 ± 1 nm form. The nucleation stage of p-Pt nanostructures usually involves the formation of polycrystalline seeds or small dendrites[48–50] due to the fast kinetically controlled reduction of the platinum precursor. The use of OLAM and OLAC (added simultaneously at room temperature), known for their ability to be adsorbed on specific facets, promotes the directional growth of NPs.[51] First, the growth of ⟨111⟩ axes produces cubes with elongated vertexes, then, at 20 min (Figure 3.4d), it can be seen the deposition of small polycrystalline clusters on the star-shaped NPs giving rise to porous dendrites that grow to the final p-Pt morphology (Fig. 3.4h). This latter behavior suggests a thermodynamic control driving the NP surface energy to its minimum. Nevertheless, this reaction achieves a narrow size distribution of the nanoparticles, contrary to many reported methodologies for porous nanoparticles,[52–54] where an ill-defined size distribution is usually reported.[50,55,56]

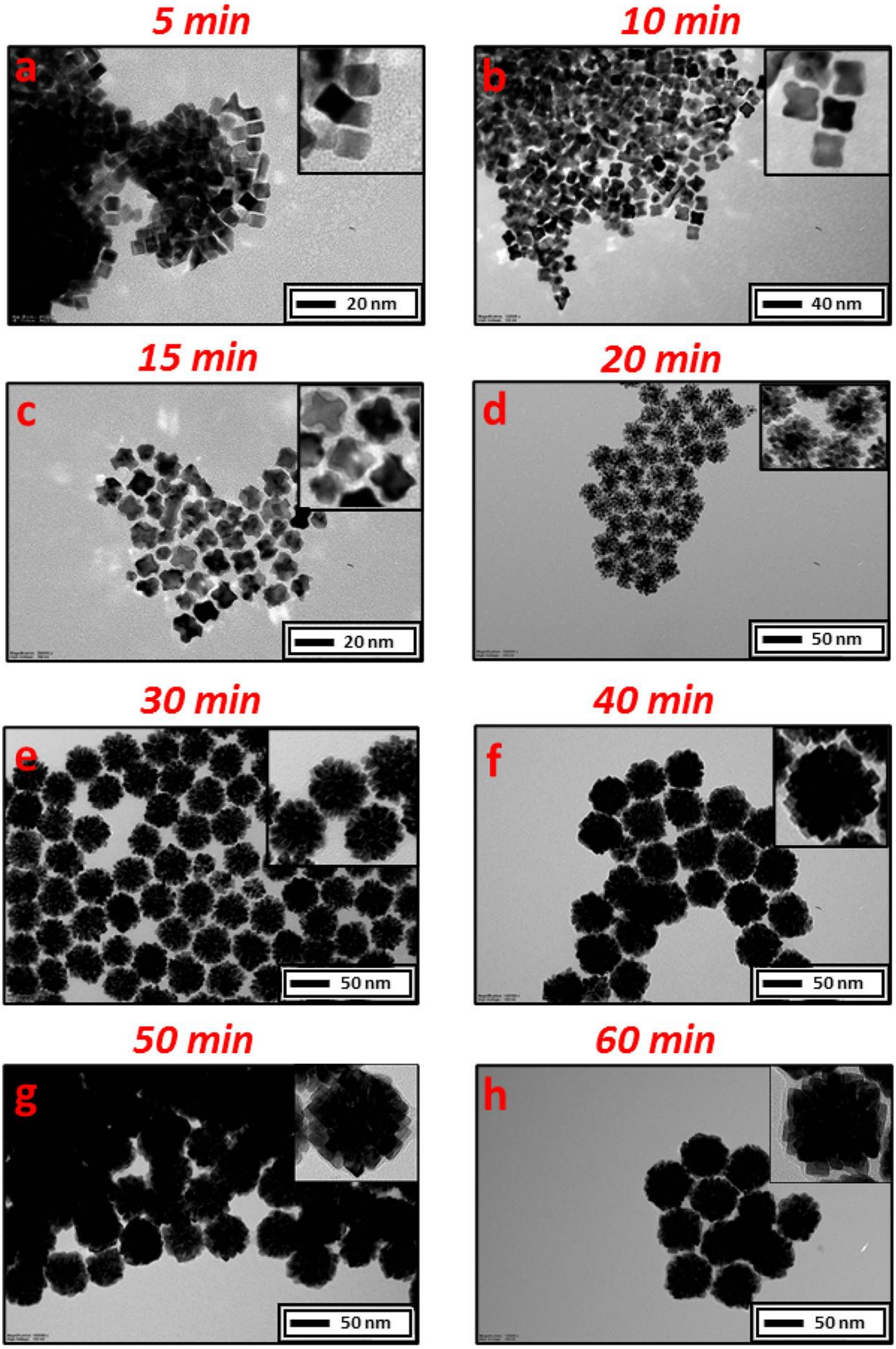

Figure 3.4 Typical TEM images representing the size and shape progression of the porous Pt NPs at 5 (a), 10 (b), 15 (c), 20 (d), 30 (e), 40 (f), 50 (g), and 60 min (h).

The synthesized p-Pt NPs were deposited via impregnation on a Vulcan XC72R support to obtain suitable materials for electrocatalytic studies. To put into context its catalytic activity with respect to other forms of platinum over carbon, two different reference materials were considered. One consisted of a commercial Pt/C material from Alfa as the industry standard reference. The other reference material was obtained by subjecting p-Pt NP to sintering under H_2 at 400°C, in order to define the contribution of pores or distinct facets. Importantly in relation to cost-effectiveness, the synthetized composites Pt/Vulcan (p-Pt and s-Pt NPs) materials were prepared with a metal loading of 15 wt%, as determined by ICP-OES analysis, while the commercial Pt/C had a nominal loading of 20 wt%, confirmed through ICP measurement. As expected, the pristine Vulcan XC72R shows a higher surface area and pore volume than the composite porous Pt NPs/Vulcan material, considering the higher density of Pt with respect to the carbon support. Notably, after sintering of the composite porous Pt NPs/Vulcan under H_2 at 400 °C, no significant modifications of the textural properties are observed (Tab. 3.1).

	S_{BET} [a] ($m^2\ g^{-1}$)	S_{ext} [b] ($m^2\ g^{-1}$)	S_{micro} [c] ($m^2\ g^{-1}$)	V_{tot} [d] ($cm^3\ g^{-1}$)	V_{micro} [e] ($cm^3\ g^{-1}$)	V_{meso} [f] ($cm^3\ g^{-1}$)	D_M [g] (nm)
Vulcan	200	146	54	0.604	0.036	0.568	51
P-Pt/Vulcan	140	125	15	0.627	0.012	0.615	63
comm. Pt/C	138	106	32	0.503	0.022	0.481	59
s-Pt/Vulcan	140	113	27	0.525	0.019	0.506	53

[a] Specific surface area calculated following the BET method.

[b] Specific surface area external to micropores, determined from the t-plot analysis.

[c] Specific surface area of micropores.

[d] Total volume of pores calculated from BJH analysis.

[e] Total volume of micropores, determined from t-plot analysis.

[f] Total volume of mesopores.

[g] Maximum of the pore size distribution, determined by BJH analysis

Table 3.1 Summary of the textural properties for the investigated materials.

H_2 chemisorption experiments have been performed on the various Pt/C materials to analyze the Pt-exposed surface area. Data obtained from treatment of the H_2 chemisorption isotherms (Fig. 3.5) is summarized in Table 3.2. The composite p-Pt NPs/Vulcan chemisorbed a remarkably lower amount of H_2 with respect to the commercial Pt/C material. As a consequence, metal dispersion and exposed surface areas (reported irrespectively of the mass of the catalyst or to the mass of Pt) are lower, and the apparent metal particle size is larger for the composite p-Pt/Vulcan material. It is straightforward to note that, in the composite porous Pt/Vulcan material, the exposed metal surface area reported with respect to the mass of Pt is 18.1 m^2 g_{Pt}^{-1}, which is very close to the value of 15.4 m^2 g_{Pt}^{-1} measured by N_2 physisorption on the pristine porous Pt NPs, even considering the intrinsic systematic errors of the two different techniques.

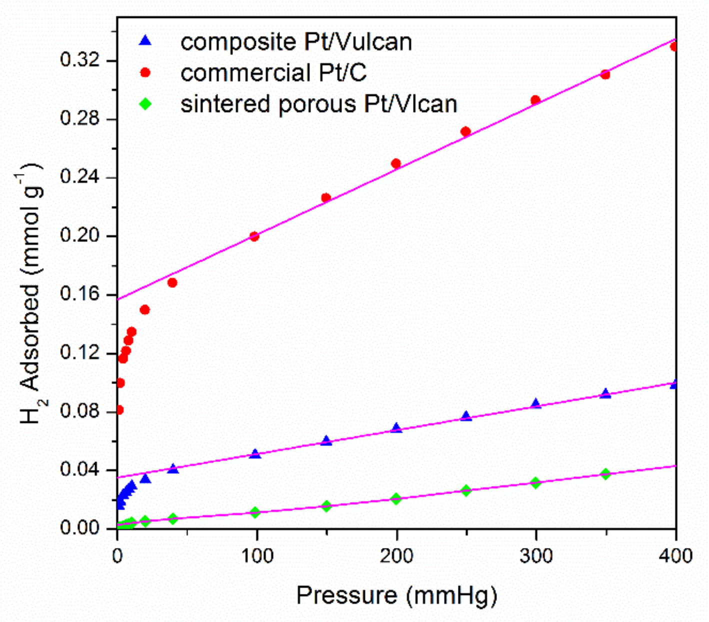

Figure 3.5 H_2 chemisorption measurements for porous multifaceted Pt on Vulcan and commercial Pt on carbon.

	D % [a]	*d_{part}* [b] *(nm)*	*$EMSA_{cat}$* [c] *(m^2 g^{-1})*	*$EMSA_{Pt}$* [d] *(m^2 g^{-1})*
comm. Pt/C	23.9	5.0	11.8	59.1
p-Pt/Vulcan	7.3	15	2.7	18.1
s-Pt/Vulcan	0.4	280	0.14	0.97

[a] Metal dispersion, calculated assuming a spherical shape of the metal particles.

[b] Apparent particle size.

[c] Exposed metal surface area (EMSA), expressed per quantity of catalyst.

[d] Exposed metal surface area (EMSA), expressed per quantity of platinum.

Table 3.2 Summary of the metal textural properties of the investigated materials.

Moreover, powder XRD analysis of the composite p-Pt/Vulcan material (Fig. 3.6) showed the typical reflection of metal Pt (JCPDS 04-0802), together with a very broad reflection around 26° due to the crystalline graphitic portion of Vulcan XC72R. The peak broadening of the (111) reflection of Pt is compatible with an average crystallite size of 11 nm, the same measured for the pristine porous Pt NPs. This result suggests that the porous nature of the Pt NPs is preserved during the various steps involved in the preparation of the composite porous Pt NPs/Vulcan (deposition protected porous Pt NPs and washing removed organic ligands). Notably, after the sintering treatment in H_2 at 400 °C, the exposed metal surface area drastically decreased, confirming the deep sintering on the Pt nanoparticles.

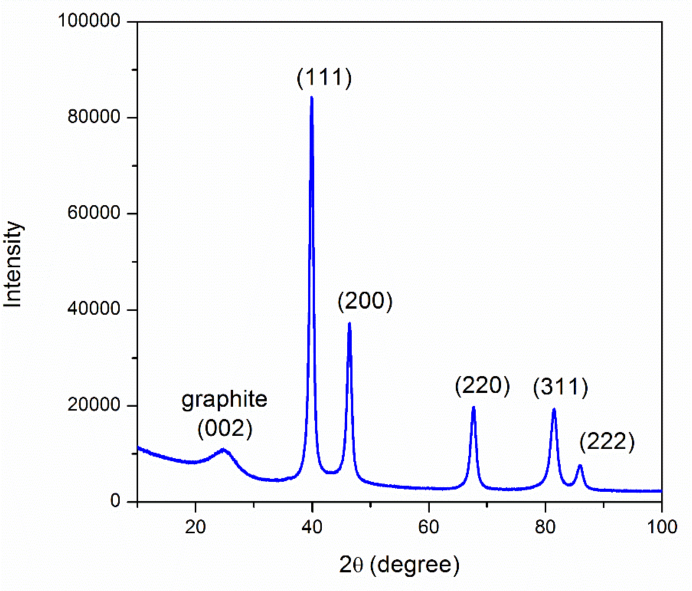

Figure 3.6 Powder x-ray diffraction pattern of the composite porous Pt NPs/Vulcan.

Finally, the morphology of the various Pt/C samples was analyzed by TEM and representative images are reported in Fig. 3.6. The commercial Pt/C sample (Fig. 3.7a) shows the presence of highly dispersed Pt nanoparticles, with a mean diameter of 3–4 nm. On the other hand, TEM images of the porous Pt/Vulcan composite material (Fig. 3.7b) shows the presence of the porous Pt NPs deposited on the carbonaceous support: despite the limited contrast due to the thickness of the support around the porous Pt NPs, the aggregation of various Pt crystallites to form a porous particle is clearly visible. After sintering by H_2 treatment at 400 °C, TEM analysis (Fig. 3.7c) confirms the coalescence of the Pt crystallite to form very large metal particles with spherical shapes. All the results obtained by TEM analysis of the supported Pt/C materials, investigated in electrocatalytic tests, are fully in agreement with the H_2 chemisorption results.

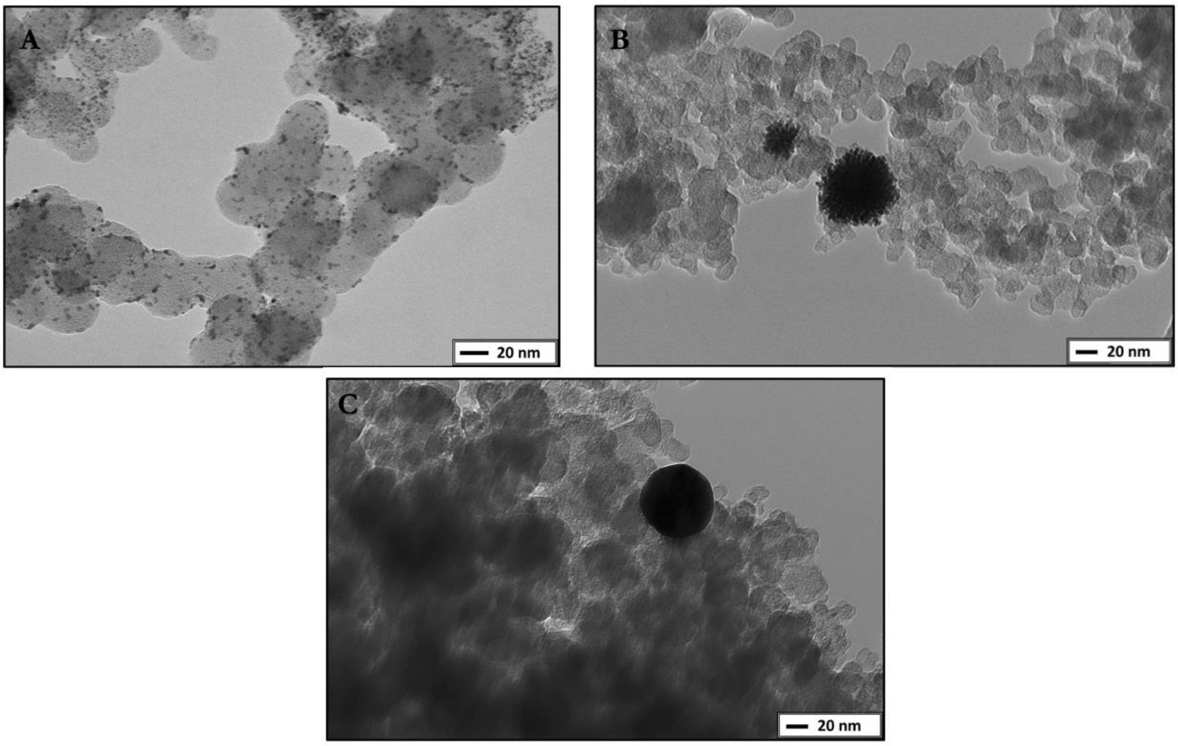

Fig. 3.7 Representative TEM images of (a) commercial Pt/C, (b) porous Pt/Vulcan and (c) sintered Pt/Vulcan nanocomposites.

Electrochemical characterization and catalysis. All materials were subjected to an initial pretreatment with cyclic voltammetries (CV) in $HClO_4$ at 0.5 V s^{-1} to clean and stabilize the platinum surface. During cycling, the Pt nanoparticles are able to either oxidize or desorb the remaining surfactant present on their surface by displacing it with an oxide layer (during oxidation) or a hydride layer (during reduction). The first CVs after this pretreatment step, registered at 0.1 V s^{-1}, show the classic features of Platinum in perchloric acid.[57] The characteristic CVs for the three materials tested are reported in Fig. 3.8. The profile of platinum CVs can be "separated" in three areas of interest, because they can be related to different phenomena on the surface: the hydrogen region, the double layer (DL) region, and the oxide region.[58] The DL region (0.4–0.6 V vs RHE) is mainly influenced by the carbon support: from the lower capacitive currents, we can infer that the Vulcan XC72R has less surface area accessible to the ions in solution than the carbon used in the commercial Pt/C. In the hydrogen region (0-0.4 V vs RHE), the formation of Pt hydrides can be related to features of the exposed platinum surfaces through the CV peaks. The position of each peak is indicative of the particular stability of different hydrides on different platinum facets (i.e. more stable at higher potentials). The commercial Pt/C material shows two close peaks at 0.15 and 0.2 V vs RHE: the first can be related to (110) step sites, the origin of the second peak is somewhat still debated and could arise from (111) sites.[57] Similarly, the composite porous Pt/Vulcan shows a peak at 0.13 V and one at 0.3 V vs RHE, with (110) and (100) step sites also present on the surface.

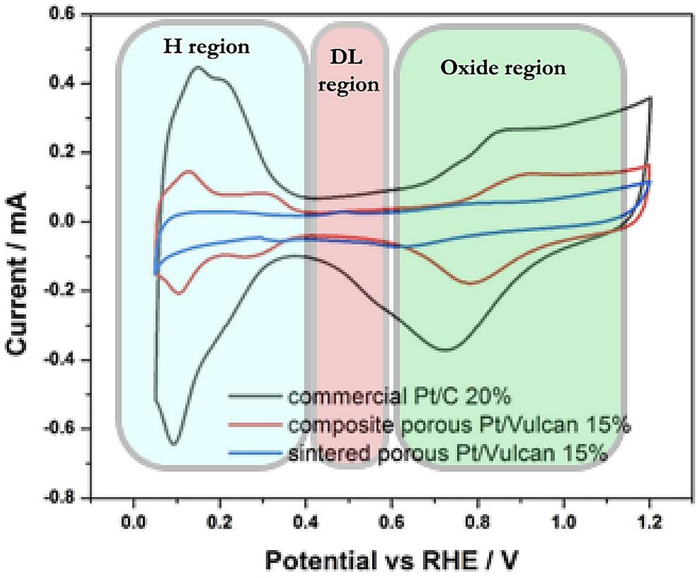

Figure 3.8 CVs for commercial Pt/C (black), porous Pt/Vulcan (red) and sintered Pt/Vulcan (blue), registered at 100 mV s^{-1} in $HClO_4$ after material pre-treatment.

ECSAs and RFs can be calculated for the three samples from the CVs (Tab. 3.3, for more details see Experimental Section). As expected, the commercial Pt/C material shows the highest electrochemical surface areas due to the very low dimensions of the Pt nanoparticles. Moreover, the cathodic and anodic sweeps of the composite p-Pt NPs/Vulcan material show very good symmetry in the hydrogen region. This indicates high reversibility of the hydride formation phenomena due to the clean after treatment of the catalyst with NaOH. The ECSA for the composite porous Pt NPs/Vulcan is one-half of that of the commercial reference material. After sintering, only 25% of ECSA is retained. Even if the trends are in good agreement with the ones observed by H_2 chemisorption, there is a significant difference in the calculated values: this discrepancy (between the values of metal surface area from electrochemical measurements and H_2 chemisorption) can be clearly related to the differences in the techniques. In fact, H_2 chemisorption is a gas-based measurement in which all the surface Pt atoms exposed to H_2 are “counted”, while the ECSA takes into account only the atoms that can be reached by diffusion of electrons in the overall assembly of the electrode/electrolyte (i.e. solid/liquid) interface.

	ECSA / $m_{Pt}^2\ g^{-1}$	RF
Comm. Pt-C 20%	6,3	1,9
Porous Pt-C	2,9	0,87
Sintered Pt-C	0,71	0,21

Tab. 3.3 Electrochemical surface areas (ECSAs) and Roughness Factors (RFs) of the investigated catalysts.

The ORR activity for all Pt-C composites was investigated through Linear Sweep Voltammetry (LSV). The tests were conducted in acid electrolyte (0.1 M $HClO_4$) in the potential window between 0.1 and 1.1 V vs RHE at a scan rate of 10 mV s^{-1}. The catalyst loading varied between samples to keep a fixed platinum loading of 30 µg cm^{-2}. The electrolyte was first saturated with Ar to register the background currents, then with pure O_2 for the actual catalytic test (Fig. 3.9). For the three materials, it is possible to observe two separate peaks in the ORR sweep (at 0.7 and 0.3 V vs RHE or commercial and p-Pt/C, less visible on s-Pt/C): this can be attributed to the different kinetics of the oxygen reduction reaction on platinum oxide and reduced platinum (the Pt reduction potential is between 0.7 and 0.8 V vs RHE as can be seen in Fig. 3.8). From the LSVs, activity data normalized for platinum mass and ECSA can be extracted to make comparisons (Fig. 3.10). The comparison of the obtained results highlights the importance of porosity of the Pt NPs in our material. The sweeps of commercial Pt/C and composite porous Pt NPs/Vulcan are very similar, showing higher activities per unit area for the porous nanoparticles. The composite porous Pt NPs/Vulcan shows comparable mass activity (MA) with respect to the commercial Pt/C material, but, having a lower ECSA, its specific activity (SA) is much higher than that of the reference material. Overall, the material displays higher MA and SA for ORR, compared to other porous or non-porous Pt-based nanomaterials from the literature.[59,60] At the same time, the sintered Pt NPs/Vulcan shows a very low MA, while the SA is closer to that of the reference commercial Pt/C. The peculiar performance of the composite porous Pt NPs/Vulcan expressed in terms of SA could arise from the well-defined morphology of the Pt crystallites.

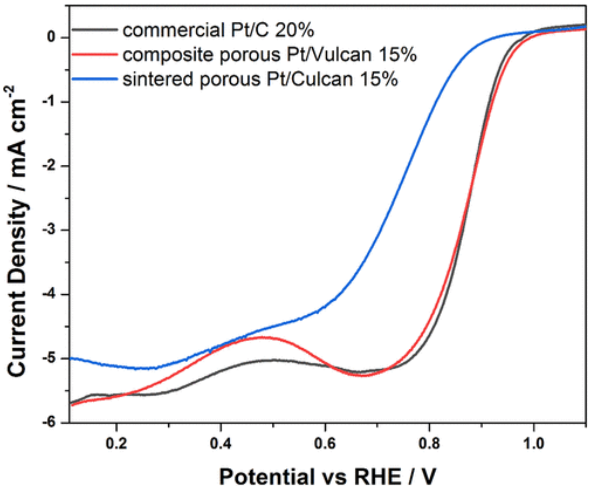

Figure 3.9 LSVs for commercial Pt/C (black), composite porous Pt/Vulcan material (red), and sintered porous Pt/Vulcan material (blue) registered at 10 mV s^{-1} from 0.1 to 1.1 V in 0.1 M HClO4 solution at 1600 rpm. The data is corrected for background currents, pH and ohmic losses.

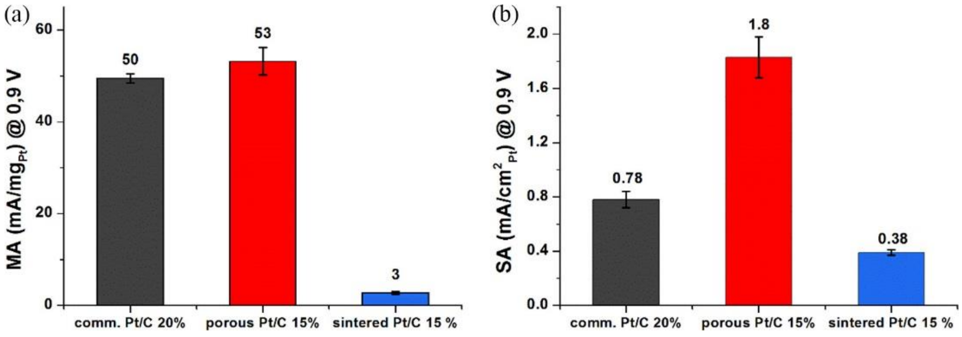

Figure 3.10. Comparison of MAs (a) and SAs (b) for ORR calculated from values at 0.9 V vs RHE in Fig. 3.8.

The three materials were tested also to investigate the Methanol Oxidation Reaction (MOR), to understand if a similar behavior would arise. A comparison with other works in the literature in this case is more difficult, because there is no standardized protocol for MOR activity characterization. In our case, the Pt/C nanocomposites were investigated via CV in an Ar saturated acidic electrolyte (0.1 M $HClO_4$) with the addition of 10% v/v of MeOH between 0.4 and 1.4 V vs RHE at a scan rate of 50 mV s^{-1} (Fig. 3.10). Catalyst loading was again fixed at 30 μg cm^{-2}. The MOR behavior of the three materials is in fact similar to the ORR case. Specific activities calculated on the forward scan for the non-porous materials (commercial Pt/C and composite sintered Pt/Vulcan) are comparable, while the porous nature and exposed facets in the composite porous Pt/Vulcan sample result in better performance of the electrocatalyst. Again, mass activities do not show a significant difference between the commercial Pt/C and composite porous Pt/Vulcan, pointing to a balancing effect between the lower ECSA and a higher specific activity. Where a comparison was possible with the literature (due to similar catalytic protocols), our material displays higher MAs and SAs toward MOR with respect to other porous and non-porous Pt-based nanomaterials.[61–63]

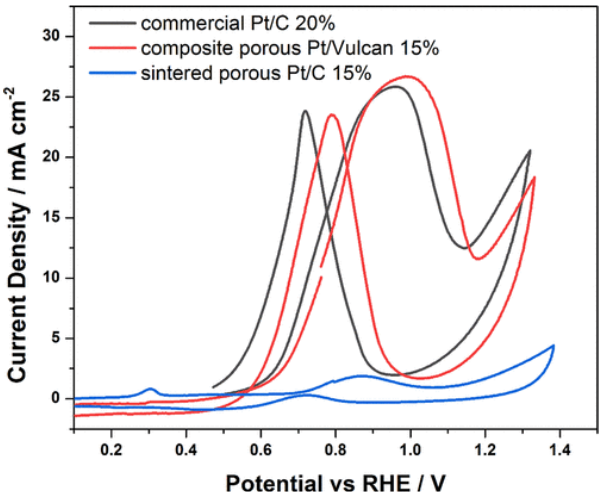

Figure 3.11 CVs of commercial Pt/C (black), composite porous Pt/Vulcan material (red), and sintered porous Pt/Vulcan material (blue) registered at 50 mV s^{-1} in a 10% vol MeOH sol. in 0.1 M $HClO_4$ from 0.1 to 1.5 V. Visualized potentials are corrected for pH and ohmic losses.

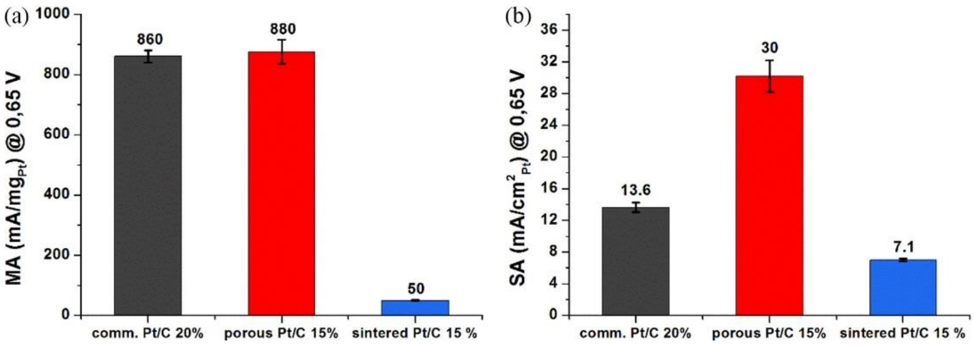

Figure 3.12 Comparison of MAs (a) and SAs (b) for MOR calculated from values at 0.65 V vs RHE in Fig. 3.10.

3.2.3 Conclusions

Porous multifaceted platinum nanoparticles (synthesized by the research group of prof. Lucia Pasquato) were characterized electrochemically in order to link their particular morphology with their catalytic activity. The synthesis was performed in the presence of OLAM and OLAC, crucial to achieve the complex architecture of the NPs promoted by the high temperature. The as-prepared NPs were very uniform in shape and highly monodisperse with a good grade of porosity. The growth mechanism displayed an unusual morphological transition of the NP shape never observed before. The resultant nanoparticles were deposited on Vulcan carbon and characterized electrochemically to understand their exposed facets and to quantify their ECSA. The porous Pt NPs showed lower surface areas than the commercial Pt NPs, however, revealed to be electrochemically active toward ORR and MOR with higher mass activity and specific activity than the controls (sintered Pt NPs and commercial Pt.NPs), highlighting the potential of highly structured and porous nanoparticles in electrocatalysis.

3.3 Cobalt@N-doped Carbon Nanocomposites for H_2O_2 Electrosynthesis

Hydrogen peroxide synthesis in small to large fuel cell setups could revolutionize many different fields. Not only H_2O_2 is interesting in industrial environments (from chemical synthesis to rocket fuel), but it could also be used, for example, to treat wastewaters while producing energy in rural contexts or poorer countries.[64] Working from previous knowledge obtained in the group,[8,34,65] Cobalt-carbon core shells were synthetized to be used as an electrocatalyst for ORR toward H_2O_2 production. A core shell structure was deemed to be the most interesting to achieve high efficiencies for the 2-electron pathway in acid electrolyte (were unprotected cobalt nanoparticles would be solubilized), and it was also highlighted that the choice of the carbon precursor is of great importance: depending on the carbon precursors and on the pyrolysis temperature, graphitic carbon shells with different texture, N doping concentrations and type of the N species (pyrrolic, pyridinic, etc.) are obtained. All these parameters have been reported of profoundly affecting both activity and selectivity of the final material.[66–68] The electrochemical characterization was primarily performed by the use of the Rotating Ring Disc Electrode (RRDE). The electrode implementation in a polymer membrane static flow electrolyzer setup was evaluated to understand how the material catalytic features such as current ranges and selectivity scale up from a classical three electrode system to a more realistic application-focused environment. Given H_2O_2 tendency to being further reduced on the electrode surface, the relationship between performance and electrode deposit protocol was also an objective of the present investigation, given its criticality for achieving suitable macroscopic porosity at the electrode interface.

3.3.1 Experimental Section

Materials. Cobalt acetate [$Co(ac)_2 \cdot 4 H_2O$], perchloric acid ($HClO_4$), and isopropyl alcohol (99.5 %) were purchased from Carlo Erba. Melamine, sulfuric acid (H_2SO_4, 98%) and Nafion® 117 solution were purchased from Sigma–Aldrich. All reagents were used as received. All experiments were conducted with milliQ water obtained by using a Direct-Q (Millipore) water purification system.

Synthesis of Co-NCNS-T. Cobalt acetate dihydrate and melamine were first mixed in 1:1 mass ratio in a few mL of water for half an hour and then dried at 90 °C for 2 h. The powder were transferred in an open alumina vessel and kept first under Ar flow for 1.5 h at 40 °C and then ramping at 3 °C/min to the final temperature (**T**) for 3 h. After cooling under Ar atmosphere, the material was dispersed in 1 M $HClO_4$ and subsequently stirred at 80 °C for 4 h. The acid-treated sample was filtered and washed with bi-distilled water. The acid leaching was repeated a second time and then the obtained black powder was dried under vacuum overnight and recovered. The samples were named Co-NCNSs-T, with T indicating the pyrolysis temperature (650, 800 and 900 °C).

Electrochemical Measurements. All the inks were prepared in a 3:1 H_2O iPrOH mixture with the addition of 5%(v/v) Nafion® 117 solution and catalyst concentration of 2.5 mg mL^{-1}. The dispersion concentration was fixed to 2.5 mg mL^{-1}. The ink was drop casted on the polished GC-RRDE in 5 µl drops till a loading of 127.5 µg cm^{-2} was reached for every experiment, unless otherwise stated, and dried under reduced pressure. In accordance with half-cell measurements, a further investigation of the different Co-based electrocatalysts was performed in a polymer membrane-exploiting static flow electrolyzer. The setup consisted of two separated compartments positioned in a vertical configuration and separated by a Proton-exchange Membrane (PEM, Nafion® 117, see Fig. 3.8).

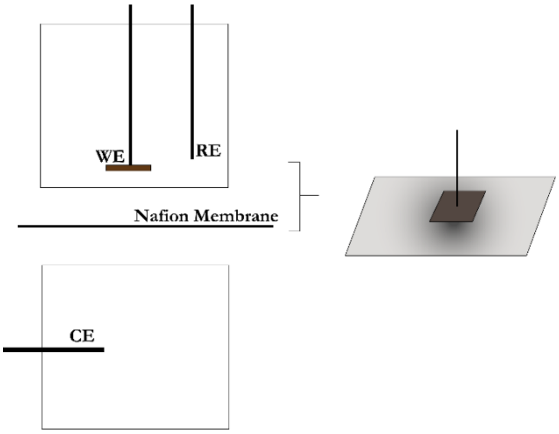

Figure 3.13 Schematic representation of the static flow eletrolyzer setup with side perspective of the orientation of the CP electrode with respect to the Nafion membrane.

The top compartment, i.e. the cathodic side, was characterized by a maximum volume of 50 mL of electrolyte, saturated with O_2. The reference and the working electrode are both introduced in the top compartment of the cell, while maintaining gas-tightness, taking care that the working electrode faced downward towards the membrane and counter electrode. A Pt wire counter electrode was placed in the anodic side bottom compartment. The maximum volume of this compartment is 120 mL of electrolyte. The catalytic material was deposited on Toray® Carbon Paper (CP, Toray Industries Inc.) with a 2 cm^2 geometric surface area at different loadings to assess the accordance of RRDE calculated selectivity in a scaled-up system. The ink was then dried in an air furnace at 60 °C. Both sides of the CP were used for deposition. To pinch in place the CP a steel threaded rod and cap (covered from the electrolyte by a hard plastic layer) were used. The CP was pinched in the center and the area covered by the plastic cap is approximately 0.25 cm^2 on each side that was excluded from the electrode geometrical surface area calculation. CAs were carried out to test the catalytic stability of the Co-NCNSs in the electrolyzer setup for 1.5 h and 3 h. After bulk electrolysis, the peroxide concentration in solution was estimated through permanganometric titration. Both for half-cell and electrolyzer CA measurements, electrode recycling tests were performed by changing the electrolyte solution to evaluate changes in activity and/or selectivity performances with time.

3.3.2 Results and Discussion

Synthesis and characterization. Pyrolysis of a cobalt derivative and melamine under controlled conditions of Ar flow, temperature resulted in a nanocomposite material showing a characteristic core-shell structure. After the pyrolysis, acid washing was used to remove the excess of metal present as exohedral metal NPs. The final material retained only the cobalt cores protected by a N-doped graphitic shell, resulting in the Cobalt@N-doped Carbon Nano-Shells (**Co-NCNS**). The absence of any extra-metallic species is critical to unequivocally assign electrocatalytic performance in core-shell systems avoiding any false conclusion arising from unaccounted presence of extra-metallic species [69]. Melamine was chosen as a carbon and nitrogen source due to its ability to form highly ordered C-N structures, such as that of graphitic carbon nitride (g-C_3N_4) [70]. The presence of a cobalt NP defines the final morphology and composition, as the metal acts as a catalytic site and template the polymerization of g-C_3N_4 from melamine, leading to the core-shell configuration. Melamine sublimation, followed by degradation, occurs during the heating stage, favouring the formation of graphitic N-doped carbon nanospheres enveloping cobalt nanoparticles. Three different composites were prepared by varying the pyrolysis temperature (650, 800 and 900 °C) affording respectively **Co-NCNS**-650, **Co-NCNS**-800, **Co-NCNS**-900. It is known that pyrolysis temperature largely affects the properties of the material, such as morphology, composition, porosity, conductivity, and consequently the catalytic performance [71–73].

TEM analysis shows that some graphitic structures are unable to protect the metal nanoparticle from the acid leaching step, leaving behind a material with the desired core-shell structure and a hollow graphitic matrix (Fig. 3.14a).

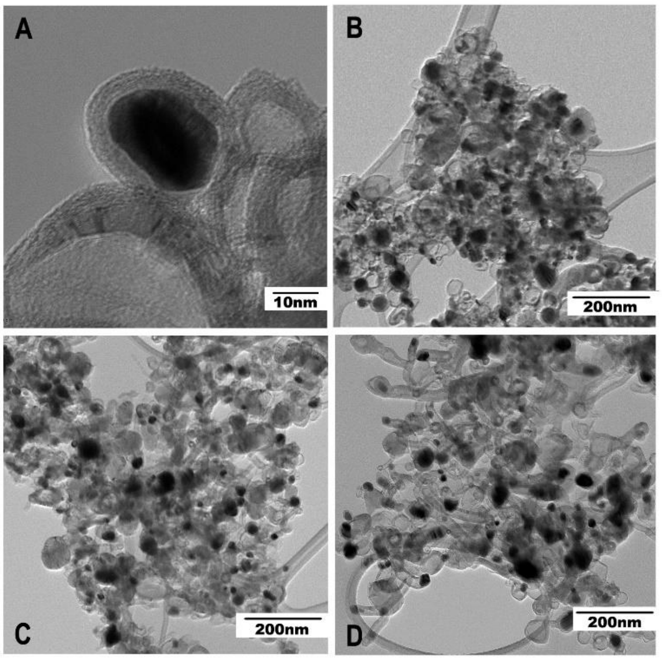

Figure 3.14 Typical morphology of Co-NCNS-800 visible in TEM images and low magnification images of (a) Co-NCNS-650 (b), Co-NCNS-800 (c) and Co-NCNS-900 (d).

Moreover, at 650 °C the preferred structure is a uniform N-doped Carbon Nano-Shell enveloping the metallic cobalt core (Fig. 3.14b). In contrast, higher pyrolysis temperatures (Fig. 3.14c,d) trigger to some extent the development of a carbon nanotube structure, with the Co nanoparticles located within the inner space of the nanotubes. Evidently a more severe thermal treatment allows the anisotropic catalytic growth of the carbon structure [74]. The distribution of the nanoparticle diameters could be estimated by analysis of TEM images (Fig. 3.15). All three materials show a broad distribution of particle size but, with increased pyrolysis temperature, the average particle size decreases. Thermogravimetric analysis (TGA, Fig. 3.16) shows similar characteristics throughout the Co-NCNs samples, with a stability to air until 350 °C and a residual weight of 10-15 % at 850 °C ascribed to the remaining inorganic component (mainly cobalt oxide), while ICP-OES analysis provided a cobalt loading in the range of 4-7% (w/w).

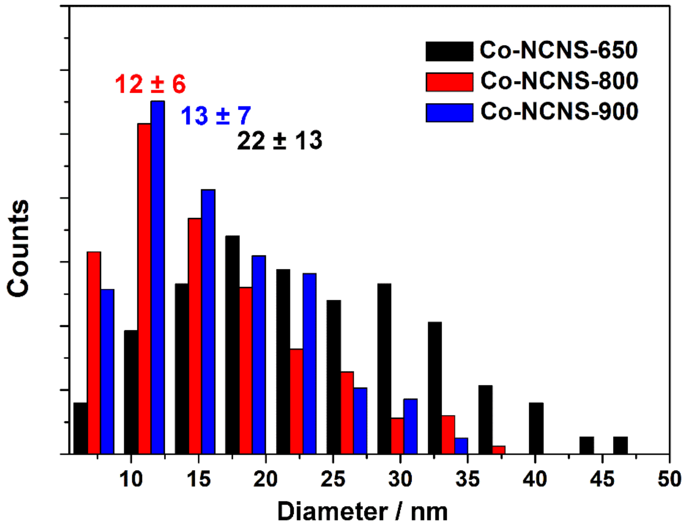

Figure 3.15 Cobalt NP cores' dimension distributions of Co-NCNS-650 (black), Co-NCNS-800 (red) and Co-NCNS-900 (blue). Sample population 300 nanoparticles each.

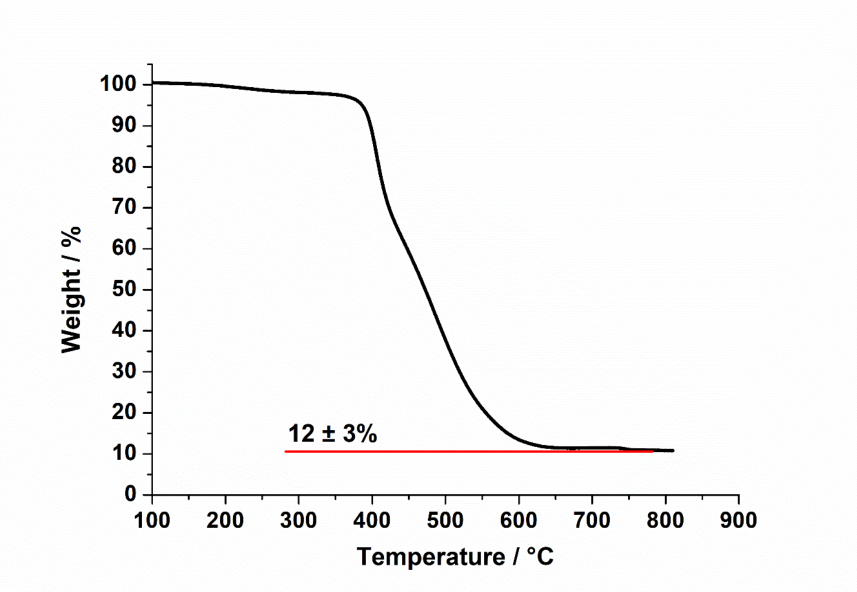

Figure 3.16 Thermogravimetric Analysis of Co-NCNS-800 with a scan speed of 20 °C/min in air. The remaining weight at 800 °C is given by the cobalt oxide that forms during the TGA.

The high degree of graphitization of the carbon shell is supported by Raman spectroscopy, that showed relatively narrow D and G peaks, typical of carbon material containing graphitic domains, after peak deconvolution (Figure 3.17), at 1320 and 1600 cm^{-1} respectively, in proportion to the higher pyrolysis temperatures, which is an indication of an increase of the graphitic character [75,76]. Moreover, the clear emergence of the double resonant peak (G') at ~ 2600 cm^{-1}, which is a signature of the graphitic sp^2 carbons [77], further supports the increasing graphitic nature with higher pyrolysis temperature. The correct deconvolution of the 1000-2000 cm^{-1} area was possible adding two more peaks (at 1150 and 1490 cm^{-1}), already observed in literature, and resulting from the excitation of the ν_1 and ν_3 bands of the transpolyacetylene segments at grain boundaries.[78]

Finally, the only XRD visible peaks are related to graphitic carbon and metallic cobalt (Fig. 3.18).

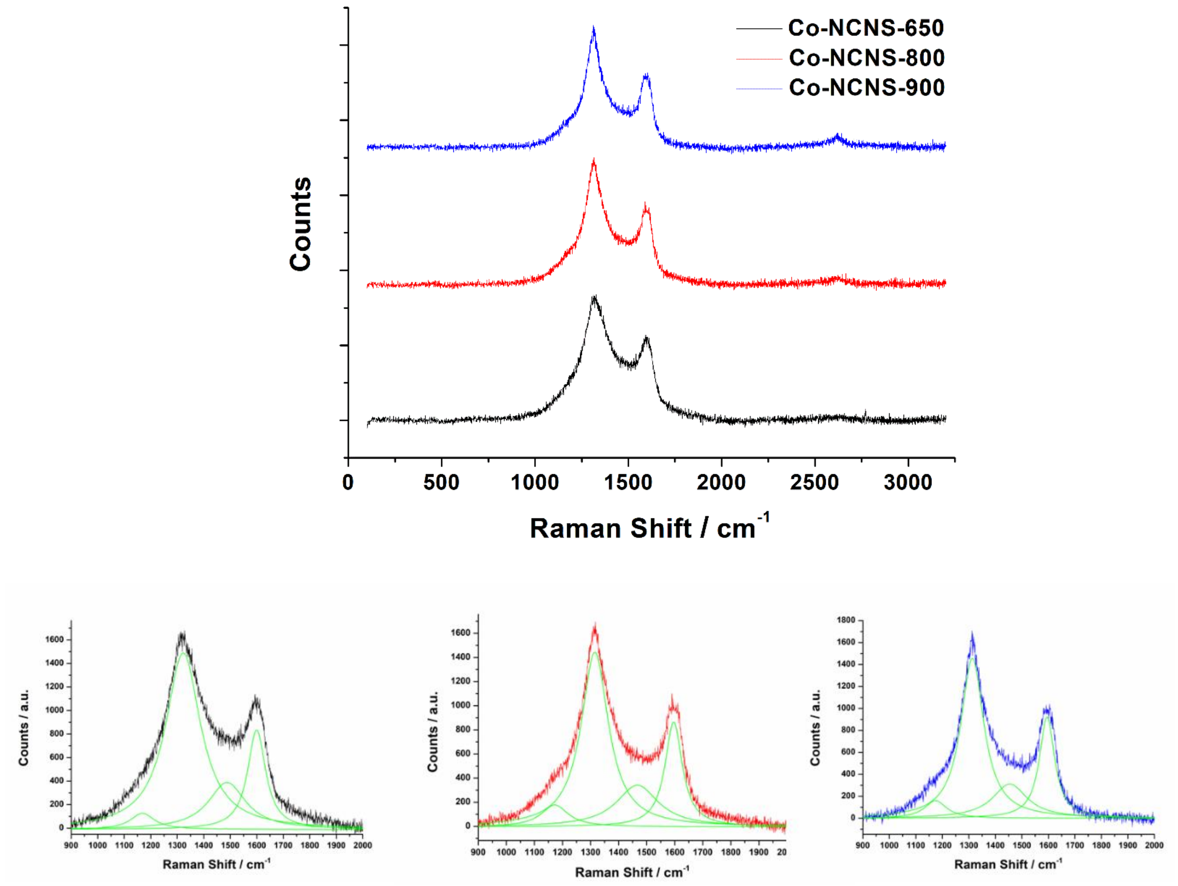

Figure 3.17 Raman spectra of Co-NCNS-650 (black), Co-NCNS-800 (red) and Co-NCNS-900 (blue). Corresponding deconvolutions are reported for the main peaks between 900 and 2000 cm^{-1}.

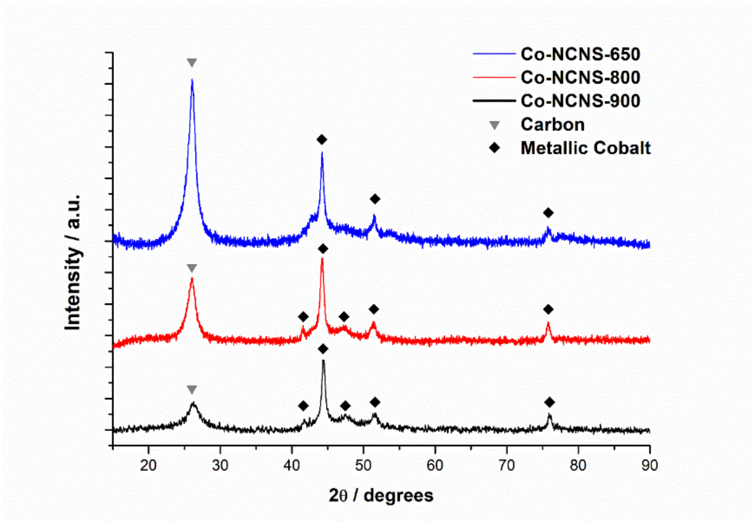

Figure 3.18 XRD analysis of Co-NCNSs with typical reflections of graphitic domains and of metallic cobalt lattice

XPS analysis provided the superficial composition of the three samples: apart from N and C, a significant percentage of O is also observed, presumably introduced in the graphitic layer during the washing step, due to the oxidizing character of $HClO_4$ (Tab. 3.4). Observation of low-intensity peaks attributed to Co species are presumably due to some thinner carbon shell which do not prevent the core cobalt to be detected by the XPS scan depth. As expected, the increase in pyrolysis temperature results in a progressive loss of both N and O content [71], leading to a higher C percentage, and this is also reflected in the observed lower ORR current density with the less doped CNSs (Fig. 3.21, Table 3.4).

Sample	*C / at%*	*N / at%*	*O / at%*	*Co / at%*
Co-NCNSs-650	86.52	5.79	7.05	0.64
Co-NCNSs-800	92.14	3.40	3.92	0.54
Co-NCNSs-900	94.46	2.69	2.47	0.38

Table 3.4 atomic ratio by XPS analysis of a) Co-NCNSs-650, b) Co-NCNSs-900, c) Co-NCNSs-800.

As previously reported, the N type distribution, in particular the $N_{pyrrolic}/N_{pyridinic}$ ratio, significantly affects the ORR selectivity, with the 2-electron pathway requiring optimum $N_{pyrrolic}/N_{pyridinic}$ [73]. Accordingly, in the present case we note that pyrrolic/pyridinic ratio increases in the order Co-NCNS-650 < Co-NCNSs-800 < Co-NCNSs-900 (Fig. 3.19, Tab. 3.5), and that the best H_2O_2 selectivity would be achieved with the Co-NCNSs-900 catalyst (see following discussion on electrochemistry). However, the trend in current density is the opposite, as anticipated in view of the progressive overall loss of the N and O dopants, which are typically associated, and thus proportional, to the catalytic active sites [79]. It is worth mentioning that even if Co is embedded within the carbon shells and therefore not directly available to the reactive environment, it may have an indirect role in the catalysis by means of electronic surface states modification of the superficial carbon, as proposed in several articles on core-shell electro-catalysts [34,69].

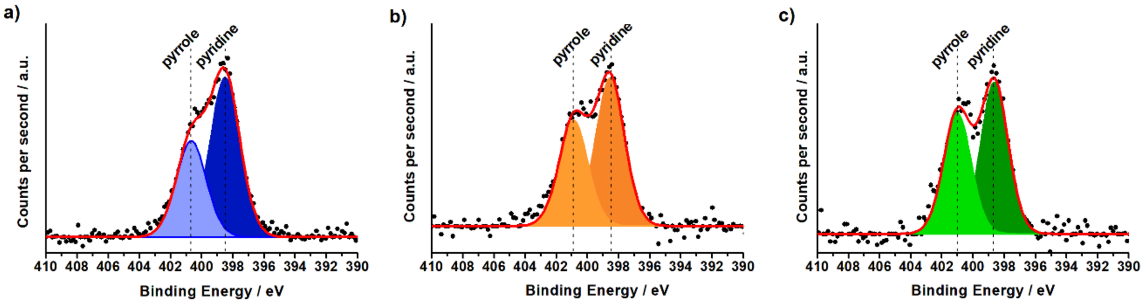

Figure 3.19 Deconvoluted N1s core level spectra of a) Co-NCNSs-650, b) Co-NCNSs-800, c) Co-NCNSs-900.

Samples	*Pyrrolic N=C at ~401 eV (%)*	*Pyridinic N=C at ~398 eV (%)*	*Pyrrolic N=C / Pyridinic N=C*
Co-NCNSs-650	37.7	62.3	0.61
Co-NCNSs-800	41.7	58.3	0.72
Co-NCNSs-900	44.4	55.6	0.80

Table 3.5 Atomic percentage of N1s components derived from fitting analysis.

ECSA and corresponding RFs shows fewer active sites surviving the higher temperature treatments (Fig. 3.20a, Tab. 3.6). The Brunauer–Emmett–Teller (BET) surface area confirms this tendency, decreasing with higher pyrolysis temperature, as the carbon shell tends to graphitize resulting in less porous carbon (Fig. 3.20b, Tab. 3.6) [80]. Hence, the isotherms are typical of mesoporous materials, showing a hysteresis loop at high nitrogen pressures. The pore diameter distributions show two maxima, around 3 and 100 nm (Fig. 3.20c), in which the molecular oxygen dissolved in the electrolyte can diffuse and react. Typical detrimental characteristics, such as micropores that could trap the hydrogen peroxide and favour its reduction to water [67,81], represent only a limited fraction of the pore makeup (Tab. 3.6).

	ECSA (cm^2)	*RF*	*SA$_{BET}$ (m^2 g^{-1})*	*Ext SA (m^2 g^{-1})*	*Cumulative Pore Volume (cm^3 g^{-1})*	*Micropore Volume (cm^3 g^{-1})*
Co-NCNS-650	2.64 ±0.06	13.4 ±0.3	173	137	0.65	0.016
Co-NCNS-800	2.09 ±0.06	10.6±0.3	164	132	0.58	0.025
Co-NCNS-900	1.22 ±0.06	6.2±0.1	132	108	0.51	0.015

Table 3.6 Calculated surface areas and pore volumes derived from BET and electrochemical analysis. ECSA values are calculated on a catalytic loading of 127.5 µg cm^{-2}.

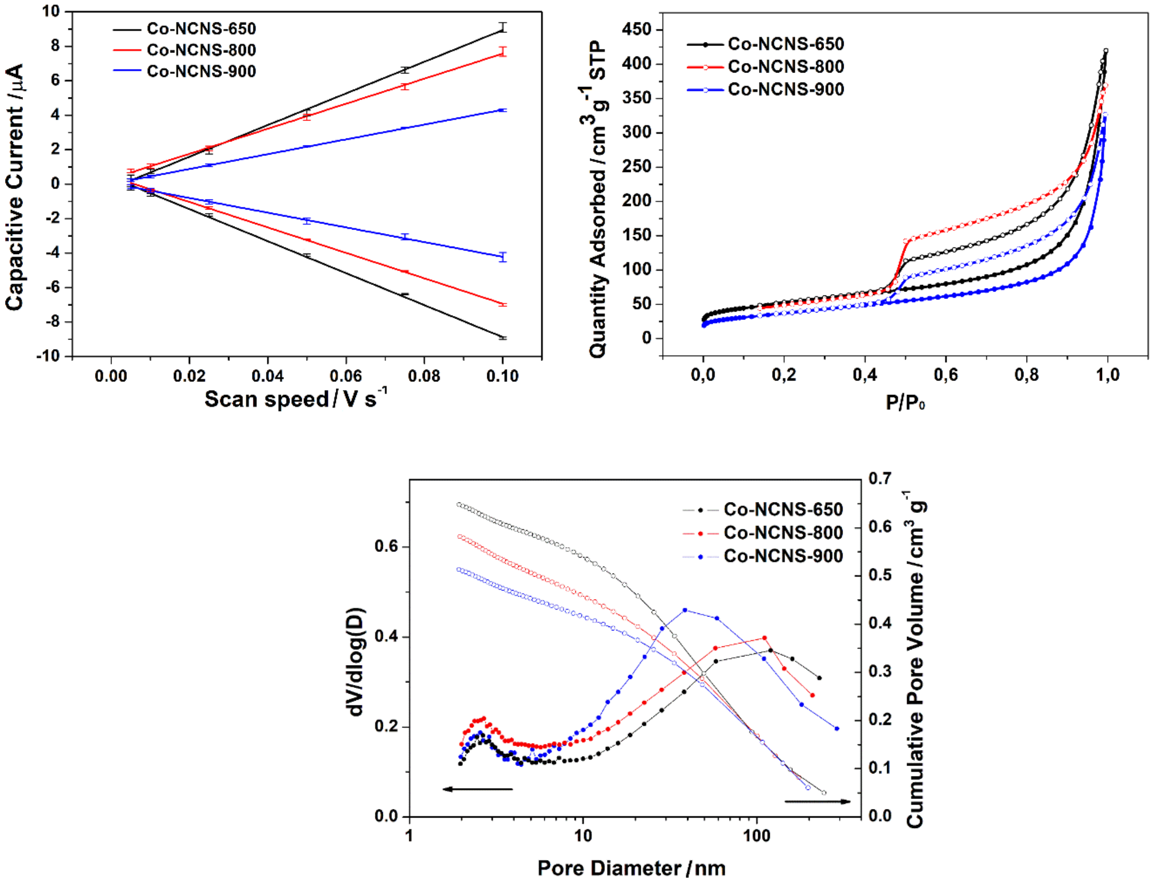

Figure 3.20 (a) ECSA calculations, (b) N_2 isotherms and (c) adsorption pore size distributions and cumulative pore volume for the three synthetized Co-NCNS materials.

ORR performances in half cell. ORR catalytic activities of the different Co-NCNS composites were investigated in relation to the pyrolysis temperature via LSV in acidic electrolyte (0.1 M H_2SO_4) between 0.9 and 0 V vs RHE at a scan rate of 5 mV s^{-1} (Fig. 3.21). The best catalyst loading to ensure good H_2O_2 selectivity and high current densities was determined to be 127.5 µg cm^{-2}, corresponding to a very low loading of ~6 μg_{Co} cm^{-2}, similar to state of the art catalyst loadings with precious metals in H_2O_2 generation [82].

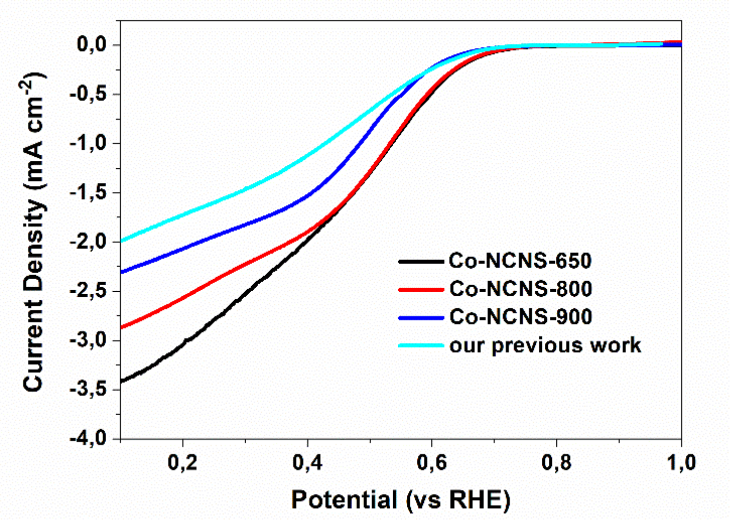

Figure 3.21 LSV obtained at 1600 rpm on different Co-NCNCSs compared to our previous work on cobalt core-shell systems [34].

The later onset shown by Co-NCNS-900 could be due to a lower porosity of the carbon shell (as underlined in BET and ECSA analysis) and different N-type species on the carbon surface [80]. Co-NCNSs-650, on the other hand, accounted for higher currents, presumably resulting from the higher N content, but low selectivity due to low graphitization of the material combined with the non-optimum N type distribution [8]. The above results suggested that an intermediate structure where all the chemical and structural features could be tailored for best activity and selectivity was hinged to the pyrolysis temperature. Hence, Co-NCNSs-800 was prepared to balance selectivity and throughput. The selectivity of the material was calculated from RRDE analysis and finally validated by the traditional permanganometric titration of the electrolyte. The selectivity toward the 2-electron pathway from RRDE analysis (Fig. 3.22) showed that Co-NCNS-900 and Co-NCNS-800 have higher selectivity toward H_2O_2 with a peak very close to 100% at very low overpotentials; on the other hand, Co-NCNS-650 displayed higher peak currents but with substantially lower selectivity at all potentials. At high currents, all materials tend to lose selectivity due to faster reduction kinetics (hydrogen peroxide to water) at the electrode surface [83,84].

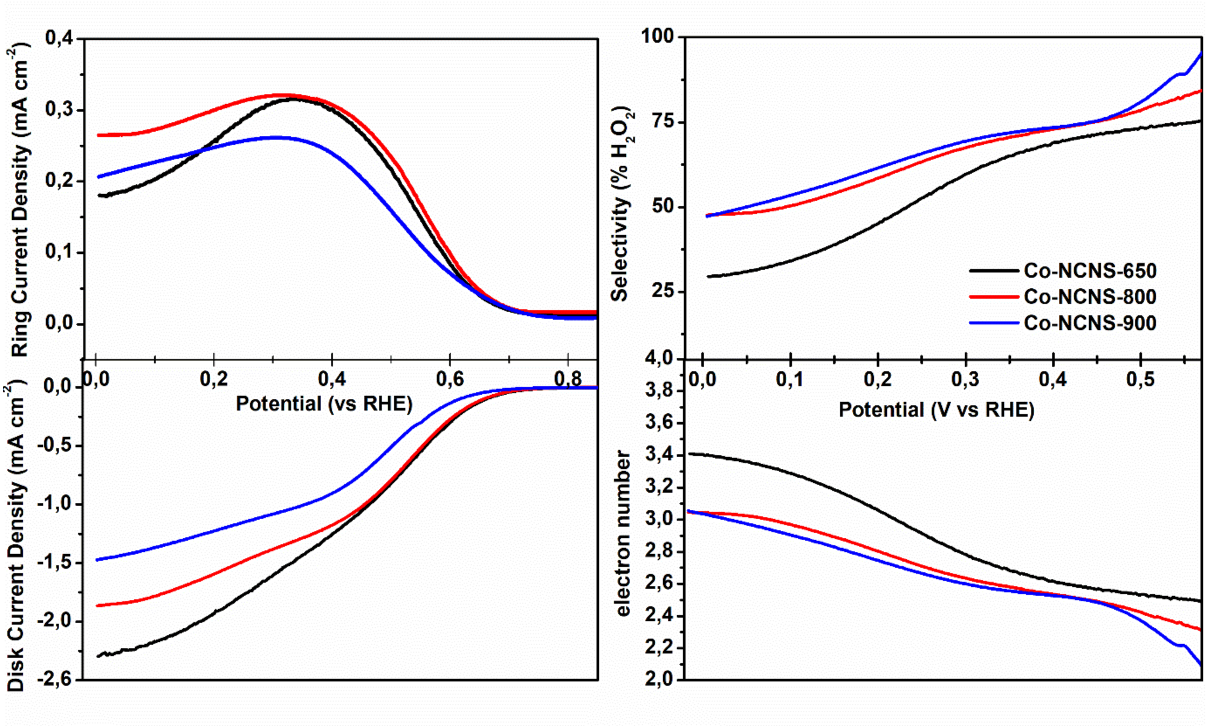

Figure 3.22 RRDE analysis on different Co-NCNS: Disk and Ring currents at 800 rpm (left) and calculated electron number and H_2O_2 selectivity (right).

CA tests in acidic electrolyte were employed to assess the catalytic stability of the materials. All Co-NCNS showed similar stabilities, with a retained activity higher than 95% after a 1 h test (Fig. 3.23). An Ion Coupled Plasma (ICP-OEP) analysis of the electrolyte after a CA test showed no traces of cobalt, excluding leaching of the cobalt core in solution. A possible deactivation route could be the reduction of catalytically active sites on the carbon surface or the loss of contact of the material on the GC interface. To further understand the surface modifications during catalysis, Co-NCNS-800 was subjected to a series of three CAs replacing the electrolyte between runs (Fig. 3.24). The material partial reactivation after electrolyte recycling suggests a convergence of concomitant causes: a partial deactivation of the catalyst that is reversed at the end of each CA and an irreversible reorganization or detachment of the nanoparticles, that has been confirmed both through ECSA and RRDE collection efficiency calculations before and after a 2 h CA run (Tab. 3.6). The increase in collection efficiency of the RRDE (toward the 25% stated by the manufacturer) reflects a plainer surface on the electrode, resulting in diminished turbulent flow at the GCE interface. The slight loss in electrochemically active surface area is consistent with this thesis, pointing to aggregation on the surface of the electrode or detachment of the material itself.

	Before CA	*After CA*
ECSA (cm^2)	3.4±0.1	3.2±0.3
N_c (%)	19±1	24±1

Table 3.6 Variation of Electrochemical Surface Area (ECSA) and collection efficiency (Nc) before and after a 1 h chronoamperometry on a GC-RRDE.

ORR performances in membrane-based electrolyzer. Electrolyzer performances have been evaluated through longer CAs (3 h) and electrolyte recycling tests to understand catalytic stability in a scaled-up environment and changes in selectivity after prolonged activity. Co-NCNS-800 deposited on a CP electrode shows excellent stability both after a 3 h CA (Fig. 3.23) and a 6h recycling test (Fig. 3.24). The permanganometric titration of the electrolyte at the end of each CA test (Tab. 3.7) showed a decrease in catalytic selectivity in time, probably due to accumulation of hydrogen peroxide that can be further reduced to water at the electrode surface.

Electrocatalyst	**Electrode loading (μg cm^{-2})**		
	175	250	500
	FEs (H_2O_2) % [vs. Electrolysis time (h)]		
Co-NCNS-800	94±4 [1.5, first cycle] 94±4 [1.5, second cycle] 86±3 [3.0, third cycle]	82±3 [1.5, first cycle] 79±2 [1.5, second cycle] 76±3 [3.0, third cycle]	75±1 [1.5, first cycle] 74±1 [1.5,second cycle] 75±2 [3.0, third cycle]
Co-NCNS-650	62±4 [1.5]	57±3 [3.0]	45±5 [1.5]

Table 3.7 Electrode loading effect on Co-NCNS-800 selectivity toward hydrogen peroxide during electrolyte recycling tests (FE, Faradaic Efficiency).

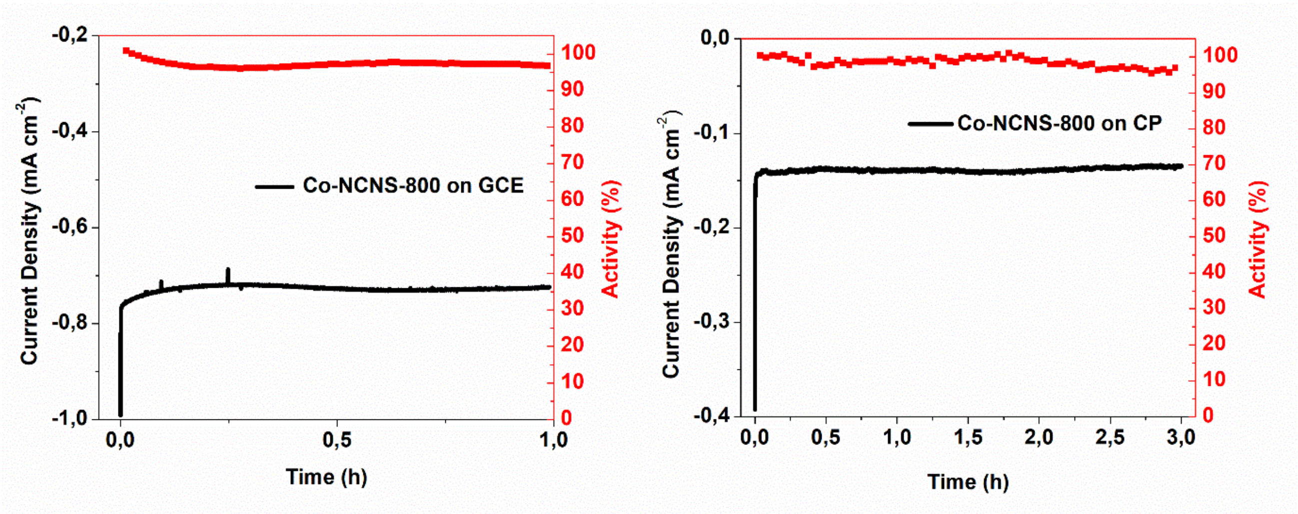

Figure 3.23 CA tests for Co-NCNS-800 on GC-RDE at 800 rpm (127.5 μg cm^{-2}, left) and on carbon paper (175 μg cm^{-2}, right) with calculated retained activity (as percentage).

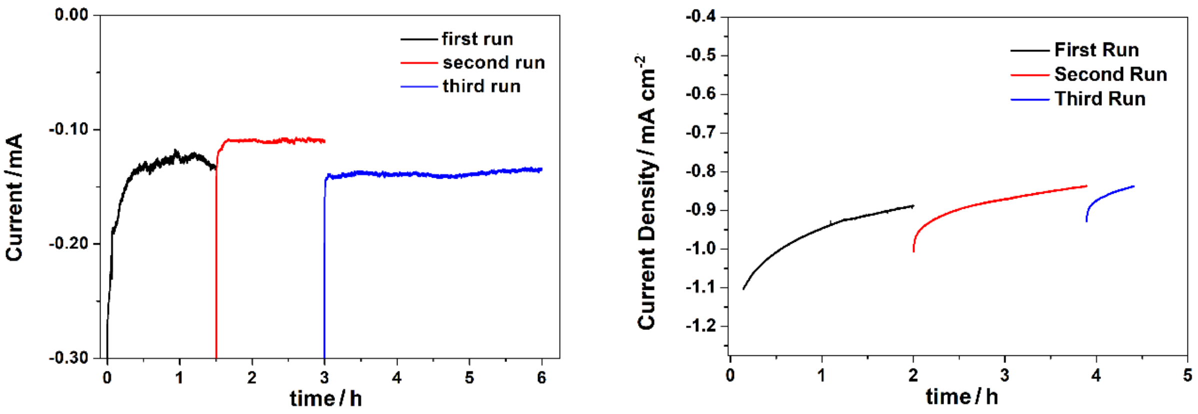

Figure 3.24 Electrolyte recycling tests for Co-NCNS-800 deposited on carbon paper (left) and on glassy carbon (right).

Electrolyzer performances can be also compared to RRDE results for different loadings of Co-NCNS-800. In general, the downward trend of selectivity with higher catalytic loading is similar in both sets of experiments and in accord with literature [85]. Interestingly, from a H_2O_2 selectivity point of view, Co-NCNS-800 performs systematically better in the electrolyzer setup (Fig. 3.25). The morphologic changes observed on the GCE substrate (Tab. 3.6) could explain better results obtained on CP. Given the flat surface of GC, CP textural properties could be of paramount importance in the stabilization of Co-NCNSs to avoid aggregation on the electrode surface.

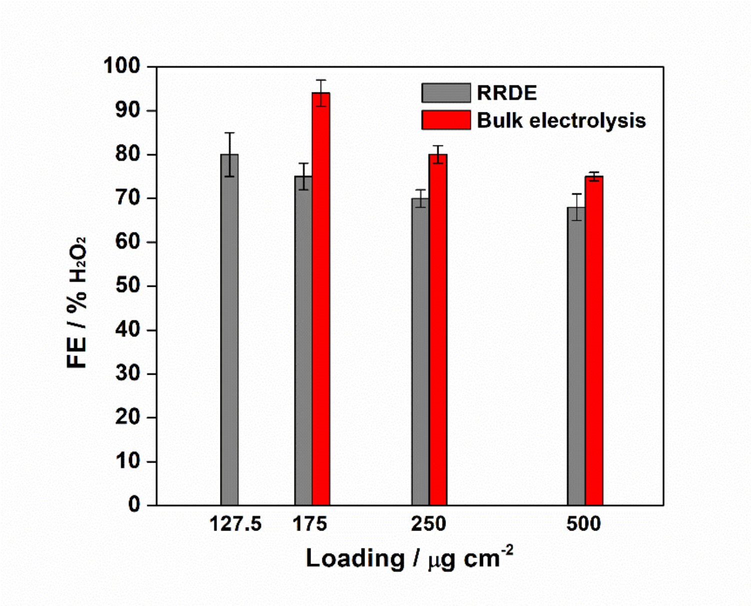

Figure 3.25 Data comparison between H_2O_2 FEs obtained from RRDE readings and permanganometric titrations on bulk electrolytic tests for Co-NCNS-800 at 0.5 V vs RHE with different catalytic loadings. FE referred to 127.5 µg cm^{-2} was reported only for RRDE setup cause of imperfect coverage of CP electrode with the same ink formulation.

3.3.3 Conclusions

ORR catalytic activities of three different Co-C composites (Co-NCNS-T) were firstly investigated in a half-cell setup in relation to the pyrolysis temperature via LSV in acidic electrolyte (0.1 M H_2SO_4). RRDE measurements showed the superior selectivity towards H_2O_2 by Co-NCNS-900 and Co-NCNS-800, almost close to completeness under optimized conditions. Co-NCNS-650 presents the highest currents, thanks to higher doping levels, but suffer from lower selectivity toward H_2O_2. Co-NCNS-800 was subjected to a deeper investigation by performing multiple CAs replacing the electrolyte between runs and parallel ECSA measurements; such combination of experiments allowed to attribute the loss of electrochemical performance to a physical surface electrode modification Co-NCNS-800 was further investigated by means of a superior setup based on an electrolyzer configuration, showing excellent stability both after a 3 h CA and a 6 h recycling test. The calculated bulk electrolysis (CA experiments) selectivity exhibited a slight decrease for longer operation times, probably due to accumulation of H_2O_2 that can be further reduced to water at the electrode surface. The results obtained herein pave the way to a rational design of flow – electrolyzer and MEA-based devices towards a real scale up for faster transfer to industrial utilization stage. Optimized working conditions related to the multi-layer structure of a PEM/MEA-structured electrolyzer and multilayer electrolyzer stacks represent one of the main targets to address H_2O_2 supply on industrial scale production by means of electrochemical methods.

3. References

(1) Nørskov, J. K.; Rossmeisl, J.; Logadottir, A.; Lindqvist, L.; Kitchin, J. R.; Bligaard, T.; Jónsson, H. Origin of the Overpotential for Oxygen Reduction at a Fuel-Cell Cathode. *Journal of Physical Chemistry B* **2004**, *108* (46), 17886–17892. https://doi.org/10.1021/JP047349J.

(2) Siahrostami, S.; Verdaguer-Casadevall, A.; Karamad, M.; Deiana, D.; Malacrida, P.; Wickman, B.; Escudero-Escribano, M.; Paoli, E. A.; Frydendal, R.; Hansen, T. W.; Chorkendorff, I.; Stephens, I. E. L.; Rossmeisl, J. Enabling Direct H2O2 Production through Rational Electrocatalyst Design. *Nature Materials 2013 12:12* **2013**, *12* (12), 1137–1143. https://doi.org/10.1038/nmat3795.

(3) Glasstone, S.; Hickling, A. The Hydrogen Peroxide Theory of Electrolytic Oxidation. *Chemical Reviews* **1939**, *25* (3), 407–441. https://doi.org/10.1021/CR60082A003.

(4) Nicoll, W. D.; Smith, A. F. Stability of Dilute Alkaline Solutions of Hydrogen Peroxide. *Industrial & Engineering Chemistry* **1955**, *47* (12), 2548–2554. https://doi.org/10.1021/ie50552a051.

(5) Siahrostami, S.; Verdaguer-Casadevall, A.; Karamad, M.; Deiana, D.; Malacrida, P.; Wickman, B.; Escudero-Escribano, M.; Paoli, E. A.; Frydendal, R.; Hansen, T. W.; Chorkendorff, I.; Stephens, I. E. L.; Rossmeisl, J. Enabling Direct H2O2 Production through Rational Electrocatalyst Design. *Nature Materials 2013 12:12* **2013**, *12* (12), 1137–1143. https://doi.org/10.1038/nmat3795.

(6) Liang, J.; Zheng, Y.; Chen, J.; Liu, J.; Hulicova-Jurcakova, D.; Jaroniec, M.; Qiao, S. Z. Facile Oxygen Reduction on a Three-Dimensionally Ordered Macroporous Graphitic C3N4/Carbon Composite Electrocatalyst. *Angewandte Chemie International Edition* **2012**, *51* (16), 3892–3896. https://doi.org/10.1002/ANIE.201107981.

(7) Liang, J.; Du, X.; Gibson, C.; Du, X. W.; Qiao, S. Z. N-Doped Graphene Natively Grown on Hierarchical Ordered Porous Carbon for Enhanced Oxygen Reduction. *Advanced Materials* **2013**, *25* (43), 6226–6231. https://doi.org/10.1002/ADMA.201302569.

(8) Iglesias, D.; Giuliani, A.; Melchionna, M.; Marchesan, S.; Criado, A.; Nasi, L.; Bevilacqua, M.; Tavagnacco, C.; Vizza, F.; Prato, M.; Fornasiero, P. N-Doped Graphitized Carbon Nanohorns as a Forefront Electrocatalyst in Highly Selective O2 Reduction to H2O2. *Chem* **2018**, *4* (1), 106–123. https://doi.org/10.1016/J.CHEMPR.2017.10.013.

(9) Kinumoto, T.; Inaba, M.; Nakayama, Y.; Ogata, K.; Umebayashi, R.; Tasaka, A.; Iriyama, Y.; Abe, T.; Ogumi, Z. Durability of Perfluorinated Ionomer Membrane against Hydrogen Peroxide. *Journal of Power Sources* **2006**, *158* (2), 1222–1228. https://doi.org/10.1016/J.JPOWSOUR.2005.10.043.

(10) Spanos, I.; Tesch, M. F.; Yu, M.; Tüysüz, H.; Zhang, J.; Feng, X.; Müllen, K.; Schlögl, R.; Mechler, A. K. Facile Protocol for Alkaline Electrolyte Purification and Its Influence on a Ni-Co Oxide Catalyst for the Oxygen Evolution Reaction. *ACS Catalysis* **2019**, *9* (9), 8165–8170. https://doi.org/10.1021/ACSCATAL.9B01940/SUPPL_FILE/CS9B01940_SI_001.PDF.

(11) Klaus, S.; Cai, Y.; Louie, M. W.; Trotochaud, L.; Bell, A. T. Effects of Fe Electrolyte Impurities on Ni(OH)2/NiOOH Structure and Oxygen Evolution Activity. *Journal of Physical Chemistry C* **2015**, *119* (13), 7243–7254. https://doi.org/10.1021/ACS.JPCC.5B00105/SUPPL_FILE/JP5B00105_SI_001.PDF.

(12) Melchionna, M.; Fornasiero, P.; Prato, M. The Rise of Hydrogen Peroxide as the Main Product by Metal-Free Catalysis in Oxygen Reductions. *Advanced Materials* **2019**, *31* (13), 1802920. https://doi.org/10.1002/ADMA.201802920.

(13) Okninski, A.; Kindracki, J.; Wolanski, P. Multidisciplinary Optimisation of Bipropellant Rocket Engines Using H2O2 as Oxidiser. *Aerospace Science and Technology* **2018**, *82–83*, 284–293. https://doi.org/10.1016/J.AST.2018.08.036.

(14) Pignatello, J. J.; Oliveros, E.; MacKay, A. Advanced Oxidation Processes for Organic Contaminant Destruction Based on the Fenton Reaction and Related Chemistry.

https://doi.org/10.1080/10643380500326564 **2007**, *36* (1), 1–84. https://doi.org/10.1080/10643380500326564.

(15) Hage, R.; Lienke, A. Applications of Transition-Metal Catalysts to Textile and Wood-Pulp Bleaching. *Angewandte Chemie International Edition* **2006**, *45* (2), 206–222. https://doi.org/10.1002/ANIE.200500525.

(16) Hou, H.; Zeng, X.; Zhang, X. Production of Hydrogen Peroxide by Photocatalytic Processes. *Angewandte Chemie International Edition* **2020**, *59* (40), 17356–17376. https://doi.org/10.1002/anie.201911609.

(17) Campos-Martin, J. M.; Blanco-Brieva, G.; Fierro, J. L. G. Hydrogen Peroxide Synthesis: An Outlook beyond the Anthraquinone Process. *Angewandte Chemie - International Edition*. John Wiley & Sons, Ltd October 27, 2006, pp 6962–6984. https://doi.org/10.1002/anie.200503779.

(18) Starz, K. A.; Auer, E.; Lehmann, T.; Zuber, R. Characteristics of Platinum-Based Electrocatalysts for Mobile PEMFC Applications. *Journal of Power Sources* **1999**, *84* (2), 167–172. https://doi.org/10.1016/S0378-7753(99)00333-X.

(19) Sasaki, K.; Shao, M.; Adzic, R. Dissolution and Stabilization of Platinum in Oxygen Cathodes. *Polymer Electrolyte Fuel Cell Durability* **2009**, 7–27. https://doi.org/10.1007/978-0-387-85536-3_2.

(20) Chen, Z.; Higgins, D.; Yu, A.; Zhang, L.; Zhang, J. A Review on Non-Precious Metal Electrocatalysts for PEM Fuel Cells. *Energy & Environmental Science* **2011**, *4* (9), 3167–3192. https://doi.org/10.1039/C0EE00558D.

(21) Ren, X.; Liu, B.; Liang, X.; Wang, Y.; Lv, Q.; Liu, A. Review—Current Progress of Non-Precious Metal for ORR Based Electrocatalysts Used for Fuel Cells. *Journal of The Electrochemical Society* **2021**, *168* (4), 044521. https://doi.org/10.1149/1945-7111/ABF695.

(22) Ren, Q.; Wang, H.; Lu, X.-F.; Tong, Y.-X.; Li, G.-R.; Ren, Q.; Wang, H.; Lu, X.; Tong, Y.; Li, G. Recent Progress on MOF-Derived Heteroatom-Doped Carbon-Based Electrocatalysts for Oxygen Reduction Reaction. *Advanced Science* **2018**, *5* (3), 1700515. https://doi.org/10.1002/ADVS.201700515.

(23) Zhang, J.; Zhang, J.; He, F.; Chen, Y.; Zhu, J.; Wang, D.; Mu, S.; Yang, H. Y. Defect and Doping Co-Engineered Non-Metal Nanocarbon ORR Electrocatalyst. *Nano-Micro Letters 2021 13:1* **2021**, *13* (1), 1–30. https://doi.org/10.1007/S40820-020-00579-Y.

(24) Wu, D.; Shen, X.; Pan, Y.; Yao, L.; Peng, Z. Platinum Alloy Catalysts for Oxygen Reduction Reaction: Advances, Challenges and Perspectives. *ChemNanoMat* **2020**, *6* (1), 32–41. https://doi.org/10.1002/CNMA.201900319.

(25) Gasteiger, H. A.; Kocha, S. S.; Sompalli, B.; Wagner, F. T. Activity Benchmarks and Requirements for Pt, Pt-Alloy, and Non-Pt Oxygen Reduction Catalysts for PEMFCs. *Applied Catalysis B: Environmental* **2005**, *56* (1-2 SPEC. ISS.), 9–35. https://doi.org/10.1016/J.APCATB.2004.06.021.

(26) Fellinger, T. P.; Hasché, F.; Strasser, P.; Antonietti, M. Mesoporous Nitrogen-Doped Carbon for the Electrocatalytic Synthesis of Hydrogen Peroxide. *J Am Chem Soc* **2012**, *134* (9), 4072–4075. https://doi.org/10.1021/ja300038p.

(27) Sun, Y.; Sinev, I.; Ju, W.; Bergmann, A.; Dresp, S.; Kühl, S.; Spöri, C.; Schmies, H.; Wang, H.; Bernsmeier, D.; Paul, B.; Schmack, R.; Kraehnert, R.; Roldan Cuenya, B.; Strasser, P. Efficient Electrochemical Hydrogen Peroxide Production from Molecular Oxygen on Nitrogen-Doped Mesoporous Carbon Catalysts. *ACS Catalysis* **2018**, *8* (4), 2844–2856. https://doi.org/10.1021/acscatal.7b03464.

(28) Liu, Y.; Quan, X.; Fan, X.; Wang, H.; Chen, S. High-Yield Electrosynthesis of Hydrogen Peroxide from Oxygen Reduction by Hierarchically Porous Carbon. *Angewandte Chemie International Edition* **2015**, *54* (23), 6837–6841. https://doi.org/10.1002/anie.201502396.

(29) Lu, Z.; Chen, G.; Siahrostami, S.; Chen, Z.; Liu, K.; Xie, J.; Liao, L.; Wu, T.; Lin, D.; Liu, Y.; Jaramillo, T. F.; Nørskov, J. K.; Cui, Y. High-Efficiency Oxygen Reduction to Hydrogen Peroxide Catalysed by Oxidized Carbon Materials. *Nature Catalysis* **2018**, *1* (2), 156–162. https://doi.org/10.1038/s41929-017-0017-x.

(30) Zhao, W. W.; Bothra, P.; Lu, Z.; Li, Y.; Mei, L. P.; Liu, K.; Zhao, Z.; Chen, G.; Back, S.; Siahrostami, S.; Kulkarni, A.; Nørskov, J. K.; Bajdich, M.; Cui, Y. Improved Oxygen Reduction

Reaction Activity of Nanostructured CoS2 through Electrochemical Tuning. *ACS Applied Energy Materials* **2019**, *2* (12), 8605–8614. https://doi.org/10.1021/acsaem.9b01527.

(31) Tang, C.; Jiao, Y.; Shi, B.; Liu, J.; Xie, Z.; Chen, X.; Zhang, Q.; Qiao, S. Coordination Tunes Selectivity: Two-Electron Oxygen Reduction on High-Loading Molybdenum Single-Atom Catalysts. *Angewandte Chemie International Edition* **2020**, *59* (23), 9171–9176. https://doi.org/10.1002/anie.202003842.

(32) Kralj, S.; Longobardo, F.; Iglesias, D.; Bevilacqua, M.; Tavagnacco, C.; Criado, A.; Delgado Jaen, J. J.; Makovec, D.; Marchesan, S.; Melchionna, M.; Prato, M.; Fornasiero, P. Ex-Solution Synthesis of Sub-5-Nm FeOx Nanoparticles on Mesoporous Hollow N,O-Doped Carbon Nanoshells for Electrocatalytic Oxygen Reduction. *ACS Applied Nano Materials* **2019**, *2* (10), 6092–6097. https://doi.org/10.1021/acsanm.9b01511.

(33) Antonin, V. S.; Parreira, L. S.; Aveiro, L. R.; Silva, F. L.; Valim, R. B.; Hammer, P.; Lanza, M. R. V.; Santos, M. C. W@Au Nanostructures Modifying Carbon as Materials for Hydrogen Peroxide Electrogeneration. *Electrochimica Acta* **2017**, *231*, 713–720. https://doi.org/10.1016/j.electacta.2017.01.192.

(34) Lenarda, A.; Bevilacqua, M.; Tavagnacco, C.; Nasi, L.; Criado, A.; Vizza, F.; Melchionna, M.; Prato, M.; Fornasiero, P. Selective Electrocatalytic H 2 O 2 Generation by Cobalt@N-Doped Graphitic Carbon Core–Shell Nanohybrids. *ChemSusChem* **2019**, *12* (8), 1664–1672. https://doi.org/10.1002/cssc.201900238.

(35) Li, W.; Bonakdarpour, A.; Gyenge, E.; Wilkinson, D. P. Drinking Water Purification by Electrosynthesis of Hydrogen Peroxide in a Power-Producing PEM Fuel Cell. *ChemSusChem* **2013**, *6* (11), 2137–2143. https://doi.org/10.1002/CSSC.201300225.

(36) Chen, Z.; Chen, S.; Siahrostami, S.; Chakthranont, P.; Hahn, C.; Nordlund, D.; Dimosthenis, S.; Nørskov, J. K.; Bao, Z.; Jaramillo, T. F. Development of a Reactor with Carbon Catalysts for Modular-Scale, Low-Cost Electrochemical Generation of H_2O_2. *Reaction Chemistry & Engineering* **2017**, *2* (2), 239–245. https://doi.org/10.1039/C6RE00195E.

(37) Yang, H. Platinum-Based Electrocatalysts with Core–Shell Nanostructures. *Angewandte Chemie International Edition* **2011**, *50* (12), 2674–2676. https://doi.org/10.1002/ANIE.201005868.

(38) Zhu, E.; Xue, W.; Wang, S.; Yan, X.; Zhou, J.; Liu, Y.; Cai, J.; Liu, E.; Jia, Q.; Duan, X.; Li, Y.; Heinz, H.; Huang, Y. Enhancement of Oxygen Reduction Reaction Activity by Grain Boundaries in Platinum Nanostructures. *Nano Research 2020 13:12* **2020**, *13* (12), 3310–3314. https://doi.org/10.1007/S12274-020-3007-2.

(39) Wang, L.; Holewinski, A.; Wang, C. Prospects of Platinum-Based Nanostructures for the Electrocatalytic Reduction of Oxygen. *ACS Catalysis* **2018**, *8* (10), 9388–9398. https://doi.org/10.1021/ACSCATAL.8B02906/ASSET/IMAGES/MEDIUM/CS-2018-02906Y_0007.GIF.

(40) Cargnello, M.; Doan-Nguyen, V. V. T.; Gordon, T. R.; Diaz, R. E.; Stach, E. A.; Gorte, R. J.; Fornasiero, P.; Murray, C. B. Control of Metal Nanocrystal Size Reveals Metal-Support Interface Role for Ceria Catalysts. *Science (1979)* **2013**, *341* (6147), 771–773. https://doi.org/10.1126/SCIENCE.1240148/SUPPL_FILE/PAPV2.PDF.

(41) Arán-Ais, R. M.; Vidal-Iglesias, F. J.; Solla-Gullón, J.; Herrero, E.; Feliu, J. M. Electrochemical Characterization of Clean Shape-Controlled Pt Nanoparticles Prepared in Presence of Oleylamine/Oleic Acid. *Electroanalysis* **2015**, *27* (4), 945–956. https://doi.org/10.1002/ELAN.201400619.

(42) Shinozaki, K.; Zack, J. W.; Richards, R. M.; Pivovar, B. S.; Kocha, S. S. Oxygen Reduction Reaction Measurements on Platinum Electrocatalysts Utilizing Rotating Disk Electrode Technique: I. Impact of Impurities, Measurement Protocols and Applied Corrections. *Journal of The Electrochemical Society* **2015**, *162* (10), F1144. https://doi.org/10.1149/2.1071509JES.

(43) Shinozaki, K.; Zack, J. W.; Pylypenko, S.; Pivovar, B. S.; Kocha, S. S. Oxygen Reduction Reaction Measurements on Platinum Electrocatalysts Utilizing Rotating Disk Electrode Technique: II. Influence of Ink Formulation, Catalyst Layer Uniformity and Thickness. *Journal of The Electrochemical Society* **2015**, *162* (12), F1384. https://doi.org/10.1149/2.0551512JES.

(44) Rodes, A.; el Achi, K.; Zamakhchari, M. A.; Clavilier, J. Hydrogen Probing of Step and Terrace Sites on Pt(S)-[n(111) × (100)]. *Journal of Electroanalytical Chemistry and Interfacial Electrochemistry* **1990**, *284* (1), 245–253. https://doi.org/10.1016/0022-0728(90)87077-W.

(45) Rudi, S.; Cui, C.; Gan, L.; Strasser, P. Comparative Study of the Electrocatalytically Active Surface Areas (ECSAs) of Pt Alloy Nanoparticles Evaluated by H Upd and CO-Stripping Voltammetry. *Electrocatalysis 2014 5:4* **2014**, *5* (4), 408–418. https://doi.org/10.1007/S12678-014-0205-2.

(46) Teng, X.; Liang, X.; Maksimuk, S.; Yang, H. Synthesis of Porous Platinum Nanoparticles. *Small* **2006**, *2* (2), 249–253. https://doi.org/10.1002/SMLL.200500244.

(47) Teng, X.; Yang, H. Synthesis of Platinum Multipeds: An Induced Anisotropic Growth. *Nano Letters* **2005**, *5* (5), 885–891. https://doi.org/10.1021/NL0503072/ASSET/IMAGES/LARGE/NL0503072F00008.JPEG.

(48) Jiang, B.; Li, C.; Malgras, V.; Imura, M.; Tominaka, S.; Yamauchi, Y. Mesoporous Pt Nanospheres with Designed Pore Surface as Highly Active Electrocatalyst. *Chemical Science* **2016**, *7* (2), 1575–1581. https://doi.org/10.1039/C5SC03779D.

(49) Pasricha, R.; Bala, T.; Biradar, A. v.; Umbarkar, S.; Sastry, M. Synthesis of Catalytically Active Porous Platinum Nanoparticles by Transmetallation Reaction and Proposition of the Mechanism. *Small* **2009**, *5* (12), 1467–1473. https://doi.org/10.1002/SMLL.200801863.

(50) Wang, S.; Kuai, L.; Huang, Y.; Yu, X.; Liu, Y.; Li, W.; Chen, L.; Geng, B. A Highly Efficient, Clean-Surface, Porous Platinum Electrocatalyst and the Inhibition Effect of Surfactants on Catalytic Activity. *Chemistry – A European Journal* **2013**, *19* (1), 240–248. https://doi.org/10.1002/CHEM.201203398.

(51) Kang, Y.; Ye, X.; Murray, C. B. Size- and Shape-Selective Synthesis of Metal Nanocrystals and Nanowires Using CO as a Reducing Agent. *Angewandte Chemie International Edition* **2010**, *49* (35), 6156–6159. https://doi.org/10.1002/ANIE.201003383.

(52) Wen, X.; Lerch, S.; Wang, Z.; Aboudiab, B.; Tehrani-Bagha, A. R.; Olsson, E.; Moth-Poulsen, K. Synthesis of Palladium Nanodendrites Using a Mixture of Cationic and Anionic Surfactants. *Langmuir* **2020**, *36* (7), 1745–1753. https://doi.org/10.1021/ACS.LANGMUIR.9B03804/ASSET/IMAGES/LARGE/LA9B03804_0007.JPEG.

(53) Mourdikoudis, S.; Montes-García, V.; Rodal-Cedeira, S.; Winckelmans, N.; Pérez-Juste, I.; Wu, H.; Bals, S.; Pérez-Juste, J.; Pastoriza-Santos, I. Highly Porous Palladium Nanodendrites: Wet-Chemical Synthesis, Electron Tomography and Catalytic Activity. *Dalton Transactions* **2019**, *48* (11), 3758–3767. https://doi.org/10.1039/C9DT00107G.

(54) Gao, Q.; Gao, M. R.; Liu, J. W.; Chen, M. Y.; Cui, C. H.; Li, H. H.; Yu, S. H. One-Pot Synthesis of Branched Palladium Nanodendrites with Superior Electrocatalytic Performance. *Nanoscale* **2013**, *5* (8), 3202–3207. https://doi.org/10.1039/C2NR33345G.

(55) Wang, L.; Yamauchi, Y. Facile Synthesis of Three-Dimensional Dendritic Platinum Nanoelectrocatalyst. *Chemistry of Materials* **2009**, *21* (15), 3562–3569. https://doi.org/10.1021/CM901161G/ASSET/IMAGES/LARGE/CM-2009-01161G_0009.JPEG.

(56) Song, Y.; Yang, Y.; Medforth, C. J.; Pereira, E.; Singh, A. K.; Xu, H.; Jiang, Y.; Brinker, C. J.; van Swol, F.; Shelnutt, J. A. Controlled Synthesis of 2-D and 3-D Dendritic Platinum Nanostructures. *J Am Chem Soc* **2004**, *126* (2), 635–645. https://doi.org/10.1021/JA037474T/SUPPL_FILE/JA037474TSI20031104_074624.PDF.

(57) Diaz-Morales, O.; Hersbach, T. J. P.; Badan, C.; Garcia, A. C.; Koper, M. T. M. Hydrogen Adsorption on Nano-Structured Platinum Electrodes. *Faraday Discussions* **2018**, *210* (0), 301–315. https://doi.org/10.1039/C8FD00062J.

(58) Angerstein-Kozlowska, H.; Conway, B. E.; Sharp, W. B. A. The Real Condition of Electrochemically Oxidized Platinum Surfaces: Part I. Resolution of Component Processes. *Journal of Electroanalytical Chemistry and Interfacial Electrochemistry* **1973**, *43* (1), 9–36. https://doi.org/10.1016/S0022-0728(73)80307-9.

(59) Shui, J. L.; Chen, C.; Li, J. C. M. Evolution of Nanoporous Pt–Fe Alloy Nanowires by Dealloying and Their Catalytic Property for Oxygen Reduction Reaction. *Advanced Functional Materials* **2011**, *21* (17), 3357–3362. https://doi.org/10.1002/ADFM.201100723.

(60) Xia, B. Y.; Wu, H. bin; Wang, X.; Lou, X. W. Highly Concave Platinum Nanoframes with High-Index Facets and Enhanced Electrocatalytic Properties. *Angewandte Chemie International Edition* **2013**, *52* (47), 12337–12340. https://doi.org/10.1002/ANIE.201307518.

(61) Wang, S.; Kuai, L.; Huang, Y.; Yu, X.; Liu, Y.; Li, W.; Chen, L.; Geng, B. A Highly Efficient, Clean-Surface, Porous Platinum Electrocatalyst and the Inhibition Effect of Surfactants on Catalytic Activity. *Chemistry – A European Journal* **2013**, *19* (1), 240–248. https://doi.org/10.1002/CHEM.201203398.

(62) Koo, J. H.; Kumar, A.; Lee, S.; Jin, X.; Jeong, H.; Kim, J.; Lee, I. S. Pore-Engineered Silica Nanoreactors for Chemical Interaction-Guided Confined Synthesis of Porous Platinum Nanodendrites. *Chemistry of Materials* **2018**, *30* (9), 3010–3018. https://doi.org/10.1021/ACS.CHEMMATER.8B00628/ASSET/IMAGES/LARGE/CM-2018-00628U_0007.JPEG.

(63) Lai, J.; Niu, W.; Qi, W.; Zhao, J.; Li, S.; Gao, W.; Luque, R.; Xu, G. A Platinum Highly Concave Cube with One Leg on Each Vertex as an Advanced Nanocatalyst for Electrocatalytic Applications. *ChemCatChem* **2015**, *7* (7), 1064–1069. https://doi.org/10.1002/CCTC.201403042.

(64) Arends, J. B. A.; van Denhouwe, S.; Verstraete, W.; Boon, N.; Rabaey, K. Enhanced Disinfection of Wastewater by Combining Wetland Treatment with Bioelectrochemical H2O2 Production. *Bioresource Technology* **2014**, *155*, 352–358. https://doi.org/10.1016/J.BIORTECH.2013.12.058.

(65) Zhang, Y.; Melchionna, M.; Medved, M.; Błoński, P.; Steklý, T.; Bakandritsos, A.; Kment, Š.; Zbořil, R.; Otyepka, M.; Fornaserio, P.; Naldoni, A. Enhanced On-Site Hydrogen Peroxide Electrosynthesis by a Selectively Carboxylated N-Doped Graphene Catalyst. *ChemCatChem* **2021**, *13* (20), 4372–4383. https://doi.org/10.1002/CCTC.202100805.

(66) Kundu, S.; Nagaiah, T. C.; Xia, W.; Wang, Y.; van Dommele, S.; Bitter, J. H.; Santa, M.; Grundmeier, G.; Bron, M.; Schuhmann, W.; Muhler, M. Electrocatalytic Activity and Stability of Nitrogen-Containing Carbon Nanotubes in the Oxygen Reduction Reaction. *Journal of Physical Chemistry C* **2009**, *113* (32), 14302–14310. https://doi.org/10.1021/jp811320d.

(67) He, W.; Jiang, C.; Wang, J.; Lu, L. High-Rate Oxygen Electroreduction over Graphitic-N Species Exposed on 3D Hierarchically Porous Nitrogen-Doped Carbons. *Angewandte Chemie - International Edition* **2014**, *53* (36), 9503–9507. https://doi.org/10.1002/anie.201404333.

(68) Tuci, G.; Zafferoni, C.; D'Ambrosio, P.; Caporali, S.; Ceppatelli, M.; Rossin, A.; Tsoufis, T.; Innocenti, M.; Giambastiani, G. Tailoring Carbon Nanotube N-Dopants While Designing Metal-Free Electrocatalysts for the Oxygen Reduction Reaction in Alkaline Medium. *ACS Catalysis* **2013**, *3* (9), 2108–2111. https://doi.org/10.1021/cs400379h.

(69) Melchionna, M.; Fornasiero, P.; Prato, M. Into the Carbon: A Matter of Core and Shell in Advanced Electrocatalysis. *APL Materials* **2020**, *8* (2), 020905. https://doi.org/10.1063/1.5134466.

(70) Thomas, A.; Fischer, A.; Goettmann, F.; Antonietti, M.; Müller, J. O.; Schlögl, R.; Carlsson, J. M. Graphitic Carbon Nitride Materials: Variation of Structure and Morphology and Their Use as Metal-Free Catalysts. *Journal of Materials Chemistry* **2008**, *18* (41), 4893–4908. https://doi.org/10.1039/b800274f.

(71) Koós, A. A.; Murdock, A. T.; Nemes-Incze, P.; Nicholls, R. J.; Pollard, A. J.; Spencer, S. J.; Shard, A. G.; Roy, D.; Biró, L. P.; Grobert, N. Effects of Temperature and Ammonia Flow Rate on the Chemical Vapour Deposition Growth of Nitrogen-Doped Graphene. *Physical Chemistry Chemical Physics* **2014**, *16* (36), 19446–19452. https://doi.org/10.1039/c4cp02132k.

(72) Yu, H.; Shang, L.; Bian, T.; Shi, R.; Waterhouse, G. I. N.; Zhao, Y.; Zhou, C.; Wu, L. Z.; Tung, C. H.; Zhang, T. Nitrogen-Doped Porous Carbon Nanosheets Templated from g-C3N4as Metal-Free Electrocatalysts for Efficient Oxygen Reduction Reaction. *Advanced Materials* **2016**, *28* (25), 5080–5086. https://doi.org/10.1002/adma.201600398.

(73) Iglesias, D.; Giuliani, A.; Melchionna, M.; Marchesan, S.; Criado, A.; Nasi, L.; Bevilacqua, M.; Tavagnacco, C.; Vizza, F.; Prato, M.; Fornasiero, P. N-Doped Graphitized Carbon Nanohorns as a Forefront Electrocatalyst in Highly Selective O2 Reduction to H2O2. *Chem* **2018**, *4* (1), 106–123. https://doi.org/10.1016/j.chempr.2017.10.013.

(74) Iglesias, D.; Melchionna, M. Enter the Tubes: Carbon Nanotube Endohedral Catalysis. *Catalysts* **2019**, *9* (2), 128. https://doi.org/10.3390/catal9020128.

(75) Ferrari, A.; Robertson, J. Interpretation of Raman Spectra of Disordered and Amorphous Carbon. *Physical Review B - Condensed Matter and Materials Physics* **2000**, *61* (20), 14095–14107. https://doi.org/10.1103/PhysRevB.61.14095.

(76) Ferrari, A. C.; Robertson, J. Raman Spectroscopy of Amorphous, Nanostructured, Diamond–like Carbon, and Nanodiamond. *Philosophical Transactions of the Royal Society of London. Series A: Mathematical, Physical and Engineering Sciences* **2004**, *362* (1824), 2477–2512. https://doi.org/10.1098/rsta.2004.1452.

(77) Dresselhaus, M. S.; Jorio, A.; Hofmann, M.; Dresselhaus, G.; Saito, R. Perspectives on Carbon Nanotubes and Graphene Raman Spectroscopy. *Nano Letters*. American Chemical Society March 10, 2010, pp 751–758. https://doi.org/10.1021/nl904286r.

(78) Ferrari, A. C.; Robertson, C. Origin of the 1150-cm^{-1} Raman mode in nanocrystalline diamond. *Physical Review B* **2001**, *63*, 121405(R). https://doi.org/10.1103/PhysRevB.63.121405.

(79) Melchionna, M.; Fornasiero, P.; Prato, M. The Rise of Hydrogen Peroxide as the Main Product by Metal-Free Catalysis in Oxygen Reductions. *Advanced Materials* **2019**, *31* (13), 1802920. https://doi.org/10.1002/adma.201802920.

(80) Zhou, Z.; Liu, T.; Khan, A. U.; Liu, G. Controlling the Physical and Electrochemical Properties of Block Copolymer-Based Porous Carbon Fibers by Pyrolysis Temperature. *Molecular Systems Design and Engineering* **2020**, *5* (1), 153–165. https://doi.org/10.1039/c9me00066f.

(81) Liang, J.; Du, X.; Gibson, C.; Du, X. W.; Qiao, S. Z. N-Doped Graphene Natively Grown on Hierarchical Ordered Porous Carbon for Enhanced Oxygen Reduction. *Advanced Materials* **2013**, *25* (43), 6226–6231. https://doi.org/10.1002/adma.201302569.

(82) Shen, R.; Chen, W.; Peng, Q.; Lu, S.; Zheng, L.; Cao, X.; Wang, Y.; Zhu, W.; Zhang, J.; Zhuang, Z.; Chen, C.; Wang, D.; Li, Y. High-Concentration Single Atomic Pt Sites on Hollow CuSx for Selective O2 Reduction to H2O2 in Acid Solution. *Chem* **2019**, *5* (8), 2099–2110. https://doi.org/10.1016/J.CHEMPR.2019.04.024.

(83) Kozawa, A.; Zilionis, V. E.; Brodd, R. J. Oxygen and Hydrogen Peroxide Reduction at a Ferric Phthalocyanine-Catalyzed Graphite Electrode. *Journal of The Electrochemical Society* **1970**, *117* (12), 1470. https://doi.org/10.1149/1.2407354.

(84) Appleby, A. J. Electrocatalysis of Aqueous Dioxygen Reduction. *Journal of Electroanalytical Chemistry*. Elsevier October 15, 1993, pp 117–179. https://doi.org/10.1016/0022-0728(93)80378-U.

(85) Biddinger, E. J.; Deak, D. von; Singh, D.; Marsh, H.; Tan, B.; Knapke, D. S.; Ozkan, U. S. Examination of Catalyst Loading Effects on the Selectivity of CNx and Pt/VC ORR Catalysts Using RRDE. *Journal of The Electrochemical Society* **2011**, *158* (4), B402. https://doi.org/10.1149/1.3552944.

4. The Nitrogen Reduction Reaction

4.1 Introduction

The Nitrogen Reduction Reaction (NRR) is one of the hottest research topics in today's electrocatalysis landscape. Molecular nitrogen can be reduced, electrochemically or by other means, to two high value chemicals, namely hydrazine and ammonia. Hydrazine is used for many applications, such as pharmaceuticals, pesticides and dyes,[1–3] while ammonia has been a fundamental chemical for mankind, mainly in the fertilizer and chemical industry. To this day, the Haber-Bosh process for ammonia synthesis has had an invaluable effect on the human population increase of the past century: it is estimated that about 40% of the world population depends on ammonia-derived fertilizers.[4] Haber's invention greatly lowered the price of nitrogen fixation, and fertilizers have increased more than two-fold the productivity of agricultural land.[5] However, its impact on the environment has been intensive due to both the loss of active nitrogen species in the environment (i.e. eutrophication) and the energetics of the Haber-Bosh synthesis. This process accounts today for 1% of the global primary energy supply.[6] Moreover, an analysis from the Institute of Industrial Productivity reported in *Chemical and Engineering News* in 2019 stated in the title: "Industrial ammonia production emits more CO_2 than any other chemical-making reaction. Chemists want to change that".[7] Finally, another source of impact for the Haber-Bosh process is the source of hydrogen, that is obtained almost exclusively from steam reforming of natural gas (i.e. gray hydrogen). Due to the importance of this fine chemical, there is a growing interest to research alternative and sustainable approaches for its preparation. Electrochemical synthesis of ammonia (ESA) through the nitrogen reduction reaction (NRR) has attracted significant attention.[8–10] The electrocatalytic reduction process is considered as an environmentally-friendly approach for NH_3 production. In fact, it can be performed from nitrogen and water at mild conditions, such as room temperature and atmospheric pressure, and it can also be powered by renewable energy.[11] The development of a sustainable ESA process requires primarily the knowledge of the thermodynamics aspects in the specific working environment (1), e.g. aqueous alkaline environment, that can be summarized by the following standard reduction potentials, and need to include the side HER (2) and hydrazine production (3):

$N_2 + 6H_2O + 6e^- \rightarrow 2NH_3 + 6OH^-$

$E^0 = -0.736$ V vs SHE at pH = 14 (1)

$2H_2O + 2e^- \rightarrow H_2 + 2OH^-$

$E^0 = -0.828$ V vs SHE at pH = 14 (2)

$N_2 + 4H_2O + 4e^- \rightarrow N_2H_4 + 4OH^-$

$E^0 = -1.160$ V vs SHE at pH = 14 (3)

The most important aspect of these concomitant reactions is that the reduction of nitrogen can, thermodynamically, start before water reduction (ca. 0.1 V earlier) but the 6 consecutive reduction steps (Fig. 4.1) result in many catalysts unable to prioritize NRR over HER.[12] In fact, the reported selectivities and partial NRR currents for many catalysts are so low to cast a shadow on their true catalytic activity.[13] The amount of produced ammonia is usually so low that it cannot be certainly related to electrochemical NRR rather than contamination from ammonia that is either already present or produced from other components of the experimental setup.

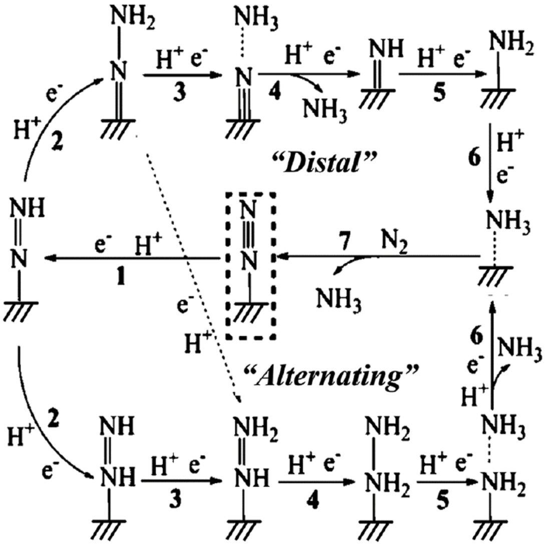

Figure 4.1 Schematic depiction of the associative pathways (including distal and alternating pathway) for catalytic conversion of N_2 to NH_3. Reproduced with permission from [12] Copyright 2016, American Chemical Society.

A considerable number of recent studies have investigated the importance to improve the measurement protocol to make sure that any detected NH_3 is actually produced from N_2 rather than any external contaminations or breakdown of the catalyst itself.[14] Moreover, many ammonia detection methods have been explored, but low sensitivity in the concentration range that these catalysts can manage represents a severe challenge.[15] Another parameter to focus on is the electrolyte and its compatibility with the particular detection method chosen. For example, in most typical Ionic Chromatography (IC) configurations (i.e. chromatography columns, flowing eluent etc.), the ammonium and sodium peaks elute at very near retention times, making difficult the accurate quantification of product in sodium-based electrolytes. Similarly, the colorimetric (i.e. spectrophotometric) methods, are sensible to pH. In particular, the salicylate method is only effective in alkaline solutions, while Nessler gives more consistent results throughout the entire pH window, but it is based on Hg salts that require some security measures.[16] Alternatively, NMR has been used successfully to detect ammonia in trace quantities, but the technique, as with IC, requires expensive components that could not be readily available to most catalysis labs.[17] For all these reasons, most of the research done in NRR catalysis hitherto has relied on more simple spectrophotometric methods that, although less reliable, can be used in conjunction with techniques to enhance reliability of results. Briefly, the salicylate reaction is catalyzed by sodium nitroprusside, necessary to promote an evident color development (Fig. 4.2a).[18] However, in some cases the blue color of the resulting indophenol complex is replaced by different color shades, resulting in ambiguous evidence.[15] On the other hand, the Nessler's method,[19] based on the ammonia reaction with K_2HgI_4 to give a colored complex (Fig. 4.2b), is a faster approach than the standard salicylate method, but it requires pretreatment steps to eliminate different interfering agents such as of metal ions, residual chlorine, sulfides, etc. Finally, products based on the colorimetric methods such as ammonia colorimetric assay kits have been commercialized to simplify the development process.

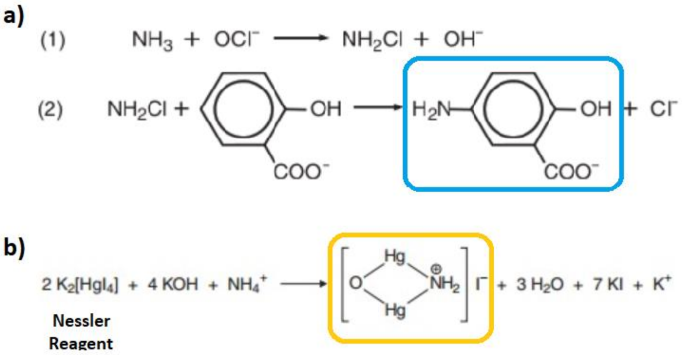

Figure 4.2 Reaction mechanisms of (a) salicylate method and (b) Nessler method for the determination of low-level ammonia in solution. The box colors represent the complexes color.

Recently, S. Z. Andersen et al.[13] proposed a strict procedure using $^{15}N_2$ to detect and quantify the electrochemical reduction of N_2 to NH_3. They demonstrated the importance of different contamination sources and showed how to remove labile nitrogen-containing compounds from the nitrogen gas as well as how to perform quantitative isotope measurements with the recycling of $^{15}N_2$ gas to contain the costs. However, the cost of labeled gas is still problematic regarding day-to-day experiments. The research of better quantification methods has proceeded in parallel to a prosperous literature on new NRR catalysts, able to suppress the competing HER process and resulting in higher ammonia production rates.[20] In this landscape, many materials that are known to be poor catalysts for the reduction of water have shown good activities for NRR. Moreover, techniques that modify the hydrophobicity of the catalytic surface have been successful in inhibiting proton adsorption and favoring that of N_2.[21] In general, carbon-based materials gained attention thanks to their intrinsic hydrophobicity, inertness to proton adsorption, low cost and versatility both as active catalysts and supports. In particular, stabilization of the active site is of paramount importance in these kinds of materials, given the reliance on intrinsically unstable structures such as defects sites, unusual facets, or single-atom catalysts.[22,23] For similar reasons, Metal Organic Frameworks (MOF) and Covalent Organic Frameworks (COF) are powerful structures in catalysis and have been used in nanocomposites to boost NRR activity. As an example, Yang et al. embedded nanoporous gold (NPG) in ZIF-8 (a MOF based on Zinc and Imidazole linkers) obtaining a composite material with an ammonia production rate and selectivity one order of magnitude higher than the starting materials.[24] This synergistic effect is at the heart of catalyst research, looking for novel properties arising from the appropriate combination of material components. (Fig. 4.3).

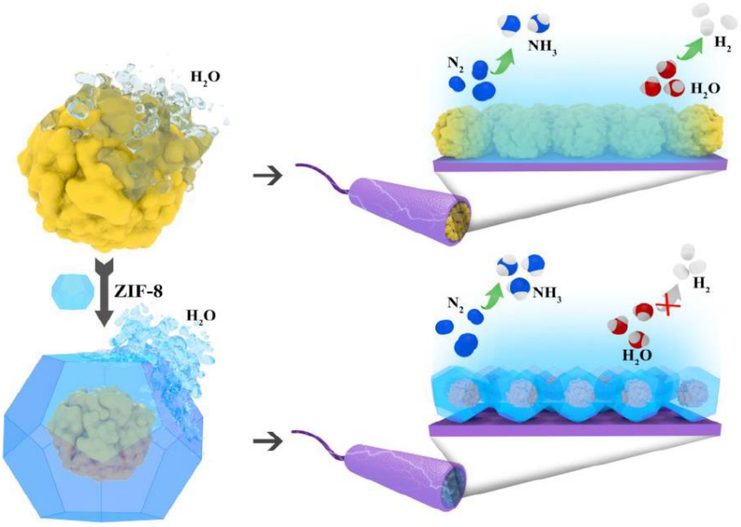

Figure 4.3 Enhancement of NRR over encapsulated NPG@ZIF-8 over the original NPG. Reproduced with permission from ref. [24]. Copyright © 2019 John Wiley & Sons, Inc.

4.2 A screening technique for potential NRR electrocatalysts

As previously discussed, the research of active NRR catalysts is somewhat slowed down by a laborious ammonia detection method. A cleaning protocol (for more information se section 2.2) is therefore needed to ensure that any NH_3 detected is produced from N_2 and not from any contamination. Previous studies[25,26] have suggested the necessity of control runs: in nitrogen-saturated electrolyte at open circuit potential (OCP), to assess contamination from the feed-gas stream, and in argon-saturated electrolyte at operating potential, to rule out any ammonia that can be released from within the cell or the catalyst itself. However, one time-saving solution could be the *operando* determination of NRR activity during catalysis, given the slow nature of ammonia detection methods and the need to keep all the electrochemical setup clean from NH_3 contaminations. A rotating ring-disc electrode (RRDE) tool could represent a sustainable, cost effective and primarily a rapid alternative method to study qualitatively the NRR process by the identification of products formed at the disc.[27] The RRDE tool, already adopted in many electrochemical labs, has been extensively used to study the kinetics of different electrochemical systems mainly centered on Oxygen Reduction Reaction (ORR). More recently (2014), the RRDE technique has been used by Lates et al.[28] to study the electrochemical reduction of CO_2 on Au-based electrocatalysts to produce CO. In 2018, Zhu and coworkers[29] extended the RRDE to characterize the CO_2 reduction process by Cu-based nanocatalysts resulting in the production of different hydrocarbon species. Other interesting research papers explore the use of RRDE to study particular electrochemical aspects including OER,[30,31] the chlorine evolution side reaction[32,33] and hydrogen peroxide selectivity from the 2 electron ORR.[34] The present chapter describes the investigation of the NRR through a series of electrocatalytic RRD voltammetry experiments in alkaline aqueous environment, where the NH_3 product oxidation on the platinum electrode is most visible.[35] The consequent NH_3 product monitoring on the Pt ring electrode is akin to an *in situ* detector as evidenced in the schematic reported in Fig. 4.4.

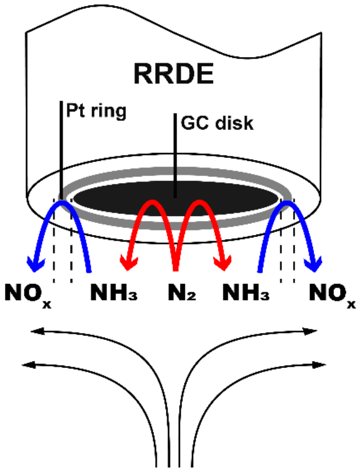

Figure 4.4 Schematics of the main NRR reactions occurring on GC/Pt electrodes of the RRDE.

Since different products can be generated simultaneously at highly negative potentials by the NRR electroactive material deposited on the GC electrode (i.e. NH_3, but also H_2, or N_2H_4), it is important to calibrate the ring electrode voltage to target ammonia electrogeneration. According to Endo and coworkers,[36] anodic ammonia oxidation process on Pt ring in alkaline environment could lead to different NOx products, even if the mechanisms have not been yet completely understood, due in part to parasite electrode poisoning. Most researchers considered reliable the Gerischer - Mauerer mechanisms (Eq. 4-9) based on the dehydrogenation steps of NH_3^* to N* and the recombination of two NH_x^*. Although NH_x or N_2H_y could be oxidized more easily on Pt than ammonia itself, they appeared to be too unstable in solution to be detected on the ring electrode. Therefore, NH_2OH has also to be considered as a candidate product formed on the disk electrode by NH_2 and OH^- (Eq. 9).

$$NH_3(aq) \rightarrow NH_3^* \quad (4)$$

$$NH_3^* + OH^- \rightarrow NH_2^* + H_2O + e^- \quad (5)$$

$$NH_2^* + OH^- \rightarrow NH^* + H_2O + e^- \quad (6)$$

$$NH_x^* + NH_y^* \rightarrow N_2H_{x+y}^* \quad (7)$$

$$N_2H_{x+y}^* + (x + y)OH^- \rightarrow N_2 + (x + y)H_2O + (x + y)e^- \quad (8)$$

$$NH_2^* + OH- \rightarrow NH_2OH + e^- \quad (9)$$

To test the potential of the RRDE technique, three different known NRR electrocatalysts were prepared, according to literature procedures. These materials were tested qualitatively with the RRDE and quantitatively with colorimetric tests to confirm their activity. The catalysts are representative of different situations we encountered during NRR testing and well elucidate the resilience of this qualitative technique to different scenarios. First, commercial Carbon Nanotubes (CNTs) supporting Fe_2O_3 Nanoparticles (30% Fe_2O_3-CNTs)[37] were studied as an example of NRR electrocatalyst operating at low overpotentials, therefore showing limited ammonia production rates. Then, a ZIF-8 derived nitrogen-doped carbon (ZIF-1100-1h)[38] was evaluated as the representative of a vast family of N-containing catalysts that showed high FE, but that are potentially unstable. This instability could be the real source of ammonia and has to be addressed in the protocol to limit false positives. Finally, a commercial Fe_2O_3 (Honeywell, pur. 99.98%)[39] was tested to document the class of electrocatalysts characterized by NRR activity at high overpotentials, where the vigorous H_2 formation gives rise to technical measurement complications. The cleaning of the electrochemical setup was of primary importance for each measurement. Therefore, ahead of each test, multiple washing steps of all the electrochemical components in the setup were necessary (i.e. cell, electrodes, bridges, frits, etc.). We demonstrated that this experimental approach is effective to discern also a low-level ammonium concentration through monitoring the ammonia oxidation peak at the ring electrode for a fast (in the order of minutes with a consolidated protocol) and preliminary electrocatalytic NRR performance evaluation.

4.2.1 Experimental Section

Material Synthesis. Iron nitrate nonahydrate $Fe(NO_3)_3 \cdot 9H_2O$, Hydrazine hydrate(N_2H_4, 60%), Salycilic acid, sodium citrate tribasic, sodium dichloroisocyanurate dihydrate, Nafion 117® 5% solution, nitric acid (HNO_3, 70%), Hydrochloric acid (HCl, 35%), Ethylene glycol (98%), Methanol (99,8%) were purchased from Sigma–Aldrich. Sodium nitroprusside and 2-propanol were purchased from Carlo Erba. Ammonium hydroxide solution (NH_3, 25%), Zinc nitrate hexahydrate $Zn(NO_3)_2 \cdot 6H_2O$, 2-methyl Imidazole, potassium hydroxide (KOH, puriss. p.a. >85%) were purchased from Fluka. All experiments were conducted with milliQ water obtained by using a Direct-Q (Millipore) water purification system.

CNTs supported Fe_2O_3 NPs (30% Fe_2O_3-CNTs) were synthetized according to literature.[37] CNTs were first oxidized in concentrated HNO_3 at reflux for 2h, then washed in DI water and dried under reduced pressure at 60°C. $Fe(NO_3)_3$ was dissolved in a 25mL DI water and 1mL ethylene glycol dispersion of the obtained o-CNTs. A 5% ammonia solution was added dropwise till pH 8 and then the product was filtered and dried at 120°C. Finally, the material was calcinated in a tubular furnace under Ar gas at 400°C. The obtained catalyst was characterized by Inductively Coupled Plasma-Optical Emission Spectrometry (ICP-OES) to check for effective iron loading.

ZIF-8 derived nitrogen-doped carbon (ZIF-1100-1h) was synthetized according to literature.[38] First, ZIF-8 were prepared mixing equal volumes of methanol solutions of reactants 2-methylimidazole and $Zn(NO_3)_2 \cdot 6H_2O$ to obtain a final molar ratio of 4:1. The solution was aged for 24h at 60°C and then the solid was collected through centrifugation and consecutive methanol washing to remove excess reactants. The obtained material was pyrolyzed under Ar flow for 1h at 1100°C in a tubular furnace and then washed in 0.1M HCl solution.

Iron(III) oxide (99.98%) was bought from Honeywell and used without further purification steps.[39]

Electrochemical testing. Prior to each measurement a standardized cleaning protocol of the entire electrochemical setup (cell, bridges, electrodes and gas inlet, frits, etc.), was adopted to avoid external interferences. Therefore, the glass cell was filled with milliQ water, and everything was kept soaking. Every 20 minutes, the water was removed and the process repeated for at least 6 times. Finally, the cell was filled with the desired amount of electrolyte. The detailed cleaning sequence and checks is reported in Section 2.2. All the inks were prepared and the dispersion concentrations were kept at 2.5 mg mL^{-1}. A variable ink volume was coated on the GC disc to achieve a designed loading of 300, 300 and 100 µg cm^{-2} for 30% Fe_2O_3-CNTs, ZIF-1100-1h and commercial Fe_2O_3, respectively, allowing a better comparison with published data. Prior to each NRR test, the complete assembled system was degassed with pure Ar for 30 min.

Electrocatalytic activities were evaluated in a 0.1 M KOH solution. Three different types of measurements were used to characterize the different NRR electrocatalysts. First, the material deposited on the disk electrode was cycled in cyclic voltammetries (CVs) from Open Circuit Potential (OCP) to –0.6 V vs. RHE, while the Pt ring potential was set to 0.7 V vs. RHE, corresponding to the potential value where NH_3 oxidation takes place. (Fig. 4.5c)

As a second set of experiments, the same GC–supported electrocatalysts were subjected to relatively fast (time order, tens of seconds) chronoamperometric tests (CAs) at fixed potential values corresponding to those where the materials would be active toward NRR, while the Pt ring would cycle in CVs inside the water stability window (0 ~ 1.4 V vs. RHE). During the complete sequence of measurements, the CV scan speed was set to 100 mV s^{-1} to both limit the formation of bubbles on the catalyst layer and have clear electrochemical peaks on the platinum ring. For similar reasons the rotation speed of the RRDE setup was limited to 200 rpm.[36]

A further set of prolonged CAs (time order of hours for product accumulation) was finally done to ascertain the faradaic efficiency (FE), by two different colorimetric analysis, and its closeness to published data. In accordance with the previous experimental setup the electrocatalysts were supported on the GC disc of RRDE electrode and subjected to three CAs measurements in different operative conditions: i) the first one was performed with the disk electrode at OCP in N_2–saturated electrolyte to check for impurities coming from the experimental setup; ii) the second one was recorded at the NRR operative potentials in Ar- saturated solution to check for stability of the material; iii) and finally the third CA test was collected at operative potentials in N_2-saturated electrolyte; these steps were completed including the systematic quantitative spectrophotometric NH_3 detection

4.2.2 Results and discussion

All measurements were done in a single-chamber electrochemical cell, the simplest possible configuration, to decrease the possibility of ammonia contamination. This setup has fewer pieces and relies on Vycor® frits to separate the electrodes. The single-compartment cell used in this study consisted of a glass cell filled with 20 mL 0.1 M KOH electrolyte, equipped with a GC/Pt RRDE as the working electrodes. A preliminary step must be the calibration of the platinum ring electrode to known quantities of the possible catalysis products (i.e. NH_3, N_2H_4 and H_2) to understand at which potentials the platinum electrode is most sensible to each product.

GC/Pt RRDE preliminary blank tests. A CV on Pt electrode was done in Ar-saturated 0.1M KOH spanning the entire electrolyte stability window (Fig. 4.5a). CVs with the same parameters were registered with the addition of either 1 mM hydrazine (Fig. 4.5b) or 0.1 M NH_3 (Fig. 4.5c). Furthermore, to simulate H_2 bubbling, the uncovered polished GC disc electrode was subjected to a CA at –1 V vs. RHE, generating a stable current of 0.2 mA (Fig. 4.5d). The voltammograms are in very good agreement with literature data. The Pt ring electrode resulted highly active toward hydrazine oxidation with an oxidation peak at 0.2 V vs. RHE followed by a plateau. Moreover, the N_2H_4 oxidation peak resulted highly dependent on the rotation speed of the electrode, confirming previous observations of diffusion-limited behavior.[40] Ammonia oxidation, on the other hand, showed an irreversible peak at 0.7 V vs. RHE, and as expected was only marginally affected by the rotation speed.[36,41,42] Lastly, hydrogen showed a broad diffusion limited oxidation peak between 0 and 1 V vs. RHE, at which point Pt oxidation to platinum oxide deactivates the electrode surface to HOR.[43]

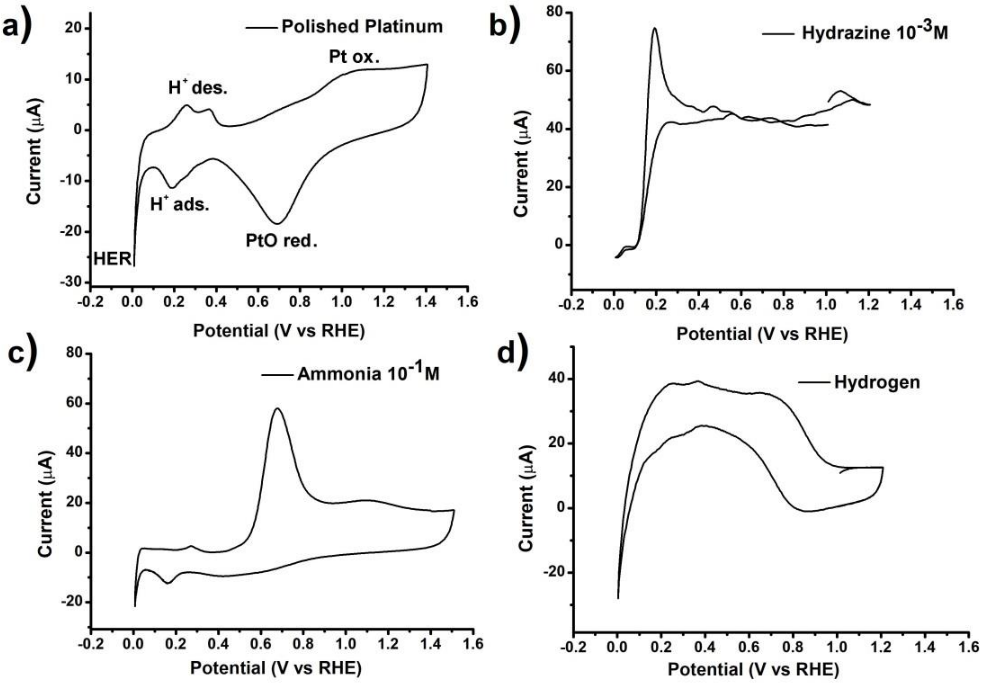

Figure 4.5 Cyclic Voltammetry scans of NRR involved products. CVs on polished Pt ring (a) with added hydrazine (b), ammonia (c) or in situ produced hydrogen (d).

Electrocatalyst fingerprint for NH_3 production. A first approach to studying the NRR catalytic properties of our materials was performed scanning (i.e. with a CV) the catalysts on the GC disk between OCP and -0.6 V vs RHE while the potential at the ring electrode was fixed at 0.7 V vs RHE, where platinum is most sensible to ammonia (Fig. 4.5c). The resulting plots (ring currents vs applied potential at the disk) show in all cases an increase of the ring current in N_2-saturated electrolyte in respect to Ar-saturated electrolytes. These differences, while indicative, were not a conclusive proof of nitrogen activation, because at that potential (0.7 V vs RHE) platinum can oxidize both ammonia and hydrogen. Therefore, a better picture of the process is needed exploiting combined disk-ring CVs.

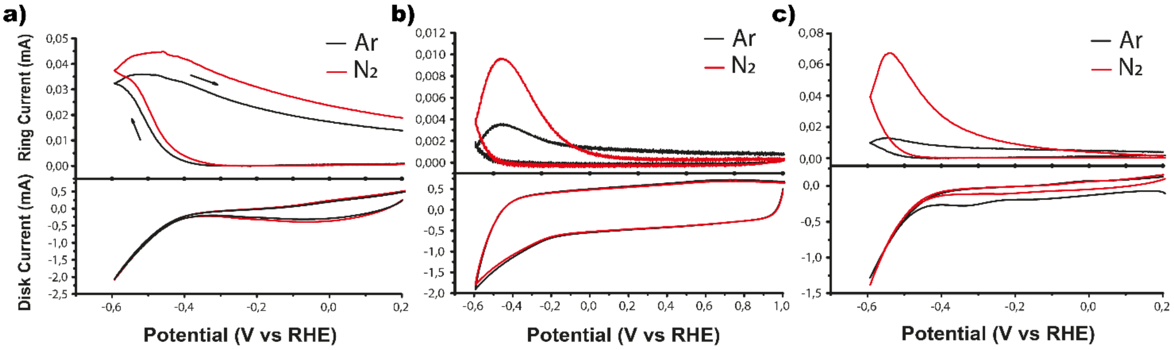

Figure 4.6 Disc and ring current responses recorded at 0.7V vs RHE for Pt ring during cycling of the disc –supported catalytic material. Case of 30% Fe_2O_3-CNTs (a), ZIF-1100-1h (b) and Fe_2O_3 (c). RRDE rotation speed 200 rpm.

The exploration of 30% Fe_2O_3-CNTs catalyst was conducted under the most critical operative conditions among the three studied electrocatalysts, due to the combination of low selectivity (FE to NH_3) and current at the investigated working potential. In Fig. 4.6a the ring currents at 0.7 V vs. RHE in Ar- (blank) and N_2-saturated electrolyte are reported, during CV cycling of the catalytic material on the disk. While the CV on the disc showed little differences between Ar- and N_2- scans, the ring electrode recorded an earlier activation potential starting from -0.25 V vs. RHE for the NRR process. However, in literature it is reported that NRR on 30% Fe_2O_3-CNTs starts even earlier, albeit with very low partial currents. Therefore, further combined RRDE–based experiments were needed to assess the NRR performance and to enhance the sensitivity of the method

In order to obtain a more detailed understanding, CAs of the GC-supported materials were carried out at different potentials, while the ring electrode was scanned in the water stability window. For all the three catalyst, hydrazine-related peaks, near 0.2 V vs RHE, were never observed. The case of 30% Fe_2O_3-CNTs was summarized in Fig. 4.7: local presence of ammonia was already detected in a single CV scan on the Pt electrode (20s, Fig. 4.7a). Running a longer CA on the catalyst (1500s, Fig. 4b), a CV on the ring electrode can be then employed to probe the bulk accumulation of NH_3 during the CA test, as also confirmed by conventional colorimetric analysis (Fig. 4.8b). Another noticeable difference was represented by the slight shift of the platinum oxide reduction peak. In a prolonged RRDE–based CA test this peak tends to decrease in magnitude, due to partial coverage of the platinum surface with strongly binding intermediates of the ammonia oxidation reaction.[36]

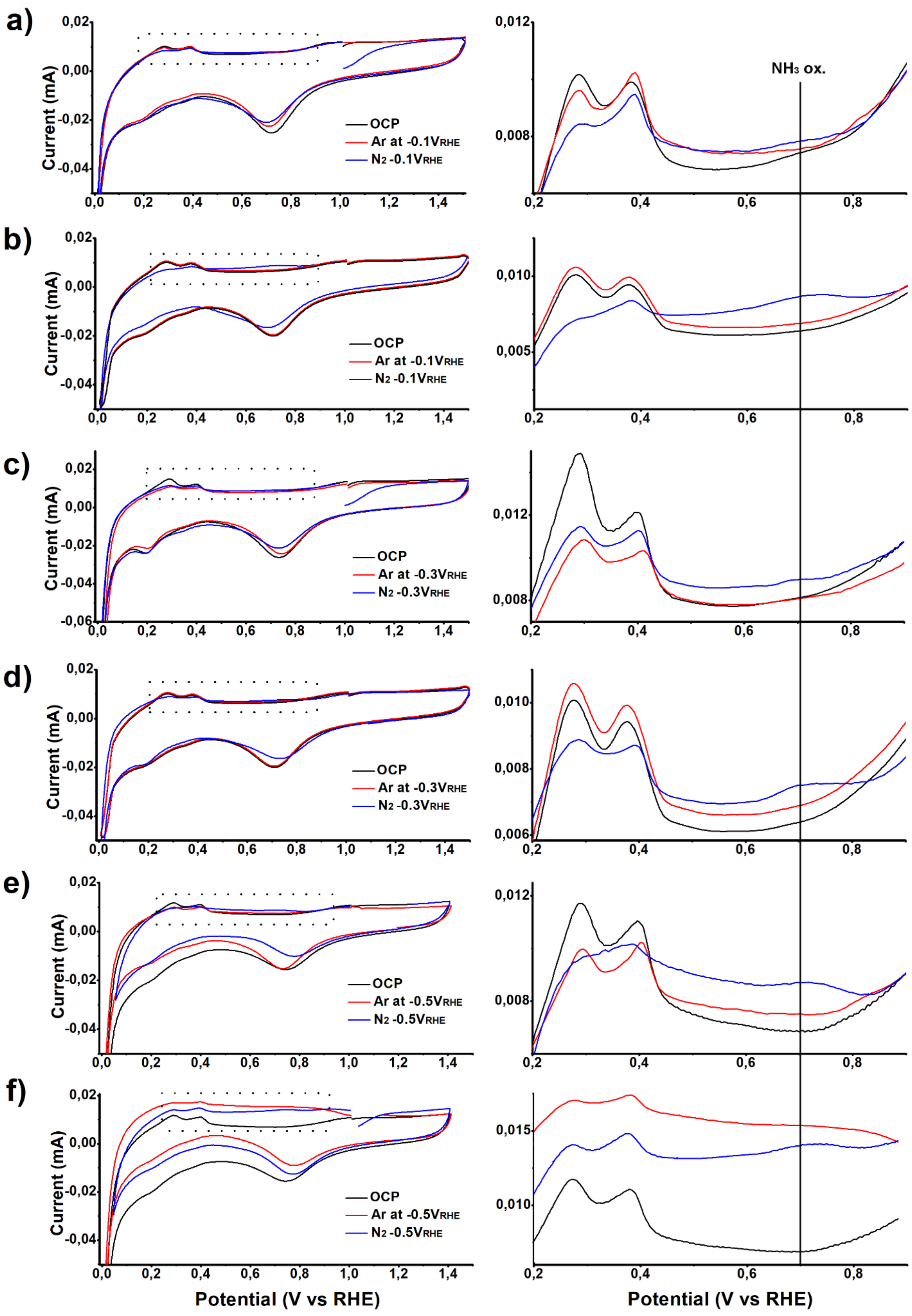

Figure 4.7 CVs on Pt ring (enlarged version on the right): GC covered by 30% Fe_2O_3-CNTs (a,b), ZIF-1100-1h (c,d) and Fe_2O_3 (e,f). The disc electrode was fixed at different operative potentials for 20s (a,c,e) and for 1500s (b,d,f). RRDE rotation speed was fixed 200 rpm.

A recent investigation by Chen et al.[37] considerably improved the ammonia formation rates and FEs for the same 30% Fe_2O_3-CNT electrocatalyst in different electrolytes, accounting for the highest ammonia formation rate and FEs to NH_3 with alkaline 0.5 M KOH electrolyte in a gas flow cell. In particular, at -0.04 V vs. RHE, the authors accounted for an ammonia formation rate of 1.86×10^{-12} mol cm^{-2} s^{-1} with NH_3 Faradaic selectivity of 0.59%, in their optimized cell setup.

It must be noticed, however, that our prolonged CA tests were done in a single-chamber cell with a GC-RDE as the catalyst support. Nonetheless, the resulting currents compared well with reported values (Fig. 4.8) and, similarly, we found a FE at -0.1 V vs. RHE of 0.5% (Tab. 4.1) and a formation rate of 3.66×10^{-12} mol $s^{-1}cm^{-2}$ (Tab 3.2) in 0.1 M KOH electrolyte.

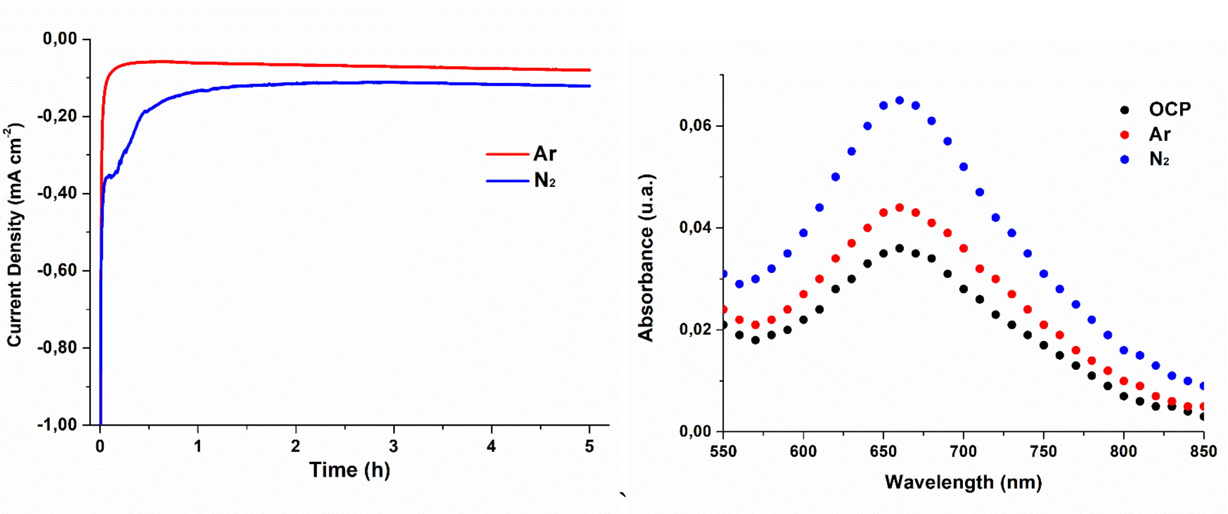

Figure 4.8 (a) CA tests for 30% Fe_2O_3-CNTs material at -0.1 V vs RHE in Ar- (black) and N_2- (blue) saturated 0.1M KOH electrolyte. (b) resulting spectra for the salicylate method revealing the ammonia produced during NRR against Ar and OCP control tests.

Electrocatalytic material degradation: false positives identification. A further important application of the RRDE-based analysis technique was referred to the time stability evaluation of nitrogen-containing catalyst in the operative environment (i.e. alkaline environment). N-based materials have been proposed as one of the most promising classes of electrocatalysts[44–46] for highly selective N_2 reduction at low overpotentials, but in some cases their performance could be ambiguously affected by the NH_3 produced via catalyst decomposition rather than truly NRR process. Due to the high sensitivity of RRDE setup, we employed the CV fingerprints in Ar-saturated electrolyte at OCP and at the investigated reductive potentials to identify possible false positives. For this purpose we investigated the electrocatalytic behavior of a ZIF based material. In this case, the setup cleaning was of primary importance in the following evaluations (as highlighted in the section “Cleaning procedure” in Section 2.2), as traces of environmental ammonia could lead to false NRR results limiting the possible application of this class of electrocatalytic materials. Hence, a consecutive washings procedure (at least 4 times) was adopted to keep the NH_3 levels in solution below a detectable level on the Pt ring. The downward trend of ammonia levels was also visible in colorimetric analysis throughout the cleaning procedure.

ZIF-1100-1h showed high NRR performance in N_2-saturated 0.1M KOH electrolyte, confirmed by the remarkable Pt ring currents increase (Fig. 4.6b). The sole currents evaluation, however, does not preclude the possibility of catalyst breakdown interference; therefore, a further analysis at the Pt electrode was needed. In the shorter CA test (20 s, Fig. 4.7c), similarly to the 30% Fe_2O_3-CNTs case, a small peak shoulder was visible at 0.7 V vs. RHE in the CV scan under N_2 flow. The absence of peaks in the same operative conditions but under Ar flow was considered significant but not definitive of catalyst stability. A prolonged CA test (1500 s, Fig. 4.7d) confirmed the ZIF-1100-1h stability. In fact, in N_2- saturated electrolyte, the CV peak at 0.7 V vs. RHE showed the expected increase due to prolonged activity, while in Ar- saturated electrolyte no peak was observed. Again, a decrease in magnitude of the Pt-oxide reduction peak was also detected, in agreement with the findings on the previous catalyst. Finally, the stability of Nafion® 117 as the ink binder could be deduced by these measurements at negative biases from the lack of any ammonia trace on the platinum CV. Mukherjee et al.[38] determined the electrocatalytic activity of ZIF-1100-1h at -0.3 V vs. RHE, where the best performances in terms of FE were observed, at 10%. Two colorimetric analyses confirmed NRR electroactivity at this potential value with a corresponding high FE of 6.5% and 4.0% by salicylate and Nessler method, respectively (Fig. 4.9 and Tab. 4.1).

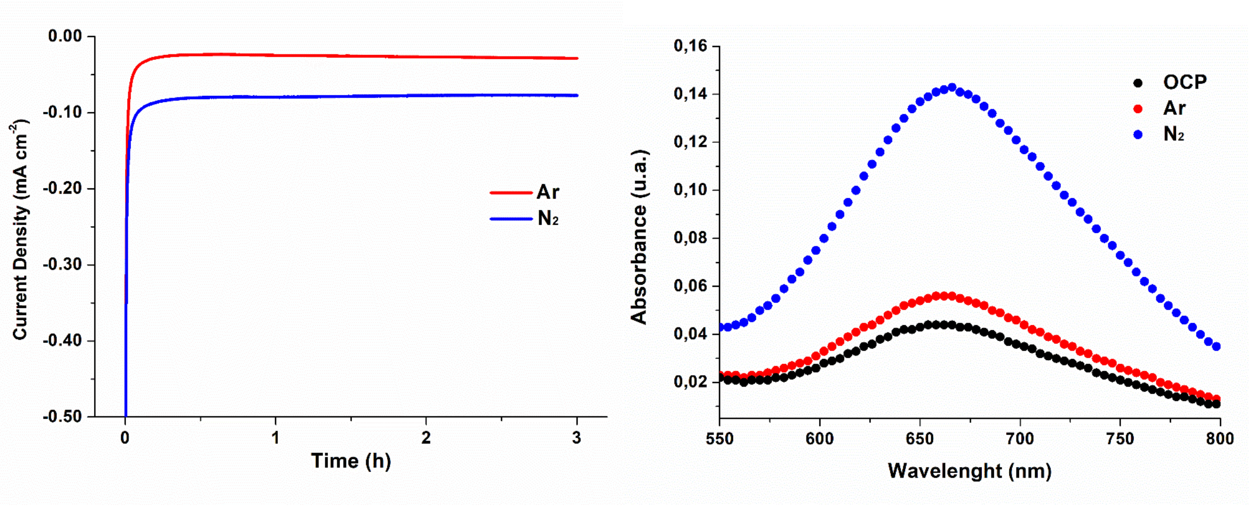

Figure 4.9 (a) CAs measurements for ZIF-1100-1h at -0.3 V vs. RHE in Ar- (black) and N_2 (blue) saturated 0.1M KOH electrolyte and (b) resulting spectra for the salicylate method revealing the ammonia produced during NRR against Ar and OCP control tests.

Overcoming parallel H_2 generation. Hydrogen interference during NRR represents one of the main problems in RRDE – based experiments due to the closeness of disk and ring electrodes. In fact, at high cathodic currents, the production of hydrogen exceeds the local solubility of the gas and results in the formation of bubbles. This is commonly registered by the ring electrode as a noisy CV that mostly resembles the hydrogen oxidation profile on Pt electrode reported in Fig. 4.5d. This case study is well represented by the Fe_2O_3 (commercial) investigated electrocatalyst. The corresponding ring currents on bulk RRDE tests (Fig. 3c) suggested high activity toward NRR at high overpotentials; however, H_2 side production heavily occurred. The attempt to identify the NRR products by Pt ring CV during a disc CA, in accordance with the method discussed so far, resulted in unclear data, due to H_2 bubble interference (Fig. 4.10).

The elimination of the H_2-related noise was addressed by gaining a cleaner NRR profile with a rather noticeable ammonia peak, only when the CV on the Pt ring electrode was started after the end of the catalysis stage on the disk, by adopting a delay of 20 s. This approach resulted suitable for both short (20 s) and longer (1500 s) CAs, as long as all H_2 bubbles were removed by flowing the sparging gas directly on the electrode surface (Fig. 4.7e, f). The CVs profile still results in a high hydrogen plateau, but the ammonia peak is in this way perfectly appreciable. In the case of Fe_2O_3, the ammonia peak did not seem to grow significantly with time. The modified method could have lower sensitivity due to the predominant diffusion of species during delay time assisted by the abundant production of H_2 bubbles. Moreover, a loss in selectivity toward NRR over time could not be excluded. In fact, at these significantly negative potentials, the surface iron oxide is slowly reduced to a mix of Fe and $Fe(OH)_2$ that is more active (Fig. 4.11) in terms of generated current, but whose selectivity toward NRR remains unclear.[47]

A two-hours CA test at -0.5 V vs RHE was used to determine the ammonia FE of the material, corresponding to 0.04% (salicylate method) also confirmed by Nessler reaction (Table 4.1). This value is in the same order of magnitude of that reported by Furuya et al.,[39] despite different cell structure and operative conditions were used. Notably, our prolonged CA with respect to the short catalysis previously used[39] and the chemical modifications on the surface[47] could justify our hypothesis of a selectivity decrease with time.

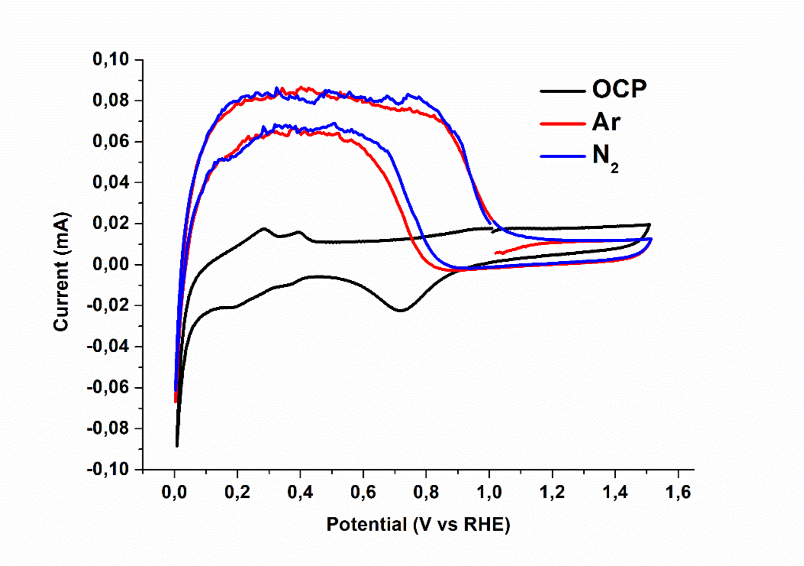

Figure 4.10 CVs on Pt ring for Fe_2O_3 electrocatalysts recorded during a CA test at -0.5 V vs. RHE for 20s. The presence of bubbles as well as dissolved H_2 covered any possible NH_3 peak.

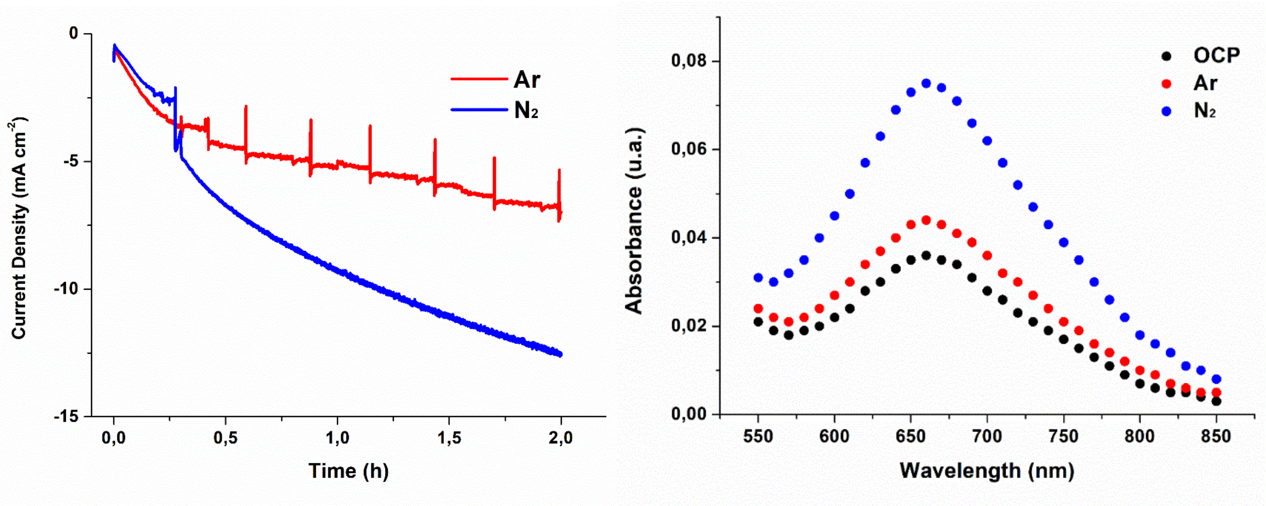

Figure 4.11 (a) CA measurements for Fe_2O_3 material at -0.5 V vs. RHE in Ar- (black) and N_2- (blue) saturated 0.1M KOH electrolyte and (b) resulting spectra for the salicylate method revealing the ammonia produced during NRR against Ar and OCP control tests.

Material	*Calculated FE (Potential)*	*Reported FE (Potential)*
30% Fe_2O_3-CNTs	**0.5%** / 0.5% (-0.1 V vs RHE)	0.59% (-0.04 V vs RHE)
ZIF-1100-1h	**6.5%** / 4.0% (-0.3 V vs RHE)	10.2% (-0.3 V vs RHE)
Fe_2O_3	**0.04%** / 0.03% (-0.5 V vs RHE)	0.06% (-1 V vs RHE)

Table 4.1. FEs for the investigated electrocatalysts, measured at the specified potentials in brackets. Calculated FEs are referred to indophenol method (bold) and confirmed by Nessler method.

Material	*Calculated NH_3 formation rate (mol $s^{-1}cm^{-2}$)*	*Reported NH_3 formation rate (mol $s^{-1}cm^{-2}$)*
30% Fe_2O_3-CNTs	3.66×10^{-12}	1.86×10^{-12} [1]
ZIF-1100-1h	2.25×10^{-11}	9.4×10^{-10}[2]
Fe_2O_3	3.45×10^{-12}	8.6×10^{-10}[3]*

Table 4.2 Ammonia formation rates calculated for the investigated electrocatalysts, and literature comparison (see references for comparing experimental conditions).

4.2.3 Conclusions

The NRR electrochemical performance for ammonia production was investigated by the use of the RDDE-based analysis technique to provide a preliminary qualitative information and the obtained data were confirmed by the traditional quantitative colorimetric tests. Three well established NRR electrocatalysts were prepared in accordance with literature procedures to represent different working potentials and currents: a CNTs supported Fe_2O_3 NPs (30% Fe_2O_3-CNTs), a commercial Fe_2O_3 and a ZIF-8 derived nitrogen-doped carbon (ZIF-1100-1h). The Pt ring electrode of the RRDE setup has been used to identify the products from N_2 reduction. Ammonia was identified as the unique product from electrochemical reduction of N_2 using all the three investigated electrocatalysts in 0.1M KOH solution and room temperature. When the disc electrode was scanned, the ring electrode detected the oxidation peak when it was held at 0.7 V vs. RHE, indicating that the product from N_2 reduction was oxidized around this potential on the Pt ring electrode. This information was subsequently confirmed by scanning the ring electrode with the three different catalysts held at specific and proved reducing potentials (each corresponding to a consistent oxidation peak at 0.7 V vs. RHE on the ring electrode).

Different results were targeted by the use of this fast screening method for NRR electrocatalytic activity, in alkaline environment. Firstly, we demonstrated that the RRDE experimental approach is effective to discern also a low-level ammonia concentration that occurs in particular operative conditions such as low overpotentials and currents; this specific case was represented by the 30% Fe_2O_3-CNTs electrocatalyst, that was characterized by limited FEs, below 1 %. Secondly, the high sensitivity of RRDE setup allowed the use of CV fingerprints obtained in Ar-saturated electrolyte, at both OCP and at reductive potentials, to identify false positives. To this purpose the case of ZIF-1100-1h was deepened to account for the class of N-doped carbon-based catalysts affected by possible degradation in the operative conditions, contributing with a secondary source of ammonia. Finally, hydrogen interference during NRR is one of the main problems in RRDE– based experiments at high cathodic currents; this phenomenon is registered by the ring electrode as a noisy cyclic voltammograms. In an attempt to overcome H_2-related noise, we gained a cleaner NRR profile with a visible ammonia peak, only when the CV on the Pt ring electrode was started after the end of the catalysis stage on the disc, by adopting a delay of 20 s. This approach resulted suitable for both short and longer CAs, having care to remove all hydrogen bubbles. The CV profile still result in a high hydrogen plateau, but the ammonia peak was perfectly visible. Based on the obtained results in different operative conditions, it is possible to assert that the excellent versatility of the investigated RRDE method, employed for a preliminary fingerprint of new NRR electrocatalyst candidates, could allow to fastly discern false positives and to reserve time and cost consuming analysis only for promising materials.

4. References

(1) Elder, D. P.; Snodin, D.; Teasdale, A. Control and Analysis of Hydrazine, Hydrazides and Hydrazones—Genotoxic Impurities in Active Pharmaceutical Ingredients (APIs) and Drug Products. *Journal of Pharmaceutical and Biomedical Analysis* **2011**, *54* (5), 900–910. https://doi.org/10.1016/J.JPBA.2010.11.007.

(2) Cui, L.; Ji, C.; Peng, Z.; Zhong, L.; Zhou, C.; Yan, L.; Qu, S.; Zhang, S.; Huang, C.; Qian, X.; Xu, Y. Unique Tri-Output Optical Probe for Specific and Ultrasensitive Detection of Hydrazine. *Analytical Chemistry* **2014**, *86* (9), 4611–4617. https://doi.org/10.1021/AC5007552.

(3) Nguyen, K. H.; Hao, Y.; Chen, W.; Zhang, Y.; Xu, M.; Yang, M.; Liu, Y. N. Recent Progress in the Development of Fluorescent Probes for Hydrazine. *Luminescence* **2018**, *33* (5), 816–836. https://doi.org/10.1002/BIO.3505.

(4) Smil, V. Nitrogen and Food Production: Proteins for Human Diets. *AMBIO: A Journal of the Human Environment* **2002**, *31* (2), 126–131. https://doi.org/10.1579/0044-7447-31.2.126.

(5) Stewart, W. M.; Dibb, D. W.; Johnston, A. E.; Smyth, T. J. The Contribution of Commercial Fertilizer Nutrients to Food Production. *Agronomy Journal* **2005**, *97* (1), 1–6. https://doi.org/10.2134/AGRONJ2005.0001.

(6) Erisman, J. W.; Sutton, M. A.; Galloway, J.; Klimont, Z.; Winiwarter, W. How a Century of Ammonia Synthesis Changed the World. *Nature Geoscience 2008 1:10* **2008**, *1* (10), 636–639. https://doi.org/10.1038/ngeo325.

(7) *Industrial ammonia production emits more CO_2 than any other chemical-making reaction. Chemists want to change that*. https://cen.acs.org/environment/green-chemistry/Industrial-ammonia-production-emits-CO2/97/i24 (accessed 2022-05-13).

(8) Cui, X.; Tang, C.; Zhang, Q. A Review of Electrocatalytic Reduction of Dinitrogen to Ammonia under Ambient Conditions. *Advanced Energy Materials* **2018**, *8* (22), 1800369. https://doi.org/10.1002/aenm.201800369.

(9) Montoya, J. H.; Tsai, C.; Vojvodic, A.; Nørskov, J. K. The Challenge of Electrochemical Ammonia Synthesis: A New Perspective on the Role of Nitrogen Scaling Relations. *ChemSusChem* **2015**, *8* (13), 2180–2186. https://doi.org/10.1002/CSSC.201500322.

(10) van der Ham, C. J. M.; Koper, M. T. M.; Hetterscheid, D. G. H. Challenges in Reduction of Dinitrogen by Proton and Electron Transfer. *Chemical Society Reviews*. Royal Society of Chemistry August 7, 2014, pp 5183–5191. https://doi.org/10.1039/c4cs00085d.

(11) Rod, T. H.; Logadottir, A.; Nørskov, J. K. Ammonia Synthesis at Low Temperatures. *Journal of Chemical Physics* **2000**, *112* (12), 5343–5347. https://doi.org/10.1063/1.481103.

(12) Li, X. F.; Li, Q. K.; Cheng, J.; Liu, L.; Yan, Q.; Wu, Y.; Zhang, X. H.; Wang, Z. Y.; Qiu, Q.; Luo, Y. Conversion of Dinitrogen to Ammonia by FeN3-Embedded Graphene. *J Am Chem Soc* **2016**, *138* (28), 8706–8709. https://doi.org/10.1021/JACS.6B04778.

(13) Andersen, S. Z.; Čolić, V.; Yang, S.; Schwalbe, J. A.; Nielander, A. C.; McEnaney, J. M.; Enemark-Rasmussen, K.; Baker, J. G.; Singh, A. R.; Rohr, B. A.; Statt, M. J.; Blair, S. J.; Mezzavilla, S.; Kibsgaard, J.; Vesborg, P. C. K.; Cargnello, M.; Bent, S. F.; Jaramillo, T. F.; Stephens, I. E. L.; Nørskov, J. K.; Chorkendorff, I. A Rigorous Electrochemical Ammonia Synthesis Protocol with Quantitative Isotope Measurements. *Nature*. Nature Publishing Group June 27, 2019, pp 504–508. https://doi.org/10.1038/s41586-019-1260-x.

(14) Greenlee, L. F.; Renner, J. N.; Foster, S. L. The Use of Controls for Consistent and Accurate Measurements of Electrocatalytic Ammonia Synthesis from Dinitrogen. *ACS Catalysis* **2018**, *8* (9), 7820–7827. https://doi.org/10.1021/ACSCATAL.8B02120.

(15) Zhao, Y.; Shi, R.; Bian, X.; Zhou, C.; Zhao, Y.; Zhang, S.; Wu, F.; N Waterhouse, G. I.; Wu, L.-Z.; Tung, C.-H.; Zhang, T.; Zhao, Y. X.; Shi, R.; Bian, X. A.; Zhou, C.; Zhao, Y. F.; Zhang, S.; Wu, F.; Wu, L.; Tung, C.; Zhang, T. R.; N Waterhouse, G. I. Ammonia Detection Methods in Photocatalytic and Electrocatalytic Experiments: How to Improve the Reliability of NH3 Production Rates? *Advanced Science* **2019**, *6* (8), 1802109. https://doi.org/10.1002/ADVS.201802109.

(16) Zhou, L.; Boyd, C. E. Comparison of Nessler, Phenate, Salicylate and Ion Selective Electrode Procedures for Determination of Total Ammonia Nitrogen in Aquaculture. *Aquaculture* **2016**, *450*, 187–193. https://doi.org/10.1016/j.aquaculture.2015.07.022.

(17) Nielander, A. C.; McEnaney, J. M.; Schwalbe, J. A.; Baker, J. G.; Blair, S. J.; Wang, L.; Pelton, J. G.; Andersen, S. Z.; Enemark-Rasmussen, K.; Čolić, V.; Yang, S.; Bent, S. F.; Cargnello, M.; Kibsgaard, J.; Vesborg, P. C. K.; Chorkendorff, I.; Jaramillo, T. F. A Versatile Method for Ammonia Detection in a Range of Relevant Electrolytes via Direct Nuclear Magnetic Resonance Techniques. *ACS Catalysis* **2019**, *9* (7), 5797–5802. https://doi.org/10.1021/ACSCATAL.9B00358.

(18) Verdouw, H.; van Echteld, C. J. A.; Dekkers, E. M. J. Ammonia Determination Based on Indophenol Formation with Sodium Salicylate. *Water Research* **1978**, *12* (6), 399–402. https://doi.org/10.1016/0043-1354(78)90107-0.

(19) Leonard, R. H. Quantitative Range of Nessler's Reaction with Ammonia. *Clinical Chemistry* **1963**, *9* (4), 417–422. https://doi.org/10.1093/clinchem/9.4.417.

(20) Ithisuphalap, K.; Zhang, H.; Guo, L.; Yang, Q.; Yang, H.; Wu, G. Photocatalysis and Photoelectrocatalysis Methods of Nitrogen Reduction for Sustainable Ammonia Synthesis. *Small Methods* **2019**, *3* (6), 1800352. https://doi.org/10.1002/SMTD.201800352.

(21) Du, C.; Qiu, C.; Fang, Z.; Li, P.; Gao, Y.; Wang, J.; Chen, W. Interface Hydrophobic Tunnel Engineering: A General Strategy to Boost Electrochemical Conversion of N2 to NH3. *Nano Energy* **2022**, *92*, 106784. https://doi.org/10.1016/J.NANOEN.2021.106784.

(22) Chen, Y.; Ji, S.; Chen, C.; Peng, Q.; Wang, D.; Li, Y. Single-Atom Catalysts: Synthetic Strategies and Electrochemical Applications. *Joule* **2018**, *2* (7), 1242–1264. https://doi.org/10.1016/J.JOULE.2018.06.019.

(23) Qichen Wang; Yongpeng Lei; Dingsheng Wang; Yadong Li. Defect Engineering in Earth-Abundant Electrocatalysts for CO 2 and N 2 Reduction. *Energy & Environmental Science* **2019**, *12* (6), 1730–1750. https://doi.org/10.1039/C8EE03781G.

(24) Yang, Y.; Wang, S. Q.; Wen, H.; Ye, T.; Chen, J.; Li, C. P.; Du, M. Nanoporous Gold Embedded ZIF Composite for Enhanced Electrochemical Nitrogen Fixation. *Angewandte Chemie International Edition* **2019**, *58* (43), 15362–15366. https://doi.org/10.1002/ANIE.201909770.

(25) Tsuneto Akira; Kudo Akihiko; Sakata Tadayoshi. Efficient Electrochemical Reduction of N2 to NH3 Catalyzed by Lithium. *Chemistry Letters* **2006**, *22* (5), 851–854. https://doi.org/10.1246/CL.1993.851.

(26) Greenlee, L. F.; Renner, J. N.; Foster, S. L. The Use of Controls for Consistent and Accurate Measurements of Electrocatalytic Ammonia Synthesis from Dinitrogen. *ACS Catalysis* **2018**, *8* (9), 7820–7827. https://doi.org/10.1021/ACSCATAL.8B02120.

(27) Hatzell, M. C.; Liu, Y.-H. Investigating the Photoelectrocatalytic Activity of Titania for Nitrogen Fixation Using Rotating Ring-Disk Electrode Voltammetry. In *ECS Meeting Abstracts*; 2019; p 1682.

(28) Lates, V.; Falch, A.; Jordaan, A.; Peach, R.; Kriek, R. J. An Electrochemical Study of Carbon Dioxide Electroreduction on Gold-Based Nanoparticle Catalysts. *Electrochimica Acta* **2014**, *128*, 75–84. https://doi.org/10.1016/j.electacta.2013.10.162.

(29) Zhu, X.; Gupta, K.; Bersani, M.; Darr, J. A.; Shearing, P. R.; Brett, D. J. L. Electrochemical Reduction of Carbon Dioxide on Copper-Based Nanocatalysts Using the Rotating Ring-Disc Electrode. *Electrochimica Acta* **2018**, *283*, 1037–1044. https://doi.org/10.1016/j.electacta.2018.07.025.

(30) Scholz, J.; Risch, M.; Stoerzinger, K. A.; Wartner, G.; Shao-Horn, Y.; Jooss, C. Rotating Ring-Disk Electrode Study of Oxygen Evolution at a Perovskite Surface: Correlating Activity to Manganese Concentration. *Journal of Physical Chemistry C* **2016**, *120* (49), 27746–27756. https://doi.org/10.1021/acs.jpcc.6b07654.

(31) McCrory, C. C. L.; Jung, S.; Peters, J. C.; Jaramillo, T. F. Benchmarking Heterogeneous Electrocatalysts for the Oxygen Evolution Reaction. *J Am Chem Soc* **2013**, *135* (45), 16977–16987. https://doi.org/10.1021/ja407115p.

(32) Vos, J. G.; Koper, M. T. M. Measurement of Competition between Oxygen Evolution and Chlorine Evolution Using Rotating Ring-Disk Electrode Voltammetry. *Journal of Electroanalytical Chemistry* **2018**, *819*, 260–268. https://doi.org/10.1016/j.jelechem.2017.10.058.

(33) Vos, J. G.; Wezendonk, T. A.; Jeremiasse, A. W.; Koper, M. T. M. MnOx/IrOx as Selective Oxygen Evolution Electrocatalyst in Acidic Chloride Solution. *J Am Chem Soc* **2018**, *140* (32), 10270–10281. https://doi.org/10.1021/jacs.8b05382.

(34) Jebaraj, A. J. J.; Georgescu, N. S.; Scherson, D. A. Oxygen and Hydrogen Peroxide Reduction on Polycrystalline Platinum in Acid Electrolytes: Effects of Bromide Adsorption. *Journal of Physical Chemistry C* **2016**, *120* (29), 16090–16099. https://doi.org/10.1021/acs.jpcc.5b12779.

(35) Marinčić, L.; Leitz, F. B. Electro-Oxidation of Ammonia in Waste Water. *Journal of Applied Electrochemistry* **1978**, *8* (4), 333–345. https://doi.org/10.1007/BF00612687.

(36) Endo, K.; Katayama, Y.; Miura, T. A Rotating Disk Electrode Study on the Ammonia Oxidation. *Electrochimica Acta* **2005**, *50* (11), 2181–2185. https://doi.org/10.1016/j.electacta.2004.09.024.

(37) Chen, S.; Perathoner, S.; Ampelli, C.; Mebrahtu, C.; Su, D.; Centi, G. Room-Temperature Electrocatalytic Synthesis of NH3 from H2O and N2 in a Gas-Liquid-Solid Three-Phase Reactor. *ACS Sustainable Chemistry and Engineering* **2017**, *5* (8), 7393–7400. https://doi.org/10.1021/acssuschemeng.7b01742.

(38) Mukherjee, S.; Cullen, D. A.; Karakalos, S.; Liu, K.; Zhang, H.; Zhao, S.; Xu, H.; More, K. L.; Wang, G.; Wu, G. Metal-Organic Framework-Derived Nitrogen-Doped Highly Disordered Carbon for Electrochemical Ammonia Synthesis Using N2 and H2O in Alkaline Electrolytes. *Nano Energy* **2018**, *48*, 217–226. https://doi.org/10.1016/j.nanoen.2018.03.059.

(39) Furuya, N.; Yoshiba, H. Electroreduction of Nitrogen to Ammonia on Gas-Diffusion Electrodes Loaded with Inorganic Catalyst. *Journal of Electroanalytical Chemistry* **1990**, *291* (1–2), 269–272. https://doi.org/10.1016/0022-0728(90)87195-P.

(40) Rosca, V.; Koper, M. T. M. Electrocatalytic Oxidation of Hydrazine on Platinum Electrodes in Alkaline Solutions. *Electrochimica Acta* **2008**, *53* (16), 5199–5205. https://doi.org/10.1016/j.electacta.2008.02.054.

(41) Gerischer, H.; Mauerer, A. Untersuchungen Zur Anodischen Oxidation von Ammoniak an Platin-Elektroden. *Journal of Electroanalytical Chemistry* **1970**, *25* (3), 421–433. https://doi.org/10.1016/S0022-0728(70)80103-6.

(42) Le Vot, S.; Roué, L.; Bélanger, D. Study of the Electrochemical Oxidation of Ammonia on Platinum in Alkaline Solution: Effect of Electrodeposition Potential on the Activity of Platinum. *Journal of Electroanalytical Chemistry* **2013**, *691*, 18–27. https://doi.org/10.1016/j.jelechem.2012.12.004.

(43) Sheng, W.; Gasteiger, H. A.; Shao-Horn, Y. Hydrogen Oxidation and Evolution Reaction Kinetics on Platinum: Acid vs Alkaline Electrolytes. *Journal of The Electrochemical Society* **2010**, *157* (11), B1529. https://doi.org/10.1149/1.3483106.

(44) Abghoui, Y.; Skúlasson, E. Transition Metal Nitride Catalysts for Electrochemical Reduction of Nitrogen to Ammonia at Ambient Conditions. In *Procedia Computer Science*; Elsevier B.V., 2015; Vol. 51, pp 1897–1906. https://doi.org/10.1016/j.procs.2015.05.433.

(45) Mao, X.; Zhou, S.; Yan, C.; Zhu, Z.; Du, A. A Single Boron Atom Doped Boron Nitride Edge as a Metal-Free Catalyst for N2 Fixation. *Physical Chemistry Chemical Physics* **2019**, *21* (3), 1110–1116. https://doi.org/10.1039/c8cp07064d.

(46) Liu, Y.; Su, Y.; Quan, X.; Fan, X.; Chen, S.; Yu, H.; Zhao, H.; Zhang, Y.; Zhao, J. Facile Ammonia Synthesis from Electrocatalytic N2 Reduction under Ambient Conditions on N-Doped Porous Carbon. *ACS Catalysis* **2018**, *8* (2), 1186–1191. https://doi.org/10.1021/acscatal.7b02165.

(47) Hang, B. T.; Thang, D. H. Electrochemical Properties of Fe2O3 Microparticles and Their Application in Fe/Air Battery Anodes. *Journal of Alloys and Compounds* **2016**, *655*, 44–49. https://doi.org/10.1016/j.jallcom.2015.09.170.

5. The Carbon Dioxide Reduction Reaction

5.1 Introduction

The CO_2 Reduction Reaction (CO_2RR), of all the reactions involving small molecules thus far discussed, is perhaps the one with the highest impact on anthropogenic global warming. Technologies that can reduce CO_2 to valuable chemicals are at the basis of the carbon cycle and will be integral for circular economy. However, in the last decade the industry standards changed to incorporate carbon capture and storage systems (CCS).[1] This approach has been easy, if somewhat costly, to implement by the fossil fuel industry to reduce its impact on the environment. In particular, CO_2 produced by power plants can be scrubbed (usually through amine baths), compressed and injected in geological formations.[2] CCS effectively sequester CO_2 but does not produce anything from it, thus reducing the total amount of carbon in the ecosystem with a non-sustainable solution. Moreover, the gaseous nature of CO_2 casts doubts on the storage stability, due to possible leakage in time.[3] To improve our carbon management, a reduction step must follow carbon capture to release this carbon in a form usable either by humans or the Earth (Carbon Capture and Utilization, CCU).[4] Many processes have been proposed and can take advantage of CO_2: chemical reactions, such as dry reforming, Fisher-Tropsch and the reversed water gas shift (RWGS), work at high temperatures on CO_2 to produce industrially important products (CO, H_2, CH_3OH and hydrocarbons) and are already well established in the industry.[5,6] Photochemical (p-) and electrochemical (e-) CO_2RR try to decrease the energetic requirements of this reduction by operating at low temperatures and in water-based electrolytes. While pCO_2RR can harness the sun's energy, eCO_2RR could exploit cheap and clean electricity from renewables to convert carbon dioxide at low temperature to methane (for combustion), methanol (fuel cells), ethylene, formic acid and CO (for the chemical industry), etc. The possible reaction products are so many that only part of them is usually reported.[7] The main half reactions (and the concurring hydrogen evolution) can be thus summarized:

$$CO_2 + 2e^- + 2H^+ \rightarrow CO + H_2O \tag{1}$$

$$CO_2 + 2e^- + 2H^+ \rightarrow HCOOH \tag{2}$$

$$CO_2 + 4e^- + 4H^+ \rightarrow HCOH + H_2O \tag{3}$$

$$CO_2 + 4e^- + 4H^+ \rightarrow CH_3OH + 2H_2O \tag{4}$$

$CO_2 + 8e^- + 8H^+ \rightarrow CH_4 + 2H_2O$ (5)

$CO_2 + 12e^- + 12H^+ \rightarrow C_2H_4 + 4H_2O$ (6)

$2H^+ + 2e^- \rightarrow H_2$ (7)

Breaking down the energetics and the pathway for CO_2RR on different metals is rather complex due to different surface structures, adsorption energies and scaling relationships between different products.[8] Of all possible materials, copper is unique among the various CO_2RR active metals because of its ability to form C-C bonds, possibly producing a range of various hydrocarbons.[9] Consequently, copper is one of the most studied catalysts for CO_2RR both in experimental and theoretical papers. Schouten et al.[10] studied the main CO_2RR pathways on copper rods by Online Electrochemical Mass Spectroscopy (OEMS) proposing that the first step in the reduction process is the formation of the adsorbed negatively charged carboxyl radical (Fig. 5.1). Once $CO_2^{\cdot\,-}$ is adsorbed it can be reduced either to formate that is readily desorbed in solution, or to CO. Protonation of carbon monoxide leads to carbonyl and then finally methane. If the concentration of adsorbed CO on the surface is high enough, dimerization can occur leading to ethylene and other C_n products.

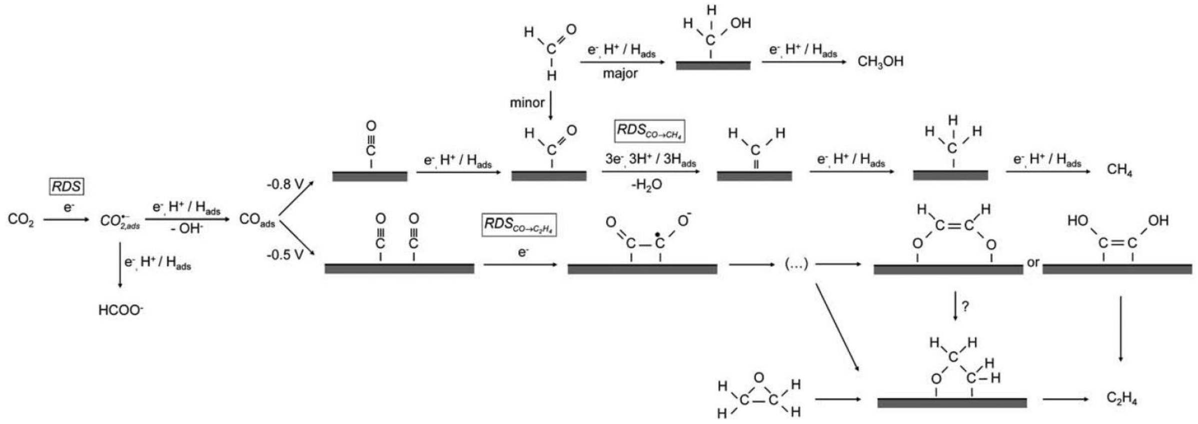

Figure 5.1 Proposed mechanism for the electrochemical reduction of carbon dioxide on copper from ref. [10]. Reproduced with permission. © Copyright 2011 Royal Society of Chemistry.

Other materials have shown high selectivities toward specific carbon products: tin oxide nanoparticles (SnO_2) is able to convert CO_2 to formic acid, with reported FEs exceeding 90%[11] while CO has been produced almost selectively on many gold nanostructures.[12,13] In particular, CO if produced in conjunction with H_2 (from the reduction of the water electrolyte), would allow syngas production, that can then be used by the chemical industry either as is, or to produce hydrogen from it (water gas shift) or methane (catalytic methanation). A downside of CO_2RR research has been its focus on using gas feed without impurities while, in reality, CO_2 separation could significantly impact the energy required for overall CCU. During Fossil fuels burning in power plants CO_2 account for only 5-15% of the flue gas escaping the power plant.[14] The rest is composed mostly by N_2, uncombusted O_2 and nitrogen and sulfur oxides (NO_x and SO_x). On the other hand, many industrial processes release high purity CO_2 streams, but they have little relative weight in our overall carbon emissions.[15] For this reason, a realistic implementation of devices able to abate the anthropogenic CO_2 deriving from fossil fuel-based power plants must take into account the presence of other gases. NO_x and SO_x represent the most critical impurities in CO_2 because they can be reduced readily on CO_2RR catalysts and often lower their efficiencies or poison them entirely.[16,17] As an example Luc et al.[16] studied copper, tin and silver electrodes reactivity to different levels of SO_2 in the CO_2 feed in the ppm range. In particular, copper proved to be the most sensitive metal to sulfur impurities, because at highly reductive potentials surface copper atoms bind sulfur obtaining copper sulfide, a poor CO_2RR catalyst. Figuring out catalysts that can withstand impurities is essential in reducing the cost of CCU and composite materials could stabilize the catalytic site against poisoning.[18,19] In this chapter, the synthesis of copper, tin and copper-tin oxides nanocomposites for CO_2RR will be explored, while the characterization (electrochemical and otherwise) will only be briefly discussed due to ongoing research on these structures.

5.2 Experimental Section

Materials. Copper sulfate pentahydrate ($CuSO_4 \cdot 5H_2O$) was purchased from Carlo Erba. NaOH (pellets, 85%), Sodium Ascorbate, Tin chloride dihydrate ($SnCl_4 \cdot 2H_2O$), Acetic Anhydride (≥99%), NH_4OH 25% solution, Ethanol (99.8%), DMSO (99.9%), Xylene (98.5%), n-Exane (95%), Oleylamine (70%), Oleic Acid (≥99%) were purchased from Sigma Aldrich. SDS was purchased from Merk. All experiments were conducted with milliQ water obtained by using a Direct-Q (Millipore) water purification system. Anhydrous tin chloride was obtained, as reported elsewhere,[20] with acetic anhydride, while Xylene was dried through distillation over sodium metal and DMSO with 5 Å molecular sieves. All other chemicals were used as is.

Synthesis. Copper oxide cubes (Cu_2O) were synthetized following a published procedure with some slight modifications.[21] Typically, in a 1 L glass beaker 380 mL of water were mixed with 2.3 g of SDS and stirred until dissolved. After 10 minutes, 4 mL of a 0.2 M $CuSO_4 \cdot 5H_2O$ solution was added while stirring, then after 5 minutes 2.4 mL of NaOH 1 M and finally, after 30 seconds, 10 mL of a 0.4 M sodium ascorbate solution. The initially transparent solution turned pale blue after addition of copper sulfate, then bright blue with sodium hydroxide and finally green and bright opaque yellow due to Cu_2O nanocubes (NCs) precipitation. After 10 minutes of stirring and 5 minutes of aging the nanoparticle solution was centrifuged and the collected NPs were washed three times with water and once with ethanol. The material was either dried in a vacuum oven at 40 °C (and used as a control) or kept dispersed in ethanol for the next steps in the nanocomposite synthesis.

To create a controlled oxidation at the nanoparticle's surface,[22] the Cu_2O NCs were redispersed in 50mL ethanol and sonicated for 30 minutes. 1 mL of 25% ammonia solution was then added while stirring and the reaction was stopped after 25 minutes, by filtering the solution through a syringe with a 0.22 μm PTFE disposable filter and washed multiple time with water and finally ethanol. During the reaction the material turns gradually from yellow to green and finally brown, while copper (I) is oxidized to copper (II). The material was dried in a vacuum oven at 40°C overnight.

Copper-tin oxides nanocomposites were synthetized through a modified galvanic displacement reaction.[23] A three-necked 50 mL round-bottom flask, equipped with a stirring bar and internal thermometer, was flame-dried under vacuum and then purged with argon. Subsequently, a known amount of copper (I-II) oxide NCs was added with 30 mL of dried Xylene and 2.6 mL oleylamine and sonicated for 30 minutes. The mixture was heated with an oil bath to 90 °C and then 3 equivalents of Sn(II) were added trough a 1.5 M solution of anhydrous $SnCl_2$ in dried DMSO. The reaction was left stirring for 2h, while the solution became increasingly blue due to stripped copper ions. Then, the flask was left to cool in air and its content centrifuged to separate the nanoparticles. The NPs were washed and centrifuged with xylene, a 2:1 n-exane ethanol mixture for three times. The material was dried in a vacuum oven at 40°C overnight.

5.3 Results and discussion

Synthesis and characterization. The synthesis of cubic copper-tin oxide nanoparticles required multiple steps that were separately optimized. First, Cu_2O nanocubes (NCs) were obtained from the reduction of tetrahydroxycuprate (II) ion with sodium ascorbate. This copper ion is produced in situ with a ligand exchange on the copper center between the sulfate ion and the hydroxyl from sodium hydroxide. The introduction in solution of SDS as a capping agent is of outmost importance to limit the growth of the nanoparticles and direct plane formation toward the nanocube shape.[24] After SDS is completely dissolved in solution, copper sulfate pentahydrate and NaOH can be added to create the tetrahydroxycuprate (II) ion in solution. Finally, the copper complex can be reduced to copper (I) oxide NC adding a sodium ascorbate solution. TEM analysis of the obtained material reveals cubic nanoparticles with well controlled dimensions of 106 ± 10 nm (Fig. 5.2)

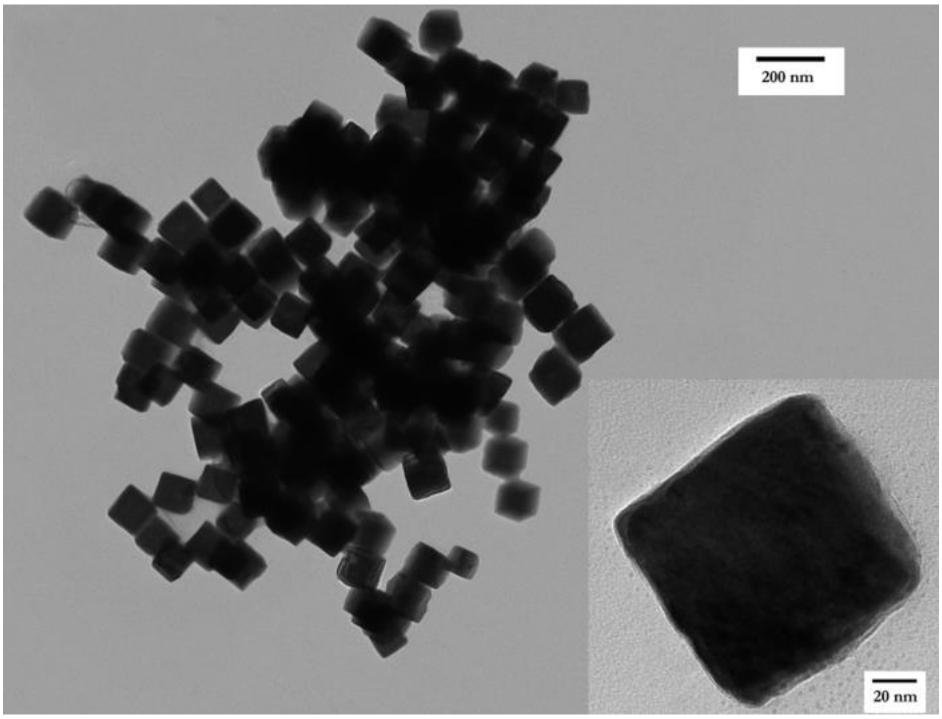

Figure 5.2 Typical morphology of Cu_2O nanocubes visible in low magnification TEM image and high magnification (inset)

A second synthetic step was the partial (i.e. surface) oxidation of the NCs to obtain Cu_2O@CuO core shell structures. The surface oxidation was achieved with a very simple reaction, adding 1 mL of 25% ammonium hydroxide solution to a dispersion of the as obtained Cu_2O NCs. The reaction is reported[22] to proceed by first oxidizing the outer layer of the nanoparticles and, if let go for enough time, resulting in hollow structures ranging from Hollow NanoCubes (HNC) to spiked nanoparticles. Confirming Park et al. procedure,[22] after 25 minutes of reaction the nanocube shape was still intact with progressive outer shell formation. The change in color of the powder is an indication of successful oxidation and was confirmed by the appearance of a small peak in XRD analysis (Fig. 5.3). While the peaks for Cu_2O remained unperturbed, the small peak at 38° was assigned to CuO.[25] However, TEM analysis showed negligible differences, due to the similar response of the copper oxides to the electron beam and unchanged dispersion of the NCs dimensions (Fig. 5.4).

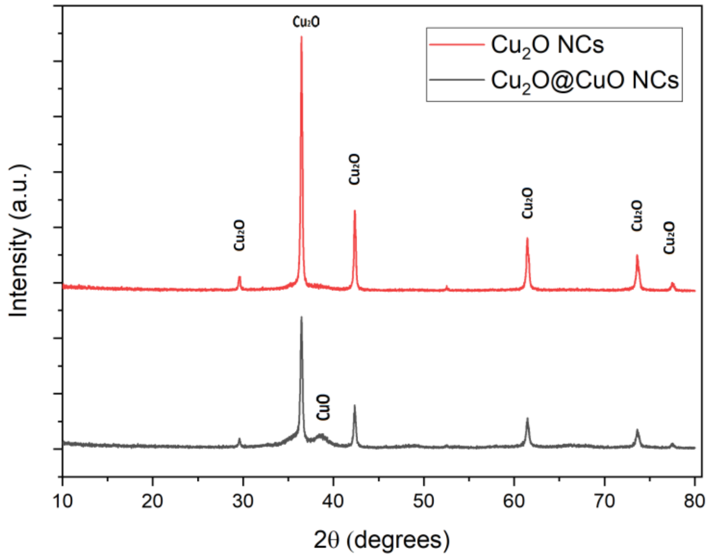

Figure 5.3 XRD powder analysis of Cu2O NCs (red) and Cu2O@CuO NCs (black).

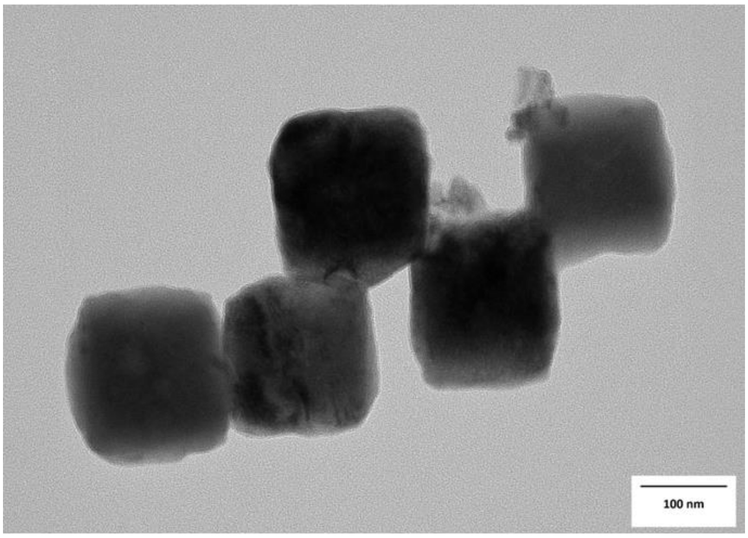

Figure 5.4 TEM image of Cu2O@CuO NCs

Finally, the outer Cu(II) present on the NCs could be used to deposit SnO_2 on the surface of the nanoparticles through Galvanic Displacement (GD).[23] GD is a spontaneous electrochemical process that evolves at open circuit potential (i.e. with net zero currents). In GD a metal atom with high standard reduction potential can be stripped (i.e. reduced) from an oxide surface by another metal with low reduction potential resulting in the metal exchange. Oh's et al.[23] explored GD in metal oxide nanoparticles to obtain core-shell and hollow structures from various metal oxides. However, during our synthetic trials, Cu_2O proved too fragile for the process: the synthetic procedure proposed by Oh et al., used a biphasic xylene and water system to obtain inverse micelles. Nevertheless, $SnCl_2$ in aqueous solutions readily releases HCl that, during the reaction time, completely dissolves any copper oxide. The modified synthetic procedure uses anhydrous $SnCl_2$ in dried DMSO. The resulting nanoparticles were cleaned with n-hexane/ethanol mixture and deposited on Vulcan carbon through impregnation. TEM analysis shows a cage-like shape with spiked borders, given by the etched Cu_2O nanocube and will be referred as **$CuO@SnO_2$ Hollow NanoCubes** (**HNCs**, Fig. 5.5).

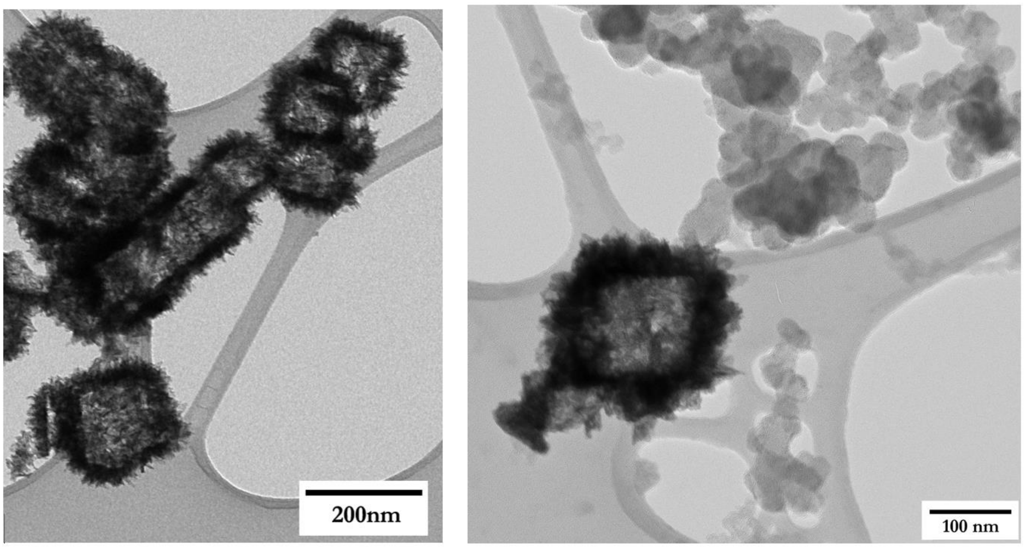

Figure 5.5 Low magnification TEM of $CuO@SnO_2$ HNCs and HNCs deposed on Vulcan

The surface area of $CuO@SnO_2$ HCNs and Cu2O@CuO NCs were characterized electrochemically (ECSA) through double layer capacitance (Fig. 5.6) As expected the cage-like nanoparticles showed almost doubled surface areas (3 m^2/g vs 1.75 m^2/g), due either to increased roughness of the HCNs themselves (as visible in Fig. 5.6) or to partial accessibility of the inner cage surface.

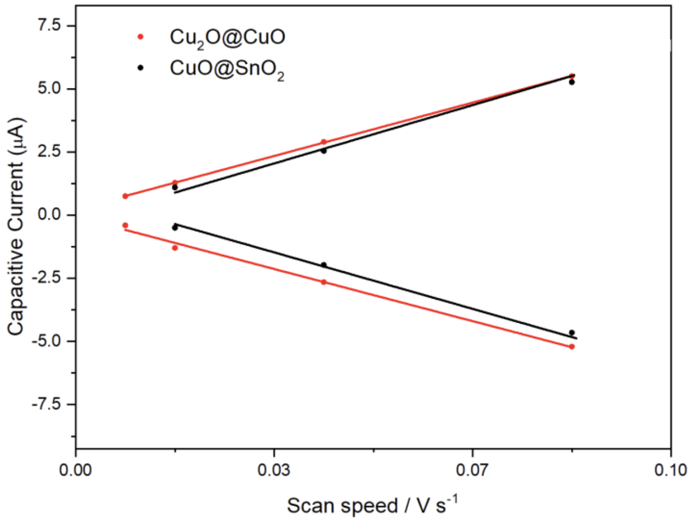

Figure 5.6 ECSA calculations for core-shell NCs (red) and HNCs (black)

Surface SnO_2 deposition was confirmed by both ICP-OES and XPS measurements (Fig. 5.5). ICP-OES revealed a molar ratio of 40% SnO_2 (with remaining 60% being copper oxide). Tin (II) and tin (IV) have very similar 2p spectra in XPS, but it is reasonable to assume that all Sn found on the material is in the (IV) oxidation number, because $SnCl_2$ was oxidized during the reaction. Copper surface oxidation state was determined through fitting of the Cu $2p_{3/2}$ region (~934 eV) and the Auger Cu LMM region (~570 eV). The absence of Cu (0) was confirmed from the LMM region, where there was no visible contribution at 567.5 eV. The deconvolution of the Cu $2p_{3/2}$ region showed the presence of both Cu(I) and Cu(II), with Cu_2O (532.5 eV) in a relative occurrence of 25% while 50% was assigned to copper hydroxide (534.6 eV) and 25% to CuO (533.5 eV).

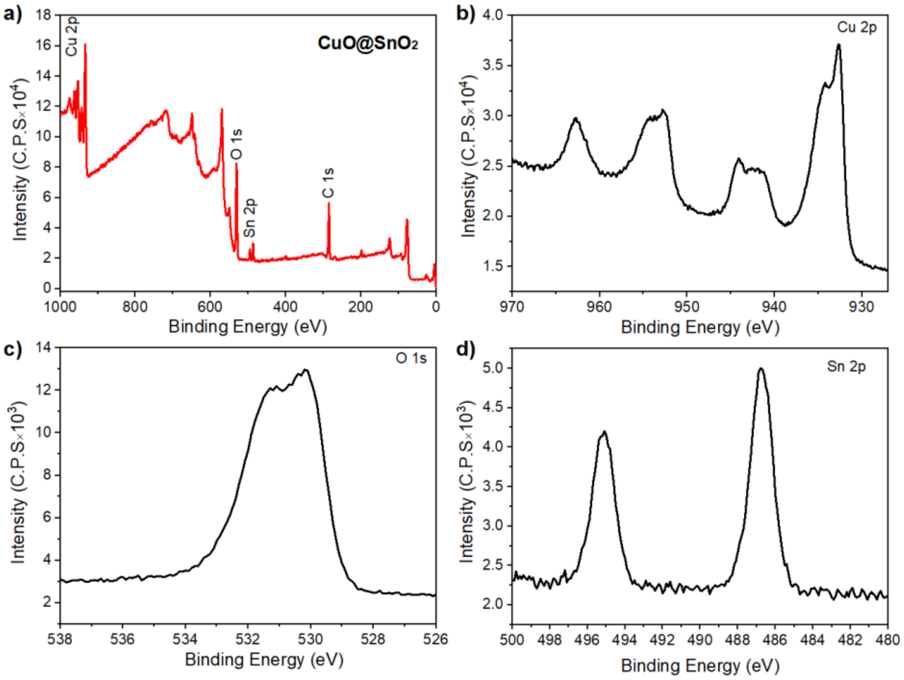

Figure 5.7 Full XPS survey (a) of $CuO@SnO_2$ HNCs and high-definition Cu 2p (b), O 1s (c) and Sn 2p spectra (d).

Electrocatalytic Tests. CO_2RR tests were done on the core-shell $Cu_2O@CuO$ nanocubes and the $CuO@SnO_2$ hollow nanocubes to understand the effect of the tin oxide shell on the catalytic selectivity of the material. Chronopotentiometries were used to assess the different catalysts in an H-cell (for more information on the setup, see Chapter 2) filled with 0.5 M $KHCO_3$. Once the electrolyte was saturated with pure CO_2, the CPs were started at 40 mA cm^{-2} (Fig. 5.8). After a brief time in which the potential increased, both materials proved very stable and even lowered the potential needed to maintain a fixed output of 40 mA cm^{-2}. The copper oxide catalysts often show this trend because at reducing potentials copper metal is the most stable phase, and also a better CO_2RR and HER catalyst.[26,27]

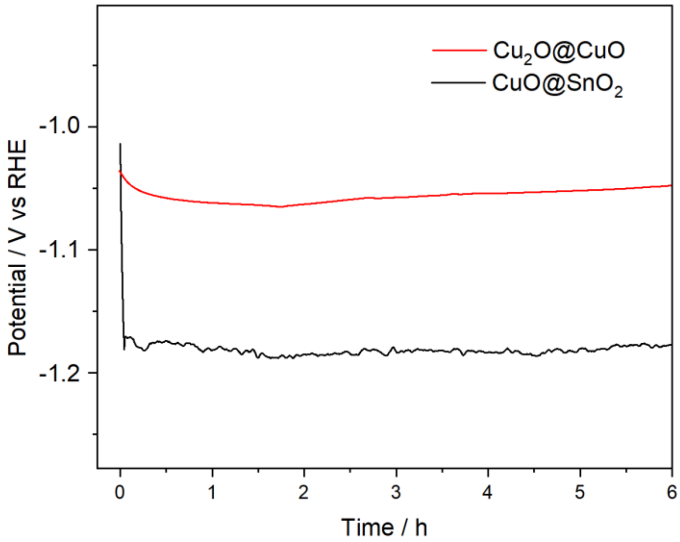

Figure 5.8 CPs at 40 mA cm^{-2} of Cu_2O@CuO (red) and CuO@SnO_2 (black) over a 6 h period in a H-cell filled with 0.5 M $KHCO_3$. The potential is corrected for pH.

The selectivity of both materials was measured by gas chromatography (GC, for non-soluble products) and ionic chromatography (IC, for formate) by collecting a small aliquot of the cell catholyte or the sparging gas. Chromatography analysis showed that both materials suppress HER to less than 15% FE. As expected,[11] CuO@SnO_2 HNCs showed a heightened (3x) activity toward formate production, while both materials show good methane production and no traces of ethylene and ethane production. Moreover, 20 to 25% of FE is lost probably due to non-tracked products (i.e. methanol[28]) or side reaction at the electrode (such as reduction of copper oxide to copper metal).

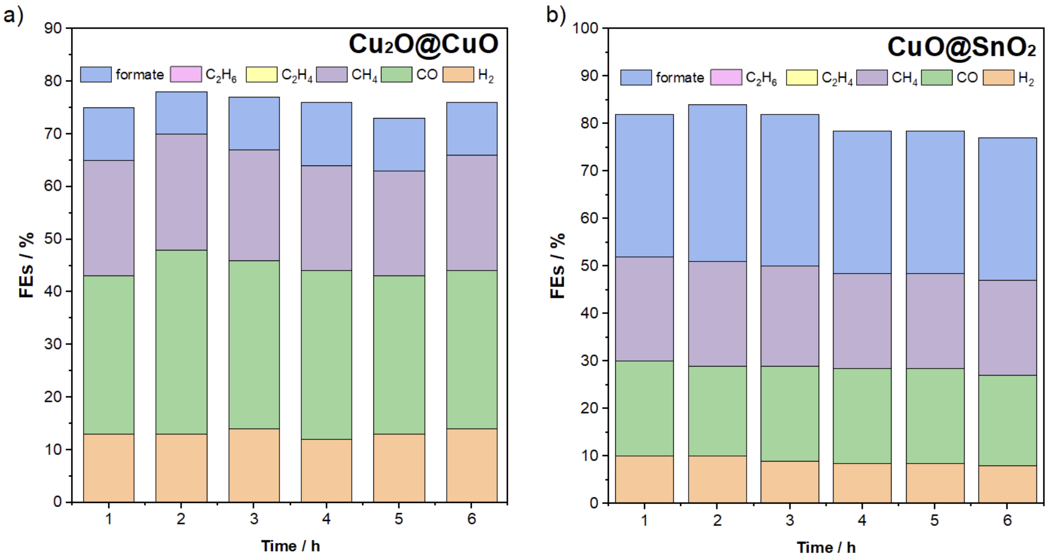

Figure 5.9 Faradaic efficiencies for different tracked CO_2RR and concurrent HER products of NCs (a) and HNC (b) with a fixed current of 40 mA cm^{-2} (Fig. 5.8). The gaseous products were tracked through online GC, while formate was measured by IC of an electrolyte sample.

CP runs in N_2 saturated electrolytes showed no other than HER activity, confirming that the reduction is at the expense of dissolved CO_2 in solution. Other CP measurements at different current densities, as well as CPs with mixed gas feeds, are underway in the group of professor Jonas Baltrusaitis in Lehigh University (Bethlehem PA, USA). In addition, the use of XPS and STEM-EELS analysis will shed a light on surface modification of the catalysts and identification of the active species (metallic Cu or the oxide species and Cu or Sn in the composites). The use of non-pure CO_2, through controlled mixing with nitrogen and SO_2, will serve to understand the stability and general viability of these materials as CO2RR catalyst fed with flue gas from power plants. The HNCs in particular will be interesting to characterize, because of the resiliency it showed in previous papers to SO_2 poisoning.[16] This CO_2RR characterization of NCs and HNCs will serve as the standard for the mixed feeds experiments that will follow.

5.4 Conclusions

The synthesis of Cu/Sn oxides nanoparticles was optimized for the peculiar properties of copper and tin. The resulting hollow nanocubes have interesting features due to the cubic copper oxide intermediate and the complete etching of the inner core by the tin chloride. These materials are also highly interesting in electrocatalysis because of copper ability of C-C coupling and tin stability and selectivity toward formate production (against hydrogen evolution). The CO_2RR activity of NCs and HNCs has been confirmed through CP coupled with GC and IC analysis, showing hampering of HER and yield of several CO_2 reduction products. These tests are needed not only to characterize CO_2RR activity of both materials, but also as a control experiment for SO_2/CO_2 mixed feed trials that are already underway in the group of professor Jonas Baltrusaitis at Lehigh University (USA).

References

(1) Raza, A.; Gholami, R.; Rezaee, R.; Rasouli, V.; Rabiei, M. Significant Aspects of Carbon Capture and Storage – A Review. *Petroleum* **2019**, *5* (4), 335–340. https://doi.org/10.1016/J.PETLM.2018.12.007.

(2) *The Global Status of CCS: 2016 Summary Report - Global CCS Institute*. https://www.globalccsinstitute.com/resources/publications-reports-research/the-global-status-of-ccs-2016-summary-report/ (accessed 2022-05-23).

(3) Chen, A.; Lin, B. L. A Simple Framework for Quantifying Electrochemical CO2 Fixation. *Joule* **2018**, *2* (4), 594–606. https://doi.org/10.1016/J.JOULE.2018.02.003.

(4) Cuéllar-Franca, R. M.; Azapagic, A. Carbon Capture, Storage and Utilisation Technologies: A Critical Analysis and Comparison of Their Life Cycle Environmental Impacts. *Journal of CO2 Utilization* **2015**, *9*, 82–102. https://doi.org/10.1016/J.JCOU.2014.12.001.

(5) Davis, S. J.; Lewis, N. S.; Shaner, M.; Aggarwal, S.; Arent, D.; Azevedo, I. L.; Benson, S. M.; Bradley, T.; Brouwer, J.; Chiang, Y. M.; Clack, C. T. M.; Cohen, A.; Doig, S.; Edmonds, J.; Fennell, P.; Field, C. B.; Hannegan, B.; Hodge, B. M.; Hoffert, M. I.; Ingersoll, E.; Jaramillo, P.; Lackner, K. S.; Mach, K. J.; Mastrandrea, M.; Ogden, J.; Peterson, P. F.; Sanchez, D. L.; Sperling, D.; Stagner, J.; Trancik, J. E.; Yang, C. J.; Caldeira, K. Net-Zero Emissions Energy Systems. *Science (1979)* **2018**, *360* (6396). https://doi.org/10.1126/SCIENCE.AAS9793/SUPPL_FILE/AAS9793-DAVIS-SM.PDF.

(6) Deutschmann, O.; Knözinger, H.; Kochloefl, K.; Turek, T. Heterogeneous Catalysis and Solid Catalysts, 3. Industrial Applications. *Ullmann's Encyclopedia of Industrial Chemistry* **2011**. https://doi.org/10.1002/14356007.O05_O03.

(7) Chatterjee, T.; Boutin, E.; Robert, M. Manifesto for the Routine Use of NMR for the Liquid Product Analysis of Aqueous CO2 Reduction: From Comprehensive Chemical Shift Data to Formaldehyde Quantification in Water. *Dalton Transactions* **2020**, *49* (14), 4257–4265. https://doi.org/10.1039/C9DT04749B.

(8) Peterson, A. A.; Nørskov, J. K. Activity Descriptors for CO 2 Electroreduction to Methane on Transition-Metal Catalysts. *Journal of Physical Chemistry Letters* **2012**, *3* (2), 251–258. https://doi.org/10.1021/JZ201461P.

(9) Peterson, A. A.; Abild-Pedersen, F.; Studt, F.; Rossmeisl, J.; Nørskov, J. K. How Copper Catalyzes the Electroreduction of Carbon Dioxide into Hydrocarbon Fuels. *Energy & Environmental Science* **2010**, *3* (9), 1311–1315. https://doi.org/10.1039/C0EE00071J.

(10) Schouten, K. J. P.; Kwon, Y.; van der Ham, C. J. M.; Qin, Z.; Koper, M. T. M. A New Mechanism for the Selectivity to C1 and C2 Species in the Electrochemical Reduction of Carbon Dioxide on Copper Electrodes. *Chemical Science* **2011**, *2* (10), 1902–1909. https://doi.org/10.1039/C1SC00277E.

(11) Zhang, S.; Kang, P.; Meyer, T. J. Nanostructured Tin Catalysts for Selective Electrochemical Reduction of Carbon Dioxide to Formate. *J Am Chem Soc* **2014**, *136* (5), 1734–1737. https://doi.org/10.1021/JA4113885.

(12) Saberi Safaei, T.; Mepham, A.; Zheng, X.; Pang, Y.; Dinh, C. T.; Liu, M.; Sinton, D.; Kelley, S. O.; Sargent, E. H. High-Density Nanosharp Microstructures Enable Efficient CO2 Electroreduction. *Nano Letters* **2016**, *16* (11), 7224–7228. https://doi.org/10.1021/ACS.NANOLETT.6B03615.

(13) Chen, Y.; Li, C. W.; Kanan, M. W. Aqueous CO2 Reduction at Very Low Overpotential on Oxide-Derived Au Nanoparticles. *J Am Chem Soc* **2012**, *134* (49), 19969–19972. https://doi.org/10.1021/JA309317U.

(14) Bains, P.; Psarras, P.; Wilcox, J. CO2 Capture from the Industry Sector. *Progress in Energy and Combustion Science* **2017**, *63*, 146–172. https://doi.org/10.1016/J.PECS.2017.07.001.

(15) Last, G. v.; Schmick, M. T. A Review of Major Non-Power-Related Carbon Dioxide Stream Compositions. *Environmental Earth Sciences* **2015**, *74* (2), 1189–1198. https://doi.org/10.1007/S12665-015-4105-4.

(16) Luc, W.; Ko, B. H.; Kattel, S.; Li, S.; Su, D.; Chen, J. G.; Jiao, F. SO2-Induced Selectivity Change in CO2 Electroreduction. *J Am Chem Soc* **2019**. https://doi.org/10.1021/JACS.9B03215.

(17) Ko, B. H.; Hasa, B.; Shin, H.; Jeng, E.; Overa, S.; Chen, W.; Jiao, F. The Impact of Nitrogen Oxides on Electrochemical Carbon Dioxide Reduction. *Nature Communications 2020 11:1* **2020**, *11* (1), 1–9. https://doi.org/10.1038/s41467-020-19731-8.

(18) Hou, P.; Song, W.; Wang, X.; Hu, Z.; Kang, P. Well-Defined Single-Atom Cobalt Catalyst for Electrocatalytic Flue Gas CO2 Reduction. *Small* **2020**, *16* (24), 2001896. https://doi.org/10.1002/SMLL.202001896.

(19) Xu, Y.; Edwards, J. P.; Zhong, J.; O'Brien, C. P.; Gabardo, C. M.; McCallum, C.; Li, J.; Dinh, C. T.; Sargent, E. H.; Sinton, D. Oxygen-Tolerant Electroproduction of C 2 Products from Simulated Flue Gas. *Energy & Environmental Science* **2020**, *13* (2), 554–561. https://doi.org/10.1039/C9EE03077H.

(20) Armarego, W. L. F.; Chai, C. L. L. Common Physical Techniques Used in Purification. *Purification of Laboratory Chemicals* **2009**, 1–60. https://doi.org/10.1016/B978-1-85617-567-8.50009-3.

(21) Thoka, S.; Lee, A. T.; Huang, M. H. Scalable Synthesis of Size-Tunable Small Cu2O Nanocubes and Octahedra for Facet-Dependent Optical Characterization and Pseudomorphic Conversion to Cu Nanocrystals. *ACS Sustainable Chemistry and Engineering* **2019**, *7* (12), 10467–10476. https://doi.org/10.1021/ACSSUSCHEMENG.9B00844.

(22) Park, J. C.; Kim, J.; Kwon, H.; Song, H. Gram-Scale Synthesis of Cu2O Nanocubes and Subsequent Oxidation to CuO Hollow Nanostructures for Lithium-Ion Battery Anode Materials. *Advanced Materials* **2009**, *21* (7), 803–807. https://doi.org/10.1002/ADMA.200800596.

(23) Oh, M. H.; Yu, T.; Yu, S. H.; Lim, B.; Ko, K. T.; Willinger, M. G.; Seo, D. H.; Kim, B. H.; Cho, M. G.; Park, J. H.; Kang, K.; Sung, Y. E.; Pinna, N.; Hyeon, T. Galvanic Replacement Reactions in Metal Oxide Nanocrystals. *Science (1979)* **2013**, *340* (6135), 964–968. https://doi.org/10.1126/SCIENCE.1234751.

(24) Rej, S.; Bisetto, M.; Naldoni, A.; Fornasiero, P. Well-Defined Cu 2 O Photocatalysts for Solar Fuels and Chemicals. **2021**. https://doi.org/10.1039/d0ta10181h.

(25) Amal, M. I.; Wibowo, J. T.; Nuraini, L.; Senopati, G.; Hasbi, M. Y.; Priyotomo, G. Antibacterial Activity of Copper Oxide Nanoparticles Prepared by Mechanical Milling. *IOP Conference Series: Materials Science and Engineering* **2019**, *578* (1), 012039. https://doi.org/10.1088/1757-899X/578/1/012039.

(26) Kim, J.; Choi, W.; Park, J. W.; Kim, C.; Kim, M.; Song, H. Branched Copper Oxide Nanoparticles Induce Highly Selective Ethylene Production by Electrochemical Carbon Dioxide Reduction. *J Am Chem Soc* **2019**, *141* (17), 6986–6994. https://doi.org/10.1021/JACS.9B00911

(27) Ferrara, M.; Bevilacqua, M.; Tavagnacco, C.; Vizza, F.; Fornasiero, P. Fast Screening Method for Nitrogen Reduction Reaction (NRR) Electrocatalytic Activity with Rotating Ring-Disc Electrode (RRDE) Analysis in Alkaline Environment. *ChemCatChem* **2020**, *12* (24), 6205–6213. https://doi.org/10.1002/CCTC.202001498.

(28) Yang, H.; Wu, Y.; Li, G.; Lin, Q.; Hu, Q.; Zhang, Q.; Liu, J.; He, C. Scalable Production of Efficient Single-Atom Copper Decorated Carbon Membranes for CO2 Electroreduction to Methanol. *J Am Chem Soc* **2019**, *141* (32), 12717–12723. https://doi.org/10.1021/JACS.9B04907.

6. Conclusions and outlook

This research project has focused on the development of new nanostructured electrocatalysts for small molecules (O_2, N_2 and CO_2) activation. The application of electrocatalysis to energy storage and conversion, through electrolyzers and fuel cells, has gained traction in research especially with today's increased attention on the environment. Nanotechnology has the potential to bring to the market new electrolytic processes that could boost green chemistry with their improved sustainability (low temperature and pressures, water-based electrolytes, earth abundant catalyst materials, etc.). The project addressed i) the synthesis of novel materials with nanometric features reflected in their heightened catalytic performance, ii) the characterization of these materials with advanced techniques such as XRD, XPS, TEM, TGA, N_2 physisorption, UV-Vis and Raman spectroscopy, and iii) the development of protocols to speed up the research of novel catalysts.

In particular, during research on oxygen reduction reaction catalysts, platinum porous multifaceted nanoparticles were obtained through soft templating method, and their above-average activity was linked to their porosity and exposed facets by comparison with non-porous nanoparticles and commercial Pt on carbon. Moreover, a core shell structure with a cobalt core and a shell of graphitized carbon was synthetized and characterized to enable the electroproduction of hydrogen peroxide (through partial reduction of O_2). Many parameters were studied: the impact of pyrolysis temperature on porosity and N,O functionalities on the carbon surface and thus on electrocatalytic activity, but also the deposition thickness as well as the type of electrode support (glassy carbon or carbon paper) and the electrolyzer type and geometry. In this case, the best performances were achieved balancing the degree of functionalization and graphitization: the higher the pyrolysis temperature, the higher the selectivity showed by the material toward hydrogen peroxide to the detriment of the peak current output.

To speed up research on nitrogen reduction reaction catalysts we developed a protocol to qualitatively evaluate nitrogen reduction, based on the rotating ring disk electrode technique. This type of electrode, commonly referred to as RRDE, has been previously used to evaluate selectivity of ORR, OER but also, more recently, CO_2RR. RRDEs are increasingly present in every electrochemical lab and their application in heterogeneous catalysis have significantly streamlined many analytical techniques (i.e. titrations) that require much more time and additional chemicals. This new protocol can not only detect very low level of produced ammonia (thanks to selective adsorption of ammonia on the platinum ring electrode), but it allows for the assessment of the stability of many N-containing materials toward degradation. Ruling out secondary sources of nitrogen compounds in solution is very important in eNRR because at the lab-scale currents level (mA range), spurious ammonia can significantly affect FE calculations.

Finally, during research on CO_2 reduction reaction, a series of core-shell and hollow NPs were synthetized exploiting the reduction potential differential between the Cu(I)/Cu(II) redox couple and Sn(II)/Sn(IV). An exchange reaction (i.e. Galvanic Displacement), was used to etch Cu atoms from copper oxide cubic NPs, depositing SnO_2 on its surface. Both materials are inherently interesting for CO_2RR from literature, but the deposition of one material over the other in a controlled manner could unlock new catalytic features. In particular, the CO_2RR benchmarking of these materials reported in chapter 5 represents the control experiments for a wider application in flue gas (i.e. combustion exhaust from a power plant) treatment. Electrocatalysts designed for flue gas treatment must be able to tolerate poisoning from acidic gasses, such as NO_x and SO_x. Moreover, copper has already been found to be particularly sensitive to SO_2 in the gas mixture, much more than tin-based electrodes. Nanocomposite materials could be a step in the right direction against surface poisoning, and synthetized copper-tin structures have already shown promising electrochemical results.

The use in conjunction of very different electrochemical cells has shed light on the importance of evaluating a material on different supports and cell geometries. The basic electrochemical cell with a single compartment, used for LSVs and CVs was each time complemented with the most appropriate electrolyzer setup, because every electrochemical reaction has its own challenges and constrains (e.g. NRR need for a clean environment, or CO_2RR gas and liquid products detection).

In conclusion, this thesis provided a solid methodological basis for eNRR catalytic testing through the RRDE setup that will be instrumental for future research and publications on this topic. Moreover, the previously discussed ORR and CO_2RR advances build over the work done in the group in the last years and aim to extend the application of these materials from lab scale environment to setups resembling industrial conditions both in geometry and for the presence of impurities in the electrolyte.

Acknowledgements

Grazie per essere arrivati fino a qui, fino alla fine di questi tre anni e 121 pagine. Grazie al *Supervisor* Paolo Fornasiero, grazie a Michele, a Manuela e a Valentina che mi hanno trascinato fino al traguardo e grazie a Mario, Simone e tutti quelli che si sono trascinati con me. Grazie ad Arianna per aver reso gli anni del dottorato più belli. Grazie ai colleghi del laboratorio, e a quelli dei laboratori limitrofi. Insomma, grazie un po' a tutti, anche a sci-hub se vogliamo essere prodighi.

Sicuramente ci sono molte altre persone che andrebbero ringraziate, da Paolo Bertoncin che mi ha fatto fare i primi passi col TEM, ai tecnici XRD di Udine. Alejandro Criado a San Sebastian per l'aiuto con i dati XPS. Il professor Morgante e la professoressa Pasquato per aver coordinato il dottorato in nanotecnologie in questi anni. Grazie a Giovanni che da lontano si è tenuto in contatto e ha fugato i dubbi che mi venivano qua e là.

Lo so che è un po' mainstream ma grazie ai miei genitori, non so se sé lo sono mai sentiti dire.